Novel Thin Film Technologies for Rapid Manufacture of Glassy Carbon and its Application in Printed Electronics and Energy Storage

By

Brent de Boode

Submitted to Swansea University in fulfilment of the requirements for the Degree of Doctor of Philosophy

Swansea University

2022

Summary

This doctoral thesis is a research study into the thin film manufacture and applications of glassy carbon. The aim of this research was to explore photonic curing as a novel rapid manufacturing method to produce glassy carbon thin films and to expand the applications of glassy carbon in energy storage and printed electronics.

Photonic curing was explored as a rapid method for producing glassy carbon coatings, reducing processing time from ~20 hours for conventional thermal processing down to ~1 minute. For both photonic and conventional thermal produced coatings, Raman spectroscopy and primary peak XPS data showed sp^2 bonded carbon, indicative of bulk glassy carbon. XPS analysis indicated greater sp^3 content at the immediate surface (5-10 nm) for photonic cured carbon compared with thermally cured carbon, likely due to the local environment (temperature, atmosphere) around the surface during conversion. The produced coatings were resilient, highly smooth, with no evidence of surface defects.

The ability to rapidly manufacture glassy carbon coatings, by way of photonic curing, expands the potential window of applications of glassy carbons for high volume applications such as coatings for energy storage, rapid manufacture of complex electrically conductive shapes, and the opportunity to use temperature sensitive substrates.

Photonic cured and thermal carbonized glassy carbon thin films were explored as electrode active materials. The glassy carbon thin films from both manufacturing methods showed comparable specific capacitances to one another and to the use of porous glassy carbon as a supercapacitor active electrode material in literature.

Screen printed glassy carbon structures were made to explore potential applications for glassy carbon in printed electronics and sensors. These prints yielded electrical conductivities comparable to carbon based conductive inks, potentially expanding the applications window for glassy carbon for electronics devices with high chemical resistance, low reactivity and high thermal stability. Screen printed glassy carbon temperature and salinity sensors were produced and tested, glassy carbon as a temperature sensor yielded promising results whereas glassy carbon as a salinity sensor did not have a significant response with the investigated parameters.

Declarations and Statements

This work has not previously been accepted in substance for any degree and is not being concurrently submitted in candidature for any degree.

Signed: Brent de Boode

Date: 04/01/2023

This thesis is the result of my own investigations, except where otherwise stated. Other sources are acknowledged by footnotes giving explicit references.   A bibliography is appended.

Signed: Brent de Boode

Date: 04/01/2023

I hereby give my consent for my work, if relevant and accepted, to be available for photocopying and for inter-library loans **after expiry of a bar on access approved by the University.**

Signed: Brent de Boode

Date: 04/01/2023

The University's ethical procedures have been followed and, where appropriate, that ethical approval has been granted.

Signed: Brent de Boode

Date: 04/01/2023

Contents Page

Acknowledgements

I would like to take this opportunity to thank all those who have contributed towards this research project.

I would like to individually thank:

Dr. Davide Deganello for instigating and supervising the project, as well as aiding in the publishing of my research.

Dr. Chris Phillips for supervising the project and aiding in the publishing of my research.

Alaa Alaizoki for his help and support with the rheology measurements.

Dr. Yin Cheung Lau for his help and support with the photonic curing experiments.

Dr. Dan Jones for his help and support with the electrochemical experiments.

I would like to thank the Engineering and Physical Sciences Research Council for funding the project.

I wish to offer personal thanks to my parents for their support.

Publications

Journal article:

De Boode, B., Phillips, C., Lau, J., Adomkevicius, A., McGettrick, J., & Deganello, D. (2022). Glassy carbon manufacture using rapid photonic curing. Journal of Materials Science, 57(1), 299-310. https://doi.org/10.1007/s10853-021-06648-w

Date of Publication: 03/01/2022

List of Figures and Tables

Figures

Tables

Chapter 1: Introduction

1.1 Introduction

The research in this thesis explored a novel method of carbonization to produce glassy carbon thin films using photonic curing and explored new potential applications for glassy carbon in energy storage and printed electronics applications. Glassy carbon is a material with attractive characteristics for energy storage and electronics applications due to it high electrical conductivity, chemical resistance and gas impermeability. The endeavours of the research into manufacturing glassy carbon using photonic curing resulted in a publication in the Journal of Material Science on the 3rd of January 2022, titled "Glassy carbon manufacture using rapid photonic curing" (1). Glassy carbon thin films manufactured using both thermal and photonic curing were investigated as potential active anode materials for energy storage applications such as supercapacitors or batteries. Screen printed glassy carbon structures were characterised and explored as a novel combination of deposition and material for printed electronics applications such as temperature and salinity sensors.

1.2 Glassy Carbon Properties and Applications

Glassy carbon (GC) also known as vitreous carbon, is a non-graphitizing carbon with characteristics intermediate between those of graphite and ceramics (2,3). Non-graphitizing carbons are carbons that consist of graphitic nano-crystallites that are cross-linked between crystals in an isotropic fashion (2). This structure offers a host of important material properties including substantial hardness, high temperature resistance, impermeability to gases, low electrical resistance, chemical resistance and biocompatibility (2–9). These properties make it a useful material for electrochemical, corrosion and medical applications among others. GC is commonly used as a reference electrode in electrochemistry (5,10–15), as corrosion protection for current collectors (7,16–18) and as a surgical implant material in both humans and animals (8,9,19–21).

1.3 Glassy Carbon Production

Glassy carbon is typically produced through an endothermic reaction by the carbonization of a resole-type thermoset resin precursor (22,23) either as a bulk material or as a film (7,17,21,24–27). Common precursor resins are phenol formaldehyde and furfuryl alcohol (28). After coating and prior to heat treatment the precursor is cured by temperature or catalyst (21,29). Carbonizing the precursor is achieved by heat treatment in an inert

atmosphere with a minimum temperature of 600°C although most commercially produced glassy carbon materials are carbonized between 1000°C and 2000°C depending on the desired characteristics of the glassy carbon (24,26,27). Glassy carbon make by carbonization at the upper temperature range (~2000°C) provides a more electrically conductive material that is more brittle, whereas glassy carbon of lower carbonization temperatures (~1000°C) results in a more flexible and chemically inert glassy carbon (24–27,30). Limitations of this production method are the time and temperature required to carbonize the precursor. Polymer carbonization is a process that generally requires several hours of high temperature thermal treatment, typically in an inert atmosphere, with additional time for ramping the furnace temperature up and down. For a high quality conversion from resin to carbon low ramp rates are used, typically 1-5°C/min, this causes the typical conversion time to lie in the order of several hours (25,30). The requirement of high temperatures and long carbonization times are bottlenecks in the usability of GC in all its applications. In addition to this, if the material were to be required as a coating, then the substrate itself would need to be subjected to the same thermal treatment as the glassy carbon.

1.4 Photonic Curing as Potential Glassy Carbon Manufacture Method

Photonic curing is a recently developed alternative technology to the conventional convection oven which currently sees most use in the drying and sintering of printed or coated thin films (31–36). Photonic curing uses xenon lamps to rapidly pulse high-intensity light, transferring a high energy density to the surface of an object (31). Photonic curing minimizes the thermal treatment times while allowing conventional oven-comparable temperatures to be reached at the surface of the exposed object (32). The reduction in time is achieved because there are no requirements for ramping, holding or cooling times as the energy delivery using light is almost instantaneous. An example from Cronon *et al.* (37) where photonic curing is used to sinter aqueous silver inks shows a reduction in curing time from 90 minutes to 9 ms. Photonic curing can also be integrated with roll-to-roll processing (33) and the curing speed allows for a decrease in physical space required in automated, in-line manufacturing as it would replace an otherwise large heat or radiation curing oven (34). The localised and transient nature of photonic curing also enables the potential use of low-cost, flexible, temperature sensitive components/carrier substrates to be used for thin and thick carbon films that ordinarily could not withstand conventional thermal treatment (34). Photonic curing pulse parameters, such as lamp power, exposure

time and frequency determine the overall power density transferred onto the film (31). Current applications of photonic curing include the manufacture of flexible printed electronics (such as RFID and photovoltaics) (32,33), where the manufacturing process requires the thermal treatment or chemical conversion/sintering of a film on a temperature sensitive substrate. Photonic curing has been demonstrated to convert a CuO ink into a Cu thick-film rapidly on a cheap PET substrate, a process which otherwise requires long thermal treatment times in an inert atmosphere (35). In this case no inert atmosphere is required as the energy delivery is faster than rate of copper oxidation. Another application is sintering silver-based inks to improve the conductivity (32) or to improve the electronic properties of ZnO nano-wires (36). This method is most suited to surface treatment and is therefore applied to coatings on a carrier material rather than bulk materials.

1.5 Chapter Closure and Thesis Layout

In this research, photonic curing was explored as a faster means of converting films of phenol formaldehyde resin into glassy carbon. A novel manufacturing process for glassy carbon using a rapid photonic curing method is proposed, which is able to carbonize the coating without adversely affecting the temperature of the substrate whilst decreasing the conversion time from hours to seconds. The converted resin was then compared against a thermally derived glassy carbon. According to the most recently accepted models (4) the structure of GC consists of predominantly sp^2 bonded carbon domains that are disordered graphitic sheets, giving it a comparable structure to fullerene. The randomly oriented graphitic sheets give GC its isotropic nature (3). Raman spectroscopy and X-ray photoelectron spectroscopy were therefore used to elucidate the structure to focus on bulk (microns) and surface (nanometres) respectively given their different penetration depths (38,39), while morphology is compared using a scanning electron microscope.

Both the thermal and photonic cured glassy carbon thin films deposited on stainless steel substrates were investigated as potential anode materials for energy storage devices, either for supercapacitors or batteries. The two glassy carbon films were analysed using cyclic voltammetry, electrochemical impedance spectroscopy and galvanostatic charging and discharging. The performance of the two glassy carbon thin films were compared to each other and to similar materials tested in literature.

Screen-printed thermal cured glassy carbon thin film structures deposited on alumina substrates were used to explore potential applications of glassy carbon in printed

electronics. The electrical conductivity of screen-printed glassy carbon was characterised before potential applications as a temperature sensor and salinity sensor were explored using 2-point probe and 4-point probe setups with a multimeter and electrochemical impedance spectroscopy. The electrical characteristics were compared to literary values of comparable carbon-based conductive inks. The results of thermal cured glassy carbon could not be compared to photonic cured glassy carbon for the electrical characteristics because no photonic cured samples were produced on alumina substrates due to equipment malfunction. After this malfunction, an alternative NovaCentrix PulseForge photonic curing system was tested at a third party (Precision Varionic International, UK). This system was found too low powered for application, as further discussed in Chapter 4.

The aim of this thesis was to highlight the novel ability to produce glassy carbon using photonic curing, glassy carbon's performance as an active electrode material and the potential benefits of using glassy carbon in printed electronics.

Chapter 2: Literature Review

2.1 Introduction

This literature review chapter covers previous works concerning the selection of precursor materials, the structure of glassy carbon, glassy carbon characteristics, glassy carbon production procedures and applications of glassy carbon.

2.2 Structure of Glassy Carbon

Glassy carbon is a non-graphitizing carbon that consists predominantly of sp^2 hybridized carbon-carbon bonds. Glassy carbon is formed by randomly orientated graphitic crystallites making its structure isotropic in nature. Glassy carbon has a relatively low density compared to other carbons due to the inefficient stacking of the crystallites (2–9). The structure of carbons produced by the carbonization of organic precursors is not only dependent on the chosen heat treatment parameters, but also on the structure of the chosen precursor.

By carbonizing any organic precursor between 1000°C and 3000°C, the resultant carbon structure will either be graphitizing or non-graphitizing. A graphitizing carbon is a carbon with weaker crosslinking between the graphitic crystallites, causing these crystallites orientate themselves in anisotropic fashion, producing highly ordered and condensed parallel layers of graphitic crystallites of relatively high density (27,40–43). A non-graphitizing carbon has relatively strong crosslinking between the graphitic crystallites, resulting in a randomly orientated isotropic web-like structure of these crystallites. Due to the inefficient stacking of the non-graphitizing carbon its density is relatively low (~1.5 g/cm^3) compared to the graphitizing carbons (~2.3 g/cm^3) (4,27,40,41,43–45). Graphitizing temperatures are commonly considered between 2500°C and 3000°C but some synthetic graphite can be produced at 2200°C. Graphitizing carbons will show increased order from much lower carbonisation temperatures (1000°C) and slowly become more ordered, dense and graphite-like at the graphitic crystallite level with increasing temperatures (27,40,43). Non-graphitizing carbons will stack in graphite-like parallel groups at graphitizing temperatures, but these groups will remain at random orientations (46). Thus giving these non-graphitizing carbons a slightly more ordered, but still disordered, isotropic structure. Glassy carbon is a non-graphitizing carbon, caused primarily by the crosslinking nature of its resole type thermoset polymer precursors. Glassy carbon carbonized at 600°C, 800°C and

900°C are shown to have randomly orientated groups of parallel graphitic structure of up to 4 layers of 1-2nm in length using HRTEM methods by Jurkiewicz *et al.* (47), confirming glassy carbon's non-graphitizing nature. X-ray diffraction data shows that glassy carbon is made up of randomly orientated stacks of graphene sheets with micropores and a hexagonal-type structure, similar to the structure of carbon black (46,48). Micropores are voids enclosed between layers of graphene sheets, causing glassy carbon to have a relatively low density compared to other carbon materials (49). Harris (4) found that glassy carbon, like other non-graphitizing carbons, may have a fullerene related microstructure due glassy carbon's sp^2 dominated, web-like structure of curved carbon sheets. Yi *et al.* (18), states that the microstructure of glassy carbon consists of discrete fragments of curved carbon planes, aligning with Harris' finds. If the glassy carbon is synthesized at elevated temperatures exceeding 2000°C the structure changes to layered graphite-esque ribbon molecules. A unique aspect of glassy carbon compared to other non-graphitizing carbons is its low reactivity, suggesting a closed particle structure (4,18,50).

The carbon-carbon bonds in glassy carbon predominantly consist of sp^2 hybridized bonds, the reason for glassy carbon's high electrical conductivity. Raman spectroscopy is often employed to show the bond type of carbon materials, because from a Raman spectrum the bond-angle disorder, bond-length disorder and the bond hybridization(s) of carbon-carbon bonds are observed (7,16,29,44,47,51–54). For non-graphitizing carbons (hard carbons), like glassy carbon, the Raman spectra should mainly consist of two dominant peaks, the D band and the G band peaks. The D band is the A1g breathing mode of phonons near the K zone boundary and represents the disorder in the structure of graphitic materials, the peak is found at ~1350 cm^{-1} on a Raman spectrum (52–56). The D band mode is not observed in pure graphite but is activated with disorder and is therefore seen in randomly orientated sheets of curved graphene, glassy carbon. The D band is dispersive, hence its location varies with excitation energy, unlike the G band. The G band is the E_{2g} graphite Raman active mode and represents in the in-plane carbon-carbon bond stretching of graphitic materials and is therefore always found in carbon materials dominated by sp^2 hybridized bonds, such as glassy carbon. The G band peak is located at ~1590 cm^{-1} on a Raman spectrum (52–56). The intensity ratio between these two peaks is related to the graphitic crystallite size (52,53,55,56). sp^2 hybridized carbon-carbon bonds are found in a range of carbon materials from microcrystalline graphite to glassy carbon, varying in degrees of graphitic ordering. Sp^2 hybridized carbon-carbon bonds consist of one short-range σ-bond and one long-range π-bond. Amorphous carbons can also have a G band peak as they consists of a combination

of at least two of the carbon hybridized bonds: sp^1, sp^2 and sp^3 (52). In figure 1, taken from Ferrari *et al*. (52), the different carbon-carbon bond structures are displayed for a range of carbon materials, glassy carbon would be situated at the bottom left of the triangle with the graphitic carbons with sp^2 hybridized carbon-carbon bonds.
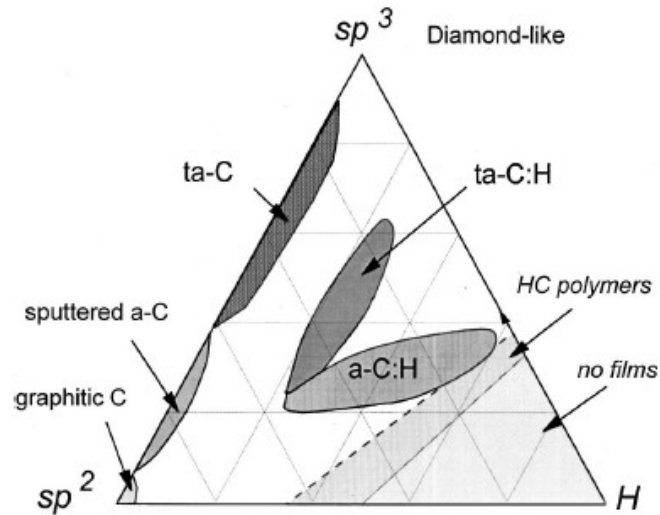
Figure 1. Comparison of carbon materials by their hybridized carbon-carbon bond structures. Taken from Ferrari et al. (52)

Raman spectra of glassy carbon in literature (7,16,29,44,47,51–54) are always found to consist of the D and G band peaks at ~1350 cm^{-1} and ~1590 cm^{-1} respectively. These two primary peaks for glassy carbon are often relatively broad compared to other hard carbons which is attributed to its relatively high crystalline disorder (52). Although for glassy carbon specifically, the FWHM of the primary Raman peaks decrease with increasing heat treatment temperatures, which aligns with the relative increase in order when glassy carbon is produced at higher temperatures (16,51). When using a multi peak Gaussian fit to analyse the Raman spectra it's found that disordered carbons like glassy carbon often have minor peaks hiding under the primary D and G band peaks at 1100 cm^{-1} and 1400 cm^{-1} (52,55). As the intensity ratio between the D and G band peaks is indicative of the graphitic crystallite size, and the graphitic crystallite size grows with heat treatment temperature for non-graphitizing carbons, the intensity ratio is also indicative of the heat treatment temperature used to produce the analysed carbon material. Therefore, an increase in heat treatment temperature results in an increase in the D/G band peak intensity ratio. In figure

2, the image taken from Ferrari *et al.* (52,55), it shown that the G band peak location combined with the intensity ratio between the D and G band peaks can be used to determine the hybridization of the carbon material. Glassy carbon fits in the centre-right section of stage 1 in figure 2, where the structure is dominated by sp^2 hybridized bonds, the G band peak has a location between 1580 cm^{-1} and 1600 cm^{-1}, and the D/G band intensity ratio is non-zero.
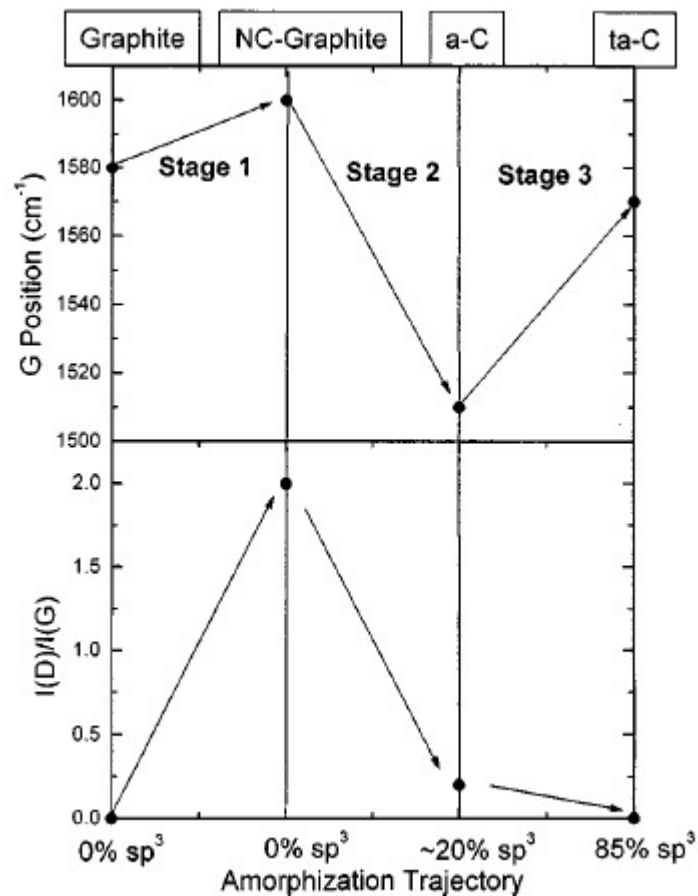
Figure 2. Amorphization trajectory of carbon materials in Raman spectrometry used to predict the hybridization of the carbon-carbon bonds. Taken from Ferrari et al. (52)

In conclusion the broad structure of glassy carbon is known: non-graphitizable, highly disordered, sp^2 hybridized bond dominated, isotropic, randomly orientated, crosslinked graphitic crystallites. These structural characteristics are well defined by material characterization methods such as Raman spectroscopy and X-ray diffraction. But the exact nanostructure of glassy is ill defined, as it has gone through multiple iterations of suspected nanostructures, from the hypothesized graphitic ribbon-like structure by Jenkins *et al.* (46,57,58) to the proposed curved graphene sheets which in turn led to the comparison to a fullerene type structure by Harris (2,4).

2.3 Physical Properties of Glassy Carbon

The structure of glassy carbon yields a carbon material with a unique combination of material properties including substantial hardness, high temperature resistance, impermeability to gases, low electrical resistance, chemical resistance and biocompatibility (2–9).   These properties make it a useful material for electrochemical, corrosion and medical applications among others. Glassy carbon is commonly used as a reference electrode in electrochemistry (5,10–15), as corrosion protection for current collectors (7,16–18) and as a surgical implant material in both humans and animals (8,9,19–21).

The hardness and flexural strength of the glassy carbon changes as a function of carbonization temperature. In the lower carbonization temperature range (600 - 1000°C), it's found that the flexural strength doubles from 600°C to 800°C from ~70 MPa to ~140 MPa, after which it stabilizes around 140 MPa as the temperature is further increased to 1200°C. The hardness of glassy carbon increases with temperature where it reaches a maximum hardness and Young's modulus of 6 GPa and 38 GPa respectively at 1000°C when testing a carbonization temperature range from 600°C to 2500°C (47). Between 1000°C and 2500°C the hardness of glassy carbon decreases with an increase in temperature. The trade-off for the high hardness of bulk glassy carbon material is the high brittleness (18,25).

Glassy carbon's isotropic crosslinked graphitic nano-crystallite structure combined with its non-graphitizing nature creates a material that has high thermal stability well into the graphitizing temperatures, up to 3000°C (2,4,18,19).

Electrical conductivity of carbon materials is determined by the crystal structure, and thus by the carbon-carbon bonds, which means it's determined by the type of hybridized valence orbitals. Glassy carbon predominantly consists of sp^2 hybridized carbon-carbon bonds, resulting in the material to have high electrical conductivity. An sp^3 bonded carbon like diamond or an sp bonded carbon like hydrocarbons have high electrical resistance. (41,52,53,55,59)

Glassy carbon has shown to have both low reactivity and high chemical resistance in a multitude of applications such as electrochemical applications, corrosion protection and medical applications (1, 4–20). The most recent nano-structure of glassy carbon predicting a fullerene-type structure (4,47), suggesting a closed particle structure, aligns well with the low reactivity and high chemical resistance characteristics of glassy carbon. Glassy carbon

has been found to be stable in acidic solutions for several months (2). Glassy carbon also boasts high anodic stability in a multitude of electrolyte and electrode systems. The gas impermeability and low oxidation rate of glassy carbon increase its chemical resistance properties (5–7,17,18).

2.4 Glassy Carbon Applications

2.4.1 Glassy Carbon in Electrochemistry and Corrosion Protection

In electrochemistry glassy carbon has been used in bulk as a working and counter electrode in poisonous organic and acidic electrolytes for its chemical resistance (2,5,7,17). The orientation of the glassy carbon electrode is unimportant because of its isotropic structure. Glassy carbon has a low oxidation rate due to its low reactivity, giving it better chemical resistance, even in acidic and alkaline environments (6). Glassy carbon is capable of relatively wide potential ranges, achieving stability windows of 0 to 4 V against Mg/Mg^{2+} in tetrahydrofuran electrolyte containing 0.5M phenylmagnesium chloride and 0.25M aluminium chloride (7), -0.8 to 1.3V against a saturated calomel electrode in phosphoric acidic electrolyte (5) and 0 to 3V against Mg/Mg^{2+} in tetraglyme electrolyte containing 1M magnesium hexamethyldisilazide and aluminium chloride in a 1:2 molar ratio (17). Standalone glassy carbon electrodes in bulk aren't favoured as working electrodes due to its low chemical reversibility of metal deposition and dissolution, the brittleness of the material and its low cycling efficiency at 55% (7).

Glassy carbon as a coating on non-noble metal current collectors such as stainless steel, aluminium, and titanium makes a more promising prospect compared to the standalone bulk glassy carbon electrode. As a coating on a non-noble metal, glassy carbon keeps the high cycling efficiency of the metal (>90%) while gaining the chemical resistance and the anodic stability from the glassy carbon layer (7,17). The glassy carbon layer would not diminish the electrical conductivity of the metal and can retain some flexibility depending on the carbon layer thickness. Wall *et al.* (17) found that coating aluminium substrate with glassy carbon increased the potential window of the aluminium current collector by 0.8V, giving it a comparable voltage window to bulk graphite. They also found that the glassy carbon coated aluminium had superior current stability over 50 hours of cycling, displaying the chemical resistance achieved by the glassy carbon coating. Yagi *et al.* (7) discovered that glassy carbon coated on stainless steel yields higher current densities than glassy carbon coated on aluminium, titanium or platinum due to the high carbon solubility of

stainless steel. The low carbon solubility of platinum and titanium may have yielded a lower current density but they produce continuous and homogeneous glassy carbon coatings, compared to the stainless steel which can be prone to producing inconsistent inhomogeneous glassy carbon coatings. The tested glassy carbon coatings were of 1μm thickness and were deposited by plasma carburization. The homogeneity of the carbon layer dictates its chemical resistance and is dependent on the substrate material, the glassy carbon coatings of glassy carbon on titanium and platinum displayed much higher chemical resistance compared to the glassy carbon coating on stainless steel (7).

Combining high anodic potentials with high or low pH electrolytes can oxidize the glassy carbon layer, changing the electrochemical performance of the carbon layer. This oxidation can be beneficial to the performance as it could activate the electrode surface, accelerating the electron transfer kinetics, changing the capacitance of the glassy carbon material (18). When glassy carbon is exposed to low pH acidic electrolytes the surface oxidizes due to an acid catalysed electrophilic reaction, producing surface oxides, and thus changing the functional groups on the surface of the electrode. Exposing glassy carbon to a high pH alkaline electrolyte oxidizes the edges of graphitic crystallites until they're hydrophilic enough to dissolve in the electrolyte. Compared to glassy carbon in a neutral pH electrolyte, the acidic electrolyte induced oxidation increased the capacitance of the electrode by factor 10 in 10 hours of exposure, whereas the alkaline electrolyte induced oxidation halved the capacitance but stabilized the capacitance as a function of time. This shows that glassy carbon isn't chemically inert but has high chemical resistance (18).

2.4.2 Glassy Carbon in Medical Implants

The chemical resistance and low reactivity of glassy carbon is not only useful in electrochemical and corrosion applications, glassy carbon has been explored in depth by Bokros, Lewis *et al.* and Markle *et al.* in the 1970s for medical devices such as implants and filters because of its biocompatibility (8,9,19–21). After extensive studies of GCs compatibility with soft tissue, blood and bone it is found that glassy carbon has no inflaming effects on neighbouring tissues. A long-term toxicology and carcinogenic study by Bokros (8) reveals that glassy carbon doesn't interact or respond to major organs, tissues, blood and urine, suggesting that glassy carbon is safe to use for biomedical devices such as teeth-root implants. No inflammation or foreign-body reactions seem to occur between glassy carbon and human tissues (8). Glassy carbon's biocompatibility with blood is assumed completely antithrombogenic or passive like pyrolytic carbon due to the

similarities in the surface structures (8,18). Glassy carbon does not fail in fatigue for medical devices because it does not have any mobile defects in its structure at room temperature and thus there is no movement mechanism to initiate fissures. In medical terms, glassy carbon has a relatively high impurity count when produced using conventional thermal carbonization of thermoset resin precursors, up 2000ppm of ash is detected on average. This level of impurity is unusable in biomedical devices and thus as a benchmark of glassy carbon with impurities under 100ppm are of acceptable purity (8).

Fibres made of glassy carbon or fibres coated in GC may be utilized to filter blood before it is transferred into another living body. The fibres diameter ranges between 1 and 100 microns to effectively filter the blood (20).

Glassy carbon has been applied to dental surgery and for percutaneous connections, particularly in skin penetrating operations using a needle rather than scalpel. Glassy carbon tooth-root implants have shown healthy tissue growth post-surgery as the tissue seems to be able to grow closely to the glassy carbon surface which enables strong fixation between the glassy carbon and tissue interface. Whether gum tissue bonds to the glassy carbon surface is unverified, but glassy carbon has shown to promote new tissue growth (8,21).

The ability to polish the glassy carbon surface allows high precision biomedical applications such as heart-valves and occluders to be manufactured from this carbon material. The biocompatibility of glassy carbon at air-tissue interfaces makes it an ideal material for percutaneous connections. Hollowed glassy carbon cylinders are utilized in vein and artery connections (8,21).

The glassy carbon implants are shaped by a combination of setting of the precursor resin in a mould followed by machining the moulded precursor to its final dimensions. Machined perforations and serrations in the set resin allows tissue to grow and integrate with the implant. During machining, fissuring of the biomedical device was found to be unavoidable but it's inconclusive whether this is due to the dimensions of the part or the stress imposed on the part by machining. Boron-doped glassy carbon is proposed as a study to achieve dimensional stability at larger dimensions (21).

2.4.3 Glassy Carbon Crucibles

Glassy carbon's high thermal stability for temperatures up to 3000°C combined with the low reactivity due to the unique nature of its structure makes glassy carbon a desirable

material for the manufacture of crucibles (2,4,18,19). There are not many applications where crucibles must be taken outside of glassy carbon's thermal stability range and the low reactivity avoids any contamination between the crucible and the sample during heat treatment, whether that's in air, inert atmosphere or in a vacuum.

To produce a glassy carbon crucible, the shape may be moulded using the precursor resin or machined out of a block of set phenolic resin precursor. The resultant set precursor crucible shape then undergoes carbonization in an inert atmosphere, resulting in a glassy carbon object of predetermined dimensions. Alternatively a crucible manufactured using graphite may be coated with glassy carbon to avoid contamination with samples during experiments or production of materials such as silicon crystals (18,19).

2.5 Precursors to Glassy Carbon

Glassy carbon can be produced with the carbonization of resol type thermosetting precursors such as phenol formaldehyde, polyfurfuryl alcohol and acetone furfuryldehyde (22,24,28,29,61–64). Phenol formaldehyde is the most common precursor resin to glassy carbon in literature.

Phenol formaldehyde can have different characteristics dependent on how the two monomers are synthesized together. The final phenol formaldehyde composition is dependent on manufacturing parameters such as monomer molar ratio, catalyst type, temperature, acidity and monomer excess percentage. These parameters dictate whether the resultant phenol formaldehyde is a novolac or resol type resin (22,23,62,65). Novolac resins are produced in an acidic environment whereas resol resins are produced in an alkaline environment. With molar ratios where the phenol monomer is in excess of the formaldehyde (P/F > 1), combined with an acidic pH the resultant phenol formaldehyde is a novolac type resin. If the molar ratio is dominated by the formaldehyde monomer (P/F < 1), and the addition is made in an alkaline environment, the phenol formaldehyde is a resol type resin. A molar ratio of 1.45 to 1.60 of formaldehyde per phenol monomer yields the higher carbon content after carbonization (23,24,50). Both the novolac and resol type resins are stable at room temperature but are cured with the application of heat (63,64). The crosslinking bond type of the novolac is a methylene link (-CH_2-), whereas the crosslinking bond type of the resol type resin is a ether link (-O-) (21,22,66,67). The crosslinked structure of the resol type phenol formaldehyde resin consists of three functional phenols and two functional methylenes. Of these groups the main oxygen

carrying group with the ether links is phenolic hydroxyl (68). The difference in bond structure causes these two resins to form distinctly different carbons when exposed to carbonization conditions, elevated temperatures in an inert atmosphere. Carbonizing a novolac resin results in a graphitizing carbon, more commonly known as a soft carbon. A graphitizing carbon will yield graphite when exposed to temperatures ranging from 2000-3000°C. Carbonizing a resol resin on the other hand, produces a non-graphitizing carbon, better known as a hard carbon, when exposed to a carbonization environment (22). Phenol formaldehyde as a carbonization precursor produces one particular kind of hard carbon: glassy carbon.

2.6 Thermal Carbonization of Precursors to Produce Glassy Carbon

Thermal carbonization of the precursors to produce glassy carbon starts with polymer deposition, the deposition method depends on the desired geometry of the final glassy carbon product (26). Resol type precusors are permanently crosslinked by way of heat or catalyst, so that the precursor is thermoset. Temperatures for thermosetting these resins are in the range of 100°C to 300°C (19,28,50). Hexamine is the most common catalyst for curing phenol formaldehyde resins (21,57).

The carbonization of one of the resol type thermosetting polymer precursors produces glassy carbon of varying qualities dependent on the chosen parameters during heat treatment. These parameters include ramp rate, set point temperature, choice of inert atmosphere and inert gas flowrate (25,26,50).

Of these parameters the set point temperature, or heat treatment temperature, is the parameter with the greatest impact on the resulting qualities of the glassy carbon and is therefore most widely covered in literature. From published XRD and Raman spectra, it's found that the precursor phenol formaldehyde start to carbonize in bulk at heat treatment temperatures exceeding 600°C (25), with the majority of the literature exploring temperatures in the 800°C to 2000°C range (4,19,26,28,46,50,57,69,70). From the carbonization literature referenced previously, it's found that in the temperature-stage up to 600°C during the carbonisation process, the organic (oxygen dominated) molecules are removed from the precursor as off gases. This causes the precursor to temporarily turn into a hydrocarbon before completing its carbonization. When glassy carbon is produced by carbonizing at a lower heat treatment temperature, a larger amount of oxygen remains in the final carbon material (53,68). In the temperature range 600°C to 1200°C, hydrogen is

removed from the carbon, producing a glassy carbon of increasing density (6,21). Depending on the precursor, heat treatment temperature of 600°C to 1200°C result in a volume reduction of 40% to 50% (6,24,28,30).

During the carbonization process, gases diffuse from the solid precursor and thus there is risk of fracturing the solid if this occurs at too high a rate. High heating rates would keep the gases inside the carbonized material yielding increased internal pressure and causing voids, cracks and other physical distortions resulting in a decrease in mechanical performance. The choice of ramp rate, the speed at which the temperature is increased, is therefore an important parameter to maintain the structural integrity of the resultant glassy carbon (6,21). Ramp rates in literature generally vary in the range of 0.1°C/min to 5 °C/min (21,28,30,70).

The carbonization must occur in an inert atmosphere, which may be achieved through different methods. The two most common methods are by flushing a furnace with an inert gas such as nitrogen or argon, commonly with a flow rate ranging between 0.1L/min and 2L/min (26,30,70). A less common method is to heat treat the precursor in a vacuum at carbonizing temperatures, but this method yields a similar result in carbon quality (26).

2.7 Photonic Curing as Potential Carbonization Method

Photonic curing is an alternative technology to the conventional convection oven which currently sees most use in the drying and sintering of printed or coated thin films as it delivers energy specifically to the surface of the sample using high intensity light, contrary to a convection oven which delivers energy to the sample through heat by raising the ambient temperature (31–36). In this thesis photonic curing is explored as an alternative method of carbonizing precursor to glassy carbon to produce glassy carbon thin films. This method is attractive for both the speed of production and the ability to use temperature sensitive substrates. Photonic curing is most suited to surface treatment and is therefore applied to coatings on a carrier material rather than bulk materials.

Photonic curing uses xenon lamps to rapidly pulse high-intensity light of wavelengths in the visible spectrum, transferring a high energy density to the surface of an object (31). Photonic curing minimizes the thermal treatment times while allowing conventional oven-comparable temperatures to be reached at the surface of the exposed object (32). The reduction in time is achieved because there are no requirements for ramping, holding or cooling times as the energy delivery using light is almost instantaneous. An example from

Cronon *et al.* (37) where photonic curing is used to sinter aqueous silver inks shows a reduction in curing time from 90 minutes to 9 ms.

Other radiative heating techniques such as UV curing and Near infrared heating (NIR) use light of shorter and longer wavelengths respectively. Lower wavelengths of light yield higher energy transfer, thus making the techniques using lower wavelengths more viable options for carbonization. A potential advantage of using photonic curing over the other radiative heating techniques is the ability to flush the heating chamber with an inert gas to create an inert atmosphere (108). In the case of producing glassy carbon coatings the carbonization in an inert atmosphere is a requirement, making photonic curing the radiative heating technique of choice.

Photonic curing can also be integrated with roll-to-roll processing (33) and the curing speed allows for a decrease in physical space required in automated, in-line manufacturing as it would replace an otherwise large heat or radiation curing oven (34). The localised and transient nature of photonic curing also enables the potential use of low-cost, flexible, temperature sensitive components/carrier substrates to be used for thin and thick carbon films that ordinarily could not withstand conventional thermal treatment (34).

Photonic curing pulse parameters, such as lamp power, exposure time and frequency determine the overall power density transferred onto the film (31). Current applications of photonic curing include the manufacture of flexible printed electronics (such as RFID and photovoltaics) (32,33), where the manufacturing process requires the thermal treatment or chemical conversion/sintering of a film on a temperature sensitive substrate. Using photonic curing to sinter metal nanoparticles and metal-based inks can make them conductive, if they were not conductive before, or improve the conductivity (71), as such photonic curing is also often identified as photonic sintering.

Photonic curing of polymers degrades the polymers at rates dependent on the chosen parameters that affect the energy density output, such as lamp voltage, lamp limit, exposure time and pulse frequency (108). Photonic curing can therefore be used to remove the polymeric binder from conductive inks. The polymeric binder in conductive inks decreased the theoretical electrical conductivity of the active material in the ink so removing the binder completely or partially using photonic curing increases the electrical conductivity of the ink (36,71). Further benefits of using photonic curing to dry inks or remove binder from inks include improved surface roughness and edge resolutions.

Photonic curing can produce adverse effects on inks, such as decreasing the layer adhesion and cohesion and thus a loss in layer structural integrity. A suggested solution to this problem is the use of post-process compacting methods by Potts *et al.* (71)

Photonic curing has been demonstrated to convert a CuO ink into a Cu thick-film rapidly on a cheap PET substrate, a process which otherwise requires long thermal treatment times in an inert atmosphere (35). In this case no inert atmosphere is required as the energy delivery is faster than rate of copper oxidation. Another application is sintering silver-based inks to improve the conductivity (32) or to improve the electronic properties of ZnO nano-wires (36).

A similar method of rapid thermal annealing of glassy carbon as a post treatment after the glassy carbon has been carbonized using a conventional thermal heat treatment procedure is introduced by Lim *et al* (53). The use of UV lamps is introduced as rapid thermal annealing (RTA), a process which is most commonly used in producing silicon wafers. Using RTA as a post-processing treatment is shown to increase the electrical conductivity by approximately 300% compared to untreated glassy carbon. This RTA method is performed in a vacuum. After RTA treatment, glassy carbon that initially was of lower heat treatment temperatures containing a higher oxygen count, achieved better electrical conductivities than glassy carbon of higher carbonization temperature with a lower oxygen count. RTA could therefore be a cost and time effective alternative addition to the conventional thermal carbonization process to produce glassy carbon (53).

2.8 Chapter Closure

From this literary review, it has been identified the majority research into glassy carbon is relatively old and that the manufacturing method of the material hasn't changed in the last decades. Photonic curing is an alternative surface treatment method that suits thin film applications, using it to carbonize an organic precursor to a carbon is previously unexplored.

Glassy carbon has been explored as corrosion protection of current collectors but has not been extensively studied as an active material on a current collector for energy storage applications such as supercapacitors or batteries. Glassy carbon thin film coatings produced

through both thermal carbonization and photonic curing as active electrode materials on current collectors are novel applications of the materials.

Some work has been done using glassy carbon microstructures in micro-electromechanical systems by moulding the precursors to shape. Literature review has also identified that screen printing of the organic precursor in liquid form to achieve specific structures for electronics applications before carbonization of the precursor has not been explored. In conclusion, this review exposes a gap in the literature for rapid glassy carbon manufacturing, and in the use of glassy carbon in printed electronics.

Chapter 3: Experimental Apparatus and Materials

In this chapter the choice of materials, precursor deposition methods, carbonization methods and characterization methods that were used in the research for this thesis are discussed.

3.1 Materials

3.1.1 Resole Type Thermoset Resin - Phenol Formaldehyde

From the literary review in chapter 2, it was identified that the organic precursor to produce glassy carbon must be a resole type thermoset resin, most commonly phenol formaldehyde or furfuryl alcohol. The selected precursor for all the glassy carbon manufacture in this thesis was Curaphen 40-852 B60, a resole-type thermoset polymer resin supplied by Bitrez Limited (UK). This precursor is a phenol formaldehyde resin in a combination of solvents to make it printable such as butan-1-ol, xylene and m-cresol. As received, this resin is flammable and has acute toxicity level 4, skin irritation level 2 and eye damage level 1, thus great care was taken in handling this material. Any usage of the material was performed in a fume cupboard, while wearing a full face mask (3M model 6000 with 3M model 6099 particulate filters for added protection). Characteristics of this resin are given in the SDS as a 45°C closed cup flash point, a relative density of 1.005 at 25°C and a dynamic viscosity of 1P at 25°C. Upon exposure to air the resin quickly increased in viscosity as the solvents evaporate, this particular resin was printable for about 5 - 10 minutes in air. This led to restrictions to the number of prints that could be made in any one session.

3.1.2 Substrate Materials

Two metal based conductive substrates, 316 stainless steel and aluminium, were chosen to be used as substrates for glassy carbon thin films due to their common use as current collector materials in energy storage applications. The conductive substrate was required for some of the characterization and application testing. The selected steel substrate for the precursor deposition was 316L stainless steel foil of 25μm thickness (Advent Research Materials (UK)) and the selected aluminium substrate for precursor deposition was aluminium foil (99.2% purity) of 25μm thickness and 100x100mm area (Advent Research Materials (UK)).

Two ceramic non-conductive substrates, alumina and glass, were chosen to be used as substrates for glassy carbon thin films to perform all the conductivity testing to remove any potential interference to the data that a conductive substrate might have. The chosen alumina substrate was alumina plate 10x8cm (Sigma Aldrich, UK) of thickness 640μm. The chosen glass substrate was 120x120mm glass plate of 2mm thickness (C.G. Tofts Glaziers, UK).

3.2 Deposition Methods

3.2.1 Bar coating

Bar coating was used to produce consistent layers of precursor on stainless steel for carbonization testing, the deposition method of bar coating was chosen for its fundamental simplicity in terms of mechanism and parameters. The phenol formaldehyde precursor resin was coated onto the steel foil substrate using bar coating (PrintCoat Instruments K Control Coater) as shown below in figure 3. Close-wound bars sizes "0, 1, 2, 3 and 4" (0.05, 0.08, 0.15, 0.30 and 0.51mm wire diameters respectively) were used yielding a theoretical wet coating thicknesses of 4, 6, 12, 24 and 40 microns respectively at a speed of circa 1.1 m/min. Two different coating thicknesses were used as a result of preliminary tests which revealed the structural integrity limitations of the phenol formaldehyde coatings during the heat treatment stages. The thicker coating (12 micron wet) was used in the conventional thermal conversion because that method experienced delamination with thinner coatings, while thin coatings (4 micron wet) were used for the photonic curing method which experiences delamination for thicker coatings. These limitations were specific to the materials and methodology used in this thesis. Ambient temperature and humidity in the fume cupboard during coating was constantly kept at 22°C and 33% respectively.
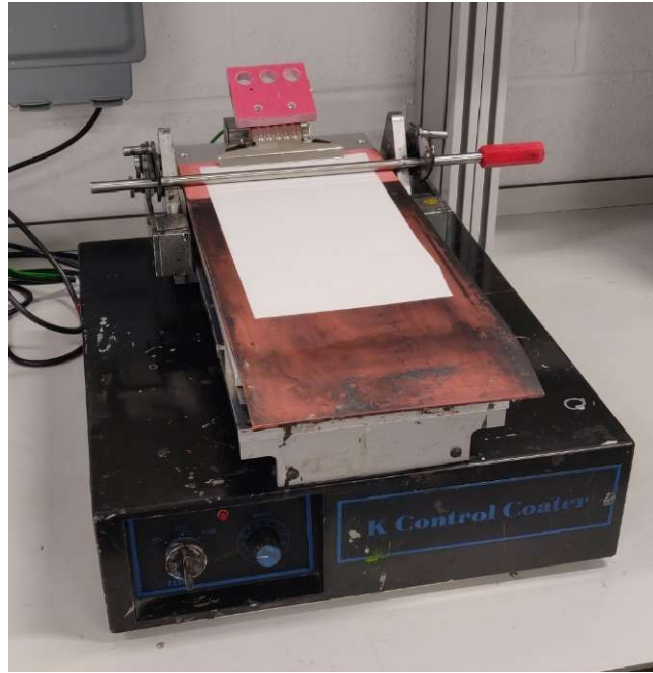
Figure 3. K Control Coater by PrintCoat Instruments used for all the bar coating work required in this work.

3.2.2 Screen printing

Screen printing as a deposition method was utilized to produce custom geometries of printed material on a substrate. In this thesis, to study the electric conductivity of glassy carbon and the viability of it in applications such as conductive tracks, a temperature sensor and a salinity sensor, screen printing was used to deposit the precursor phenol formaldehyde resin onto the non-conductive substrates, glass and alumina. The custom screen was designed in Adobe Illustrator and then ordered from and manufactured by MCI Precision Screens (UK), both the design and the screen are shown in figure 4 below. Technical specifications of the screen are an 8x10 inch frame with a 77 mesh and a 55-micron thread, yielding a theoretical wet deposition layer of 13µm. This mesh was chosen to reproduce the conversion success attained with the 12µm wet deposition bar coating as further discussed in chapter 4.1.3.
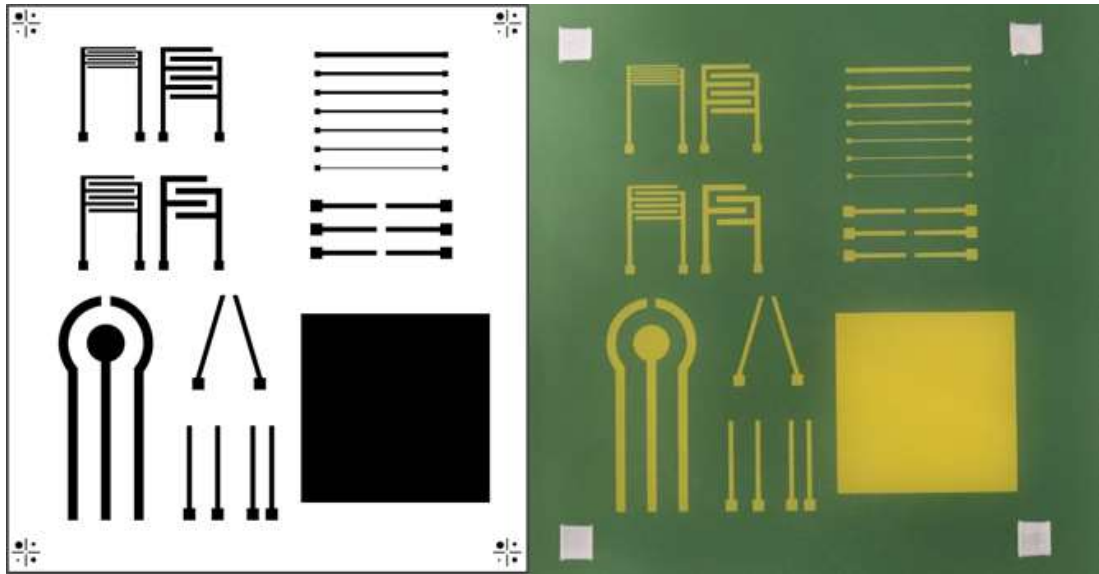
Figure 4. Screen design made in Adobe Illustrator on the left. Screen as supplied by MCI Precision Screens on the right.

Due to the toxic nature of the precursor, the screen printing was done by hand in a fume cupboard rather than using an automated screen printer. This resulted in the need for separation between the mesh and the substrate in order to achieve a good quality print, this separation is usually a printing parameter which may be customized when using a screen-printing machine. In figure 5, 3D printed spacers that fit the edge of the screen frame are shown. These home-made spacers created a distance of 3mm between the mesh in the substrate which resulted in good, repeatable hand screen printing results on ceramic substrates. To attach the spacers to the frame the hole seen in figure 5 was tapped so that it could be bolted to the frame from the top, enabling the user to manoeuvre the frame during printing without losing the spacing consistency, especially when moving the screen between substrates with the precursor resin deposited on top of the mesh.

Figure 5. 3D printed spacers for the screen-printing frame. Close-up of one spacer on the left. All 4 spacers bolted to the frame using bolts and spacers on the right.

When hand screen-printing the phenol formaldehyde resin precursor was deposited in a horizontal line via pipette above the start of the apertures in the mesh, the squeegee in its metal housing was kept as level as possible, whilst applying constant downward pressure to create contact between the bottom of the mesh and substrate. The print speed was kept as constant as possible by hand, attempting to keep as similar speed to the bar coating at approximately 1m/min.

3.3 Conversion to carbon methods

3.3.1 Precursor Thermoset Resin Curing

After depositing the precursor phenol formaldehyde resin, by bar coating or screen printing onto a metallic or ceramic substrate, the resin must be thermoset at elevated temperatures in air before the carbonization process. The "wet" resin can't go into carbonization directly as the crosslinking caused by the thermosetting of the resin is what determines the carbonized structure after heat treatment. This thermosetting was achieved by taking the coating and substrate to 220°C in air for 30 minutes as was suggested by the manufacturer of this particular Bitrez Curaphen resin, which for all the coatings produced in this thesis was done in a ventilated Votsch VTL 60/90 oven.

3.3.2 Thermal Conversion to Carbon

To carbonize the precursor phenol formaldehyde into glassy carbon, the heat treatment must take place in an inert atmosphere as discussed in section 2.6 the literature review. Therefore, the ideal oven type for the heat treatment and carbonization to produce glassy carbon is a tube furnace. The relatively small, heated volume compared to an ordinary convection oven means less time and nitrogen gas is wasted in turning the atmosphere in the tube inert. In the picture in figure 6 the tube furnace setup is shown, the nitrogen gas was supplied to the fume cupboard by the university gas system and was connected to the tube furnace via a flow meter to accurately determine the amount of gas travelling through the furnace as this was an important experimental parameter. Below the metal safety grating, protecting the user from the heating elements, is the temperature control unit, this is used to set all the heat treatment parameters before use. On the left-hand side of the image, a rubber tubing gas outlet from the furnace goes into a glass container with water, this allows the user to observe whether the gas is flowing through the tube without any leaks in the seals of the metal hardware on the ceramic tube, it also catches any potential particulates that may come out with the nitrogen gas as it exits the tube furnace. As

mentioned, the entire tube furnace with accessories was positioned inside a fume cupboard so that any potential hazardous gases coming off the precursor phenol formaldehyde resin during heat treatment may be extracted. Samples of the printed precursor on one of the selected substrates were cut to size to fit the 103x51mm alumina crucibles to minimize chance of contamination and to hold the sample in place with the nitrogen gas flowing through the tube furnace.

Figure 6. Tube furnace setup for thermal curing carbonization process. Nitrogen gas intake on the right-hand side with a flow meter, gas outlet to the left hand side into a glass container with water to catch any potential particulates.

The conventional method of producing glassy carbon is heat treatment of the cross-linked phenol formaldehyde precursor in an inert atmosphere. For this work, the coated phenol formaldehyde resin samples were exposed to a set point temperature of 800°C which was reached at a ramp rate of 2°C per minute in a tube furnace (Carbolite GERO GHA 12/450) with a holding time of 2 hours. An inert atmosphere in the furnace was achieved with a constant 1 L/minute flow of nitrogen gas. This tube furnace required temperatures of <50°C to be opened, hence resulting in long average cooling times of ~12 hours. These parameters follow conventional processes as established in literature (24–27,30,47). A maximum carbonization temperature of 800°C was selected to prevent excessive softening of the steel carrier substrate.

3.3.3 Photonic Conversion to Carbon

To carbonize the phenol formaldehyde precursor into glassy carbon in a fraction of the time of the thermal conversion method, photonic curing was explored as a way to deliver enough energy to the precursor to push it over the carbonization threshold.

For the photonic curing method, the coated phenol formaldehyde resin samples were heat treated using a photonic curing system (Novacentrix PulseForge 1200, Austin TX). The selected pulse parameters for carbonization were developed via preliminary testing and were a lamp voltage of 450V and a pulse duration of 20,000 µs giving an energy output of ~27 J/cm^2 per pulse calculated by the onboard computer software by Novacentrix. Preliminary studies included a range of variables such as lamp voltage, frequency, and pulse duration. Multiple pulses were performed, up to a maximum of 20 pulses (5,10,15,20 pulses), at a frequency of 0.3 Hz, and at range of lamp voltages from 250V to 450V. The sample resided in a dedicated sample holder with a transparent glass window as seen in figure 7. The sample holder was continually vented with nitrogen gas to achieve an inert atmosphere and remove the evolving off-gases during treatment. The steps required for both treatments are demonstrated graphically in figure 8. The total heat treatment cycle of the conventional method takes >20 hours whereas the photonic curing method requires up to 64 seconds (depending on the number of pulses).
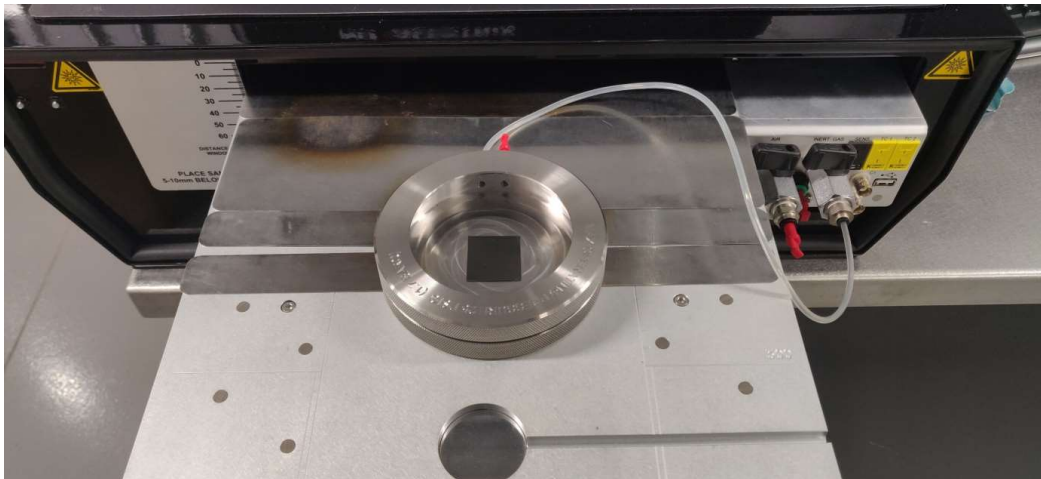
Figure 7. Converted carbon coating (~3x3cm surface area) placed in the photonic curing sample holder attached to the nitrogen gas supply
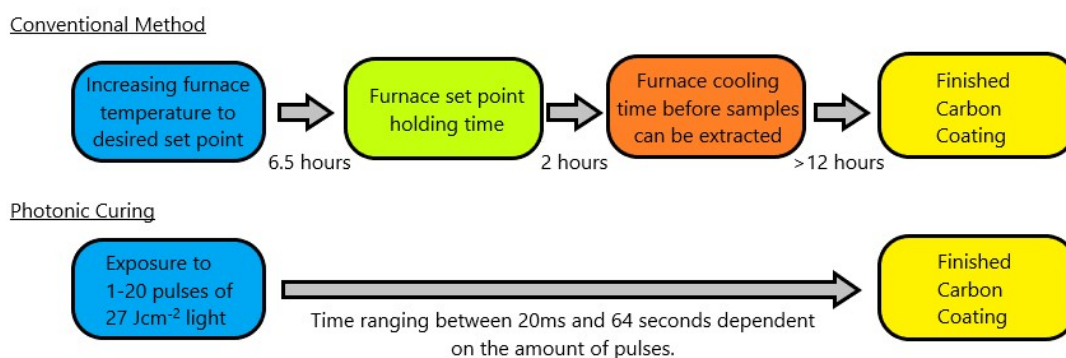
Figure 8. Breakdown of the time requirements of the iterative steps to complete both heat treatment methods

3.4 Characterization Methods

This section is dedicated to all the characterization methods used in this thesis to compare the two glassy carbon thin films produced using thermal and photonic curing, as well as to compare the measured characteristic to those found in literature.

3.4.1 Rheometer

The rheology of a material determines the type of printing and/or coating that may be employed to deposit that material. The viscosity of the phenol formaldehyde precursor resin (Bitrez Ltd, UK) was measured using a Malvern Kinexus Pro+ rheometer (Malvern Instruments, UK) with a 55mm cone with a 2° angle and parallel plate at 20°C ambient temperature. The viscosity was measured across a shear rate increasing from 0.1 to 100 s^{-1} and then reduced back to 0.1 s^{-1}. Three measurements were taken of the phenol formaldehyde precursor to average results. Rheological tests were performed by Alaa Alaizoki in Candidate's presence and support. Rheology data included for completeness of research and as used for guidance in development of deposition methods.

3.4.2 Gas Chromatography - Mass Spectrometry

Gas chromatography - mass spectrometry (GC-MS) has a wide variety of potential applications due to its ability to analyse any material down to their fundamental chemical composition. Gas chromatography (GC) is an analytical method which determines all molecular substances in complex chemical mixes, most commonly used in organic

chemistry. Mass spectroscopy (MS) is a detection method which determines and identifies molecules directly, thus yielding the most direct data possible. For this reason, MS is often used as a reference for other identification techniques. GC-MS has a sample analysis limitation where the analysed substance must have volatility high enough so that there's enough vapour present to analyse. Pyrolysers are often added to the GC-MS system to vaporise substances that would otherwise have too high a boiling point for the GC-MS to detect (72). Applications range from forensic and environmental analysis such as the detention of anabolic steroids in cough syrup (72), to medical research into different constituents of cannabis (73), to the investigation of microplastics retrieved from the ocean to attempt to tackle that aspect of our pollution footprint (74)

For the pyrolysis-GC-MS analysis performed for this thesis a PerkinElmer Clarus 600T machine was used with the Pyris software package. A pyrolyser was attached to the GC-MS system to analyse the precursor as it went through carbonization (pyrolysis in an inert atmosphere by way of nitrogen flow). A continuous ramp rate of 2°C/min was set using pyrolyser, enabling the GC-MS data to determine what compounds were removed from the precursor at specific temperatures and to observe percentage mass change of sample with temperature, including a 2 hour holding time at set point to mimic the thermal curing conversion process. The substance identification was divided up into 3 temperature sections: 20°C to 300°C, 300°C to 500°C and 500°C to 800°C.

3.4.3 Stylus Profilometry

The most fundamental of methods of investigating the topography of a surface is by way of stylus profilometry. The method consists of a stylus, which is parallel to the normal of the sample stage plane, which moves across the surface of a sample with a certain downward force and at a certain speed, dependent on how sensitive the investigated features of the sample are. The resolution of the measurements of stylus profilometry are dependent on the scan parameters and the geometry of the stylus, as the stylus is in physical contact with the sample this method has the potential of being a destructive analysis method. Stylus profilometry was used to measure surface roughness, film thickness and printed line cross-sectional areas of glassy carbon thin films produced for this thesis.

In this thesis all stylus profilometry was performed using a KLA Tencor D-600 with accompanying software. Settings were kept consistent at a scan rate of 0.05mm/s, a stylus

force of 10.0mg with a height range of 10 or 100µm and a scan length between 2 and 3mm depending on the sample.

3.4.4 Optical Profilometry - White light Interferometry

White light interferometry is an optical profilometry method to study the topography of a sample. Widely used to measure surface roughness and profiles of substrates and printed materials, white light interferometry offers a faster and non-destructive alternative to the previously discussed stylus profilometry. White light interferometry works by firing a beam of white light through a beam splitter, of which part of the beam goes to the sample and the other goes to a reference mirror. The reflected light off the reference mirror and the sample are observed by a detector, of which the data is interpreted by a computer to create a 3-dimensional image of the sample compared to the reference sample. Thus if the sample beam doesn't reach the detector an image can't be formed of the sample, and therefore the optical profilometry method comes with limitations on the type of sample it can reliably analyse depending on the colour, opacity and surface structure of the sample. For example, due to the colour, pore size and geometry of the alumina substrates used in this body of work, the amount light reflected back to the detector was too small to create a 3-dimensional image of any print on this substrate, hence for prints on this substrate the stylus method was used. The digital image is built up in layers and so the machine takes multiple images using a set interval Z step distance accompanied by a set Z range in which the machine will record images to form the eventual complete 3D image.

White light interferometry (NT2000, Veeco Instruments, Inc., Plainview, NY, USA) was used to measure a full three-dimensional surface profile over the coated surfaces. 20 times magnification was used, giving a measurement area of 232 µm by 310 µm (at a resolution of 640 × 480 pixels with sampling at 485 nm intervals).

3.4.5 Scanning electron microscopy

Scanning electron microscopy (SEM) is a non-destructive microscopy technique used to analyse the surface topography of a material. SEM as a method has advantages over conventional optical microscope such as the ability to take images up to 100,000X magnification at high resolution compared to the maximum 1,000X magnification you typically see in an optical microscope. SEM has a larger depth of field at high magnifications compared to an optical microscope due to the nature of its detection mechanism, hence it produces higher quality images with the majority of the sample surface in focus regardless

of the surface roughness, whereas the optical microscope relies on the sample being smooth at high magnification for the image to be in focus (75).

In this study the SEM data was used for the surface topography only. Scanning electron microscopy (JEOL 7800F with Oxford Instruments Aztec EDS system XMaxN detector field emission gun scanning electron microscope (FEGSEM)) was used to determine the surface topography of the carbon coatings.

3.4.6 Raman Spectroscopy

As discussed in literary review section 2.2, Raman spectroscopy is a key method for identifying carbon materials by determining their crystalline bond structure.

When the monochromatic light from the laser of a Raman spectrometer is incident on the molecules of the investigated sample, the photons undergo elastic and inelastic scattering. The elastic scattering, Rayleigh scattering, produces light of the same wavelength as the incident photons but the inelastic scattering produces photons of different wavelengths dependent on the rotational, vibrational and electronic energies of the excited molecule (76). Inelastic scattering of light by low frequency lattice vibrations is known as Brillouin scattering. Raman spectroscopy is a characterisation technique that exploits this Brillouin scattering in a medium to study structure and electronic properties of a material (77).

There are molecular selection rules to determine whether a molecule is optically active. A transition such as Raman spectrometry is allowed if the transition moment integral is nonzero. If the transition moment integral is non zero, it means the vibration due to the Raman interaction changes the polarizability of the molecule (52). In this thesis this is helpful because the phenol formaldehyde precursor is not Raman active and the glassy carbon after carbonization is Raman active, thus yielding a method to check carbonization.

Raman spectra of the carbon coatings were compared using a Renishaw inVia Raman system (Renishaw plc., Wotton-Under-Edge, UK) in backscattering configuration with a 50x objective lens (NA: 0.50, spot size ≈ 1 μm) The spectrometer used a laser of 532 nm excitation wavelength with a maximum power output of 32 mW. The spectrum acquisition parameters were set to 5% laser power (=1.6 mW), 10 second exposure time and a grating of 1800 lines/mm. Raman spectroscopy of this particular wavelength penetrates approximately 0.7-1.0 microns in carbon materials which aligns with the typical coating

thicknesses used in this study and therefore is representative of the bulk morphology of the coating (38,39).

3.4.7 X-ray Photoelectric Spectroscopy

X-ray Photoelectric Spectroscopy (XPS) determines the elemental composition and the bond types by measuring the binding energies present in a material. For carbon this can be used to analyse the composition of the hybridized carbon-carbon bonds in the studied sample.

XPS analysis works on the principle of the photoelectric effect that a material will emit electrons when it is excited by electromagnetic radiation. An monoenergetic x-ray is fired at a material resulting in the material to emit an electron of with a certain kinetic energy. For the electron to be emitted it must first overcome the binding energy of the atomic orbital from which the electron originates. The energy of the phonon (X-ray) must be equal to the kinetic energy and the binding energy of the electron. The phonon energy is predetermined and the XPS machine measures the kinetic energy of the emitted electron, enabling it to calculate the binding energy the electron had to overcome to be emitted. This binding energy allows us to characterize the material because these binding energies are specific to combinations of types of orbitals that are unique to every element. While these x-rays have a penetration depth range of 1-10 microns, the photoelectrons only travel in the range of nanometres due to their probability of colliding with matter being far greater than that of the phonons. Therefore the electrons of which the kinetic energy is measured must come from within the first few nanometres from the surface, making XPS a surface characterisation technique (78).

For the data presented in this thesis, X-Ray photoelectron spectra (XPS) were obtained using a Kratos Axis Supra (Kratos Analytical, Manchester, UK) using a monochromated Al Kα source (225W power). All spectra were recorded without using a charge neutraliser. Survey scans were recorded at a pass energy of 160 eV and the high resolution data at 40 eV with energy steps of 0.1 eV. The emission current was set at 15mA. Peaks were identified and quantified with Shirley backgrounds and GL(50) line shapes, with carbon D-parameter analysis performed as outlined by Kaciulis (79) using CasaXPS Version 2.3.22PR1.0. The photon penetration depth of XPS lies in the range of 5-10 nm (38,39), so that XPS is primarily a surface characterisation method rather than being representative of the bulk.

3.4.8 Electrochemical Characterisation (CV, EIS, GCD)

To study the electrochemical characteristics and performance of the carbon coatings produced via both the thermal carbonization and the photonic carbonization methods, a half cell setup was used where the carbon coatings are the working electrode in conjunction with a silver/silver chloride reference electrode and a platinum wire as a counter electrode in a 0.5M sodium sulphate aqueous solution. This reference and counter electrode combination is chosen due to the nature of the electrolyte being aqueous. The electrolyte was de-oxygenised using a bubbler setup with a flow meter as shown in figure 9. The electrolyte was de-oxygenised for 2 hours using nitrogen with a flow rate of 0.5L/min.

Figure 9. De-oxygenising bubbler and flowmeter setup to remove oxygen from electrolyte

A half cell testing setup consists of three electrodes: the working, reference and counter electrode as shown in the image in figure 10. The working electrode (WE) is the studied electrode, thus in this case the thermal and photonic cured carbon layers are the working electrodes. The reference electrode (RE) provides a reference potential difference to the system, hence half cell data always shows the voltage measurements against a specific material, in the case of this study it's against the potential of the silver/silver chloride ($Ag^+/AgCl$) electrode. The counter electrode (CE) provides a conductive material to complete the electric circuit of the cell, hence all the current measurements taken from the potentiostat are taken between the working and counter electrode. In a half cell setup such as the one shown in figures 10 and 11, the reference electrode is kept much closer to the working electrode compared to the counter electrode to ensure the measured reaction is

the reaction occurring at the working electrode. The reference electrode is kept at a distance of the order of millimetres from the working electrode whereas the counter electrode simply needs to be present in the same electrolyte. Material compatibility with the electrolyte is important to avoid potential poisoning of the electrolyte and/or electrodes when using a half cell setup. For aqueous electrolytes a silver/silver chloride reference electrode and platinum counter electrode is a common setup, but this setup can't be used in an organic electrolyte as this would poison both the platinum and the silver/silver chloride electrodes. For organic electrolytes the counter electrode is often carbon based, like graphite, and the reference electrode is often mercury based.
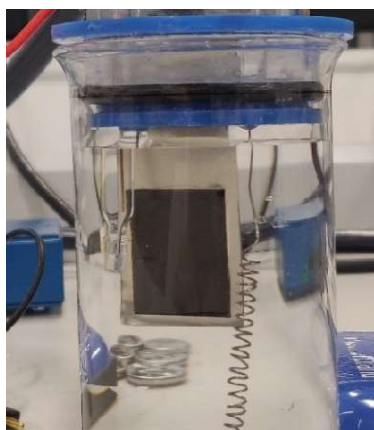
Figure 10. Half-cell setup with a photonic cured carbon WE, a platinum CE and a Ag/AgCl RE.

Nickel is a good substrate material for half-cell testing due to its electrochemical inactivity and low capacitance, but nickel is an expensive and scarce material. Aluminium and stainless steels are common alternatives for testing substrates, in this study 316 stainless steel is used because this was the choice for the carbon conversion substrate. A UV cured epoxy resin was added to the backside of the substrate and slightly onto the coating on the front to minimize interactions caused by the stainless steel with the electrolyte.

Figure 11. Half-cell setups for the photonic cured carbon (left) and the thermal cured carbon (right)

In figure 11 its observed that the photonic cured carbon sample didn't oxidize and poison the electrolyte contrary to the thermal cured carbon working electrode, as the thermal heat-treated stainless-steel substrate oxidises in the aqueous electrolyte. The electrolyte poisoning is due to the reaction of metals ions being released from the stainless steel (109). This showcases the difference between the effects of the two carbonization methods on the stainless-steel substrate, as the thermal treated stainless-steel substrate demonstrates a lower chemical resistance to the aqueous electrolyte. Other similar studies find similar poisoning of stainless steel in the same aqueous sodium sulphate electrolyte but of lower concentration (0.1 M) (109). To verify that it's the stainless-steel reacting with the electrolyte which produces the poisoning, a future experiment should be bare stainless steel, both heat treated and un-heat treated, can be exposed to the electrolyte in the half cell to observe it without carbon coatings. The photonic curing method is a surface treatment and clearly doesn't affect the chemical resistance of the steel. However, taking the stainless-steel substrate to 800°C using the conventional thermal curing heat treatment process clearly changes the chemical resistance properties of the steel as is exposed by the image in figure 11, resulting in the oxidation of the substrate. This poisoning was later avoided by using the same sample mounting method as was required for the photonic cured sample due to its dimensional limitations. The thermal cured glassy sample that was used in collecting the presented data in chapter 4.2.4 is a cut out of area ~2cm^2, which in turn is mounted on a strip of untreated stainless steel of ~20x80mm using a conductive silver paste to make both the mechanical and electrical connection. The stainless steel was then coated in a chemically resistance UV cured resin to minimize the interference of the

stainless-steel substrate on the electrochemical performance results of the two different carbon manufacturing methods.

The half-cell (also known as three electrode cell) setup is used in conjunction with a BioLogic VMP3 potentiostat to perform electrochemical analysis of the two produced carbon films using cyclic voltammetry (CV), electrochemical impedance spectroscopy (EIS) and galvanostatic charge/discharge (GCD). Prior to any to the above listed analyses the open circuit voltage (OCV) of the carbon coatings is found by leaving the system alone with no voltage or current applied to the cell, the three electrodes and the electrolyte are left alone for 5 minutes to reach an equilibrium potential difference.

Cyclic Voltammetry

CV is a method where a voltage is applied to the cell, a voltage step, a scan rate and two boundaries are set and the current induced through the cell is recorded yielding a current versus voltage graph. This method is often repeated with the same sample and voltage boundaries with an array of scan rates to study the effect of the change in scan rate on the behaviour of the current. This data can be manipulated by calculating the active material surface area or weight to obtain a current density. By plotting the obtained current density against the scan rate, the interaction between the electrolyte and the working electrode may be studied (80–82,110,111). By studying the relationship between the current or current density and the scan rate charge/discharge mechanics can be deduced to be surface controlled or diffusion-controlled processes. If the current is proportional to the scan rate its indicative of a surface-controlled process, whereas if the current is proportional to the square root of the scan rate it predicts a material that is dominated by a diffusion-controlled process. Generally, a surface-controlled working electrode is desired for supercapacitor applications whereas a diffusion-controlled process is desirable for battery applications, as the capacitive (surface-controlled) current is representative of double-layer charging and the faradaic (diffusion-controlled) current is representative of ion insertion (112). Double layer charging/discharge is the core mechanism of a supercapacitor and ion insertion is the core mechanism of a battery.

From the CV curve we learn much of the behaviour of the material in question, the stability window of the material is found by expanding the voltage window from the OCV iteratively until a voltage asymptote is found on the positive and negative end of the spectrum. From the shape of the CV curve, it can be deduced whether the studied material behaves like a

capacitor or a resistor, in all cases this is a mixture thereof but it's important to recognize tendencies by comparing to theoretical behaviours. In theory a perfect capacitor should have a CV curve that is a perfect rectangle, whereas a perfect resistor should produce two straight lines that overlap on both the oxidation and reduction steps of the CV curve. If the CV of the material contains reduction and oxidation peaks (redox peaks), studying the voltage at which these chemical reactions occur at different scan rates allows you to observe whether the interactions at these points are reversible or irreversible. If these redox peaks shift with scan rate the chemical reactions made permanent changes to the working electrode and are therefore irreversible, if the redox remain in the same location with changing scan rates the chemical reactions are reversible (113).

Galvanostatic Charge/Discharge

GCD is a method where a specific constant current is applied to charge and discharge the system to study the integral capacitance and the equivalent series resistance of an electrode material. Boundary conditions are setup in the form of a maximum and minimum voltage to which the charging and discharging takes place. In this GCD method the voltage is measured as a function of time for each set applied current. When the applied current changes direction upon reaching the pre-set voltage boundary, either the maximum or minimum, the voltage changes instantaneously as a result of the capacitance of the working electrode material, the change in voltage is known as the voltage drop. This voltage drop may be used to calculate the equivalent series resistance of the working electrode, as the measured voltage is a combination of the voltage across the equivalent series resistance and the voltage across the double layer capacitance. If the voltage drop is plotted as a function of the current density of the material the resultant gradient should theoretically be linear and be equal to factor 2 of the equivalent series resistance. The differential and integral capacitances of the material may be calculated from the acquired GCD data. The differential capacitance is the instantaneous capacitance at a specific moment in time and may be calculated using the constant applied current and the instantaneous differential of voltage with respect to time using the equation

$$C_{differential} = \frac{dQ}{dV} = \frac{1}{dV} I dt = \frac{I}{dV/dt}$$

Where dV/dt is the gradient of the recorded voltage as a function of time GCD plot. The same equation may be used for the integral capacitance, the average capacitance, of the working electrode material, only the voltage and time difference are taken over the entire

charge/discharge cycle rather than a differential at a specific point in time. Thus for the integral capacitance we find

$$C_{integral} = \frac{\Delta Q}{\Delta V} = \frac{I\Delta t}{\Delta V}$$

The integral capacitance may be calculated for both the charge and discharge curves, the ratio of the charge and discharge capacitance may then be used to calculate the Coulombic efficiency of the material as a function of current. Coulombic efficiency, also known as Faradaic efficiency, is defined as the ratio of the discharge capacitance and the charge capacitance of a material. Coulombic efficiency has units' percentage from the following equation

$$\eta = \frac{C_{discharge}}{C_{charg}} \times 100$$

Electrochemical Impedance Spectroscopy

EIS is a method that utilized alternating current instead of direct current to study the working electrode sample. EIS collects data of multiple variables making it a versatile tool for a multitude of applications. For the electrochemical analysis of the carbon coatings in this thesis, the Nyquist plot is used to study the complex impedance values and behaviour over a range of AC frequencies. This data allows one to interpret and fit models to the mechanics of the interactions between the working electrode and the electrolyte. Every working electrode interacting with an electrolyte can be modelled using a theoretical electric circuit. These theoretical equivalent circuits can be broken down into 3 fundamental components: a resistor, an inductor and a capacitor. A specific type of equivalent circuit is the Randles circuit, which is often used to describe a coating on a substrate in an electrolyte. This Randles circuit consists of a parallel plate capacitor with the electrolyte as an electrode, the coating as a dielectric and the metal subgstrate as another electrode (114). The equivalent circuit for carbon coating on a stainless steel substrate as the working electrode can be broken down into 4 components: the ohmic internal resistance (R_{in}), the charge transfer resistance (R_{ct}), the double layer capacitance (C_{dl}) and the Warburg impedance (W). The internal resistance ohmic resistance in practically all cases is representative of the electrolyte resistance of the half-cell setup. The charge transfer resistance is classically dominated by the imposed resistance of redox processes occurring at the working electrode, but as the studied carbon coatings didn't undergo any redox processes in the studied voltage window, this value is dominated by the resistance of

the stainless-steel substrate. At the electrode and electrolyte interface there exists an electrical double layer consisting of positively or negatively charged ions depending on the charge of the electrode. This electrical double layer behaves like a capacitor, there is no electron transfer between the electrode and the ions in the electrical double layer. As the electrode electrolyte interface also contains some sort of resistance as well as some capacitance, the Randles circuit models commonly models this interface as a capacitor and a resistor in parallel. The Warburg impedance describes the mass transport of a system and is a factor that is observed when the mass transport/redox species become the limiting factor of charge transfer in the system (115). In the carbon layers studied this most likely happened in the form of oxygen corroding the surface of the stainless steel as the carbon layer deteriorated. The Warburg impedance becomes the dominating factor in the Nyquist plot at low frequencies due to change of speed of diffusion. At lower frequencies the reactants will travel larger distances before the direction of flow changes, at high frequencies the Warburg impedance becomes negligible (115).
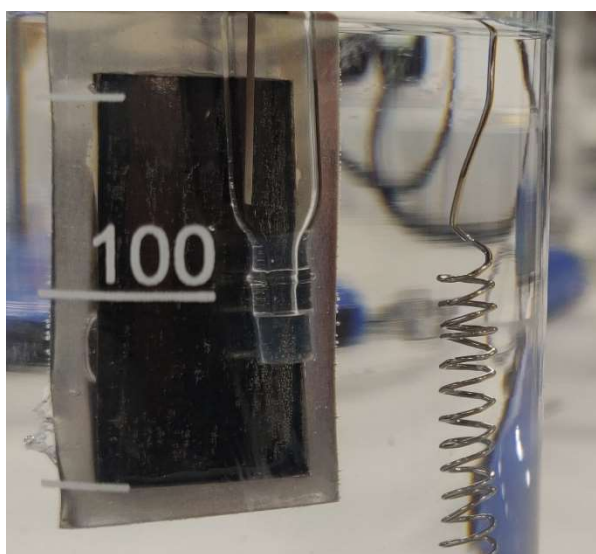
Figure 12. Photonic cured carbon sample mounted on stainless steel foil in a half-cell testing jig. Reference electrode = silver/silver choride, counter electrode = platinum coil.

3.4.9 Electrical Performance Testing

Testing the contact resistance, line conductivity and sheet resistance of different geometries of screen-printed glassy carbon structures the Keithley 2100 multimeter was employed for the data reading. The multimeter was set to display an average value of the last 100 readings. For the contact resistance and line conductivity experiments a two-point probe setup was used as shown in the image in figure 13. The two probes were held in

place using a standard set of laboratory stands and clamps to remove any movement in the probes during the data recording. Printed glassy carbon lines of length 27.3mm and varying widths between 0.3 and 1.0mm are studied for contact resistance and line conductivity on non-conductive alumina substrate.
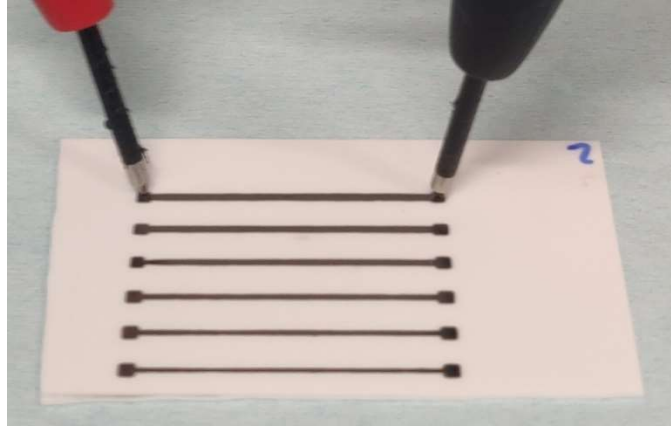
Figure 13. Two-point probe setup close-up from a line conductivity measurement, two electrodes in contact with the extremities of the glassy carbon printed line.

The sheet resistance measurements were taken using a 4-point probe connected to the Keithley 2100 multimeter which has a software option to interpret the 4-point probe style resistance data. A four-point probe works by applying a small current between the two outer electrodes, while the middle two electrodes measure the potential difference on the surface of the studied material. Depending on the geometry of the surface of the studied material an empirically derived correction factor must be applied to the recorded resistance values. The geometry of the printed glassy carbon squares is of measurements 40x40mm with a probe spacing of 1mm as demonstrated in figure 14, which corresponds to the correction factor of 4.512 to be multiplied by the recorded raw resistance data values (83). As shown in figure 14, the 4-point probe is held in place with a stand and clamp to remove any movement from the probes during measurements. 9 measurements were taken per sample to produce a reliable average value with meaningful standard deviation.
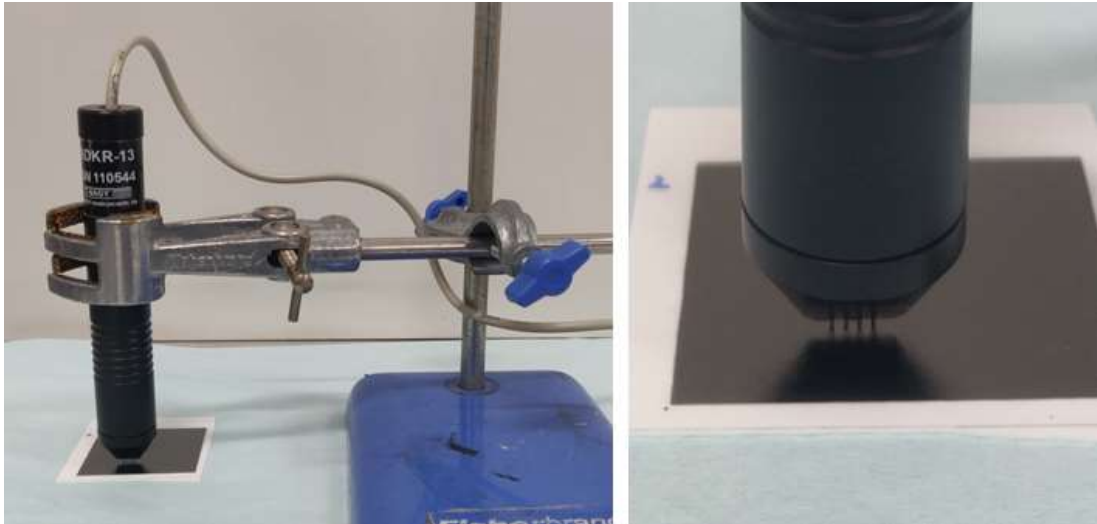
Figure 14. 4-point probe setup from a sheet resistance measurement. Image of how the probe is kept in place on the LHS and a detailed image on the RHS of how the 4 electrodes are in contact with the glassy carbon surface.

To test the viability of glassy carbon as a temperature sensor essentially the same two-point probe setup as previously shown in figure 13 is used, but the probes are replaced with crocodile clips which were soldered to wiring that was manually covered in heat resistant isolating material, as shown in figure 15. The crocodile-clips maintained contact with the printed glassy carbon lines during the recording of resistance values for an array of different temperatures ranging from room temperature to 140°C at intervals of 10°C. As a baseline comparison, resistance measurements were taken of the probe wires connected to each other by marrying the crocodile clips.
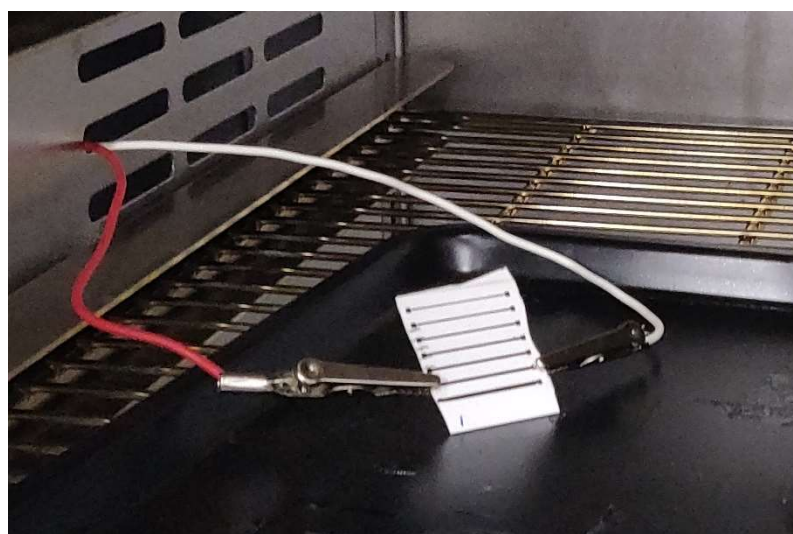
Figure 15. Crocodile-clips soldered to wire with heat resistance isolation sleeve attached to printed glassy carbon lines inside a convection oven.

Electrochemical impedance spectroscopy (EIS) and the 4-point probe setup are used to test the viability of glassy carbon as a salinity sensor by screen printing glassy carbon interdigitated structures. The 4-point probe is used to measure the sheet resistance of a sample of 40x40mm screen printed glassy carbon on alumina substrate that was kept in 5% saline solution for 70 days, measurements were taken at day 0, 1, 2, 3, 8 and 70. There is a large gap in measurements between day 8 and 70 because the 4-point probe had stopped working and no replacement was available at this time.

EIS was performed on screen printed glassy carbon interdigitated structure of 4 different sizes, these sizes are defined in section 6.5.1. These size measurements are used to calculate the cell constant of each size of interdigitated structure, which is an empirical parameter used to determine the relationship between solution conductivity and cell conductance via the equation

$$\sigma = K \times G$$

Where σ is solution conductivity, K is the cell constant, and G is the cell conductance.

The EIS measurements were taken at 5 different voltages to provide average values with standard deviations. These voltages were determined by a preliminary CV scan which showed a linear range of -0.5V to 0.5V, thus voltages in this window with a 0.25V step size were used to take EIS measurements. This sequence of testing was done for saline solutions of salt concentration 0.5% to 5% in distilled water. The salt used for the saline solutions is Saxa fine salt which consists of NaCl with sodium hexacyonoferrate(II) additive. For testing the viability of the glassy carbon interdigitated structures as salinity sensors, the interest lies at the high frequency end of the spectrum and the resistance's relationship with the salt solution concentration. Therefore, EIS is used to study the resistance as a function of frequency and as a function of salt solution concentration.
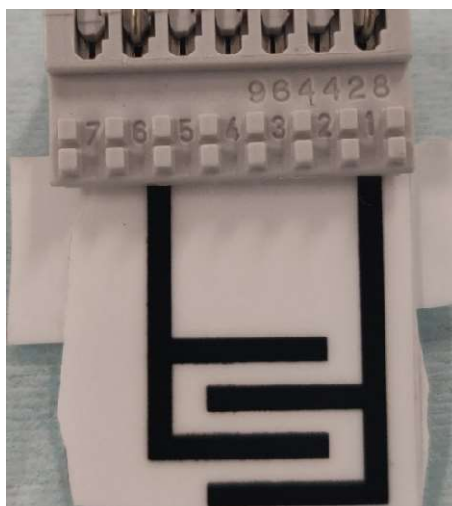
Figure 16. Screen printed glassy carbon interdigitated structure secured in an electrode connector to make electrical contact with the glassy carbon and provide a connection to the working, counter and reference electrode ports on the Biologic potentiostat.

3.5 Chapter Closure

This chapter covered the materials, apparatus and methods used in the research of the following three chapters. Chapter 4 explores photonic curing as a novel rapid carbonization method to produce glassy carbon, Chapter 5 explores the application of glassy carbon produced using both thermal carbonization and photonic curing as electrode active materials and Chapter 6 explores the application viability of glassy carbon in printed electronics and sensors.

Chapter 4: Glassy Carbon Thin Film Development

4.1 Introduction

This chapter compares the manufacture of glassy carbon thin films using two carbonization methods: the conventional thermal carbonization and a novel approach based on photonic curing. The chapter describes manufacturing process followed by material characterisation of the carbon thin films. The process of producing these carbon films is discussed from start to finish, the material characterisation compares the chemistry of the material produced using the two methods as well as comparing it to literature.

4.2: Precursor Resin Deposition and Characterisation

Before any carbonisation process, thin film layers of phenol formaldehyde resin precursor had to be deposited over the selected stainless-steel substrate. Preliminary assessment of the rheology of the resin was performed to help defining coating selection. Bar-coating was selected for its suitability and simplicity. Details of bar-coating process with measurements of resulting deposited layer thickness are described below.

4.2.1: Rheology of Glassy Carbon Precursor

To understand the behaviour of the chosen phenol formaldehyde resin precursor before printing/coating, the rheology of the resin, as supplied by Bitrez Ltd, is studied using a Malvern Kinexus Pro+ rheometer. My colleague Alaa Alaizoki aided in the data of the following rheology measurements. From figure 17 it's observed that the elastic and viscous moduli and the phase angle are independent of the shear stress applied to the liquid, suggesting that the precursor behaves like a Newtonian fluid at room temperature, which was measured to be 20°C.
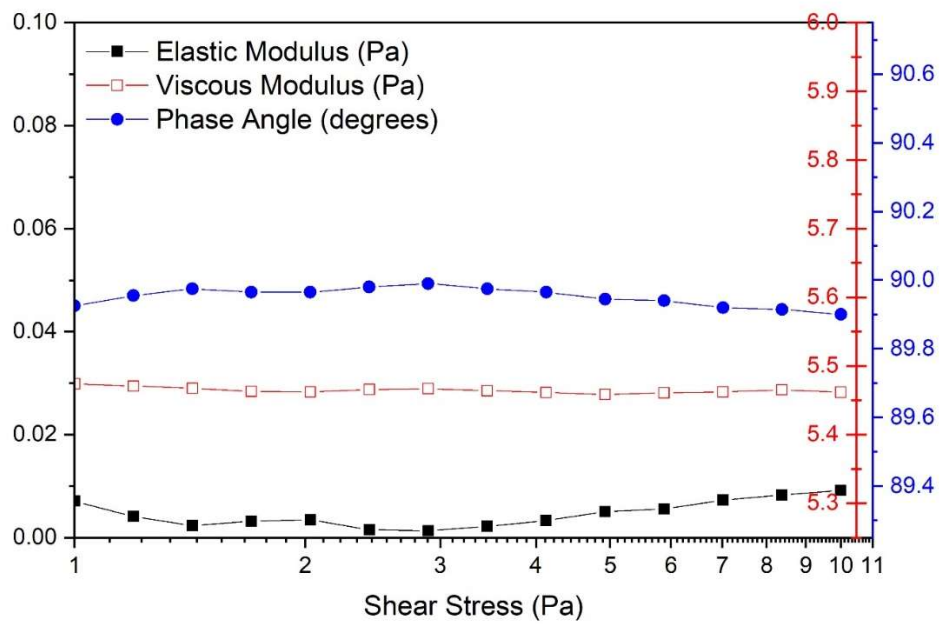
Figure 17. Elastic modulus, viscous modulus and phase angle plotted against the imposed shear stress during the rheology measurements

From the data in figure 17 and 18, it's found that the average viscosity is 0.830 ± 0.008 Pa*s and the average phase angle is 89.95 ± 0.11 degrees.
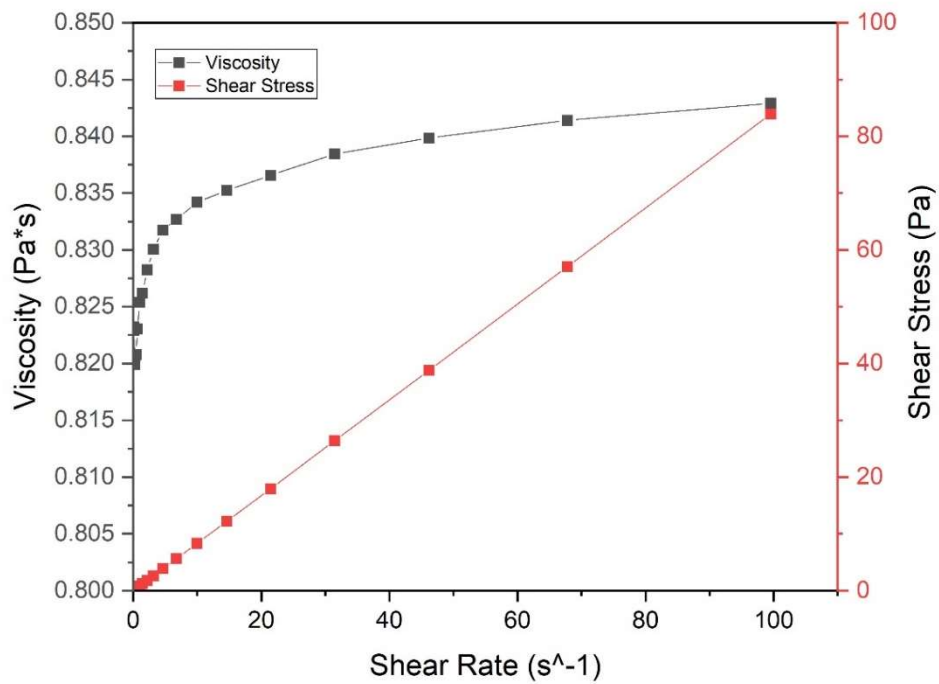
Figure 18. Viscosity and Shear Stress as a function of shear rate of the phenol formaldehyde resin precursor.

4.2.2: Bar Coating of Glassy Carbon Precursor

This section discusses the bar coating process and parameters adopted for this work for the coating a phenol formaldehyde resin, precursor to glassy carbon.

Bar coating was used to deposit a thin film in the order of micrometres of the phenol formaldehyde precursor onto the selected substrate (316 stainless steel). Bar coating was performed on a semi-automatic K-Control coater as seen in figure 19. As a note, the phenol formaldehyde precursor supplied by Bitrez contains solvents that evaporate quickly in air (butan-1-ol, m-cresol and xylene) and is therefore only of printable viscosity in air for a few minutes.
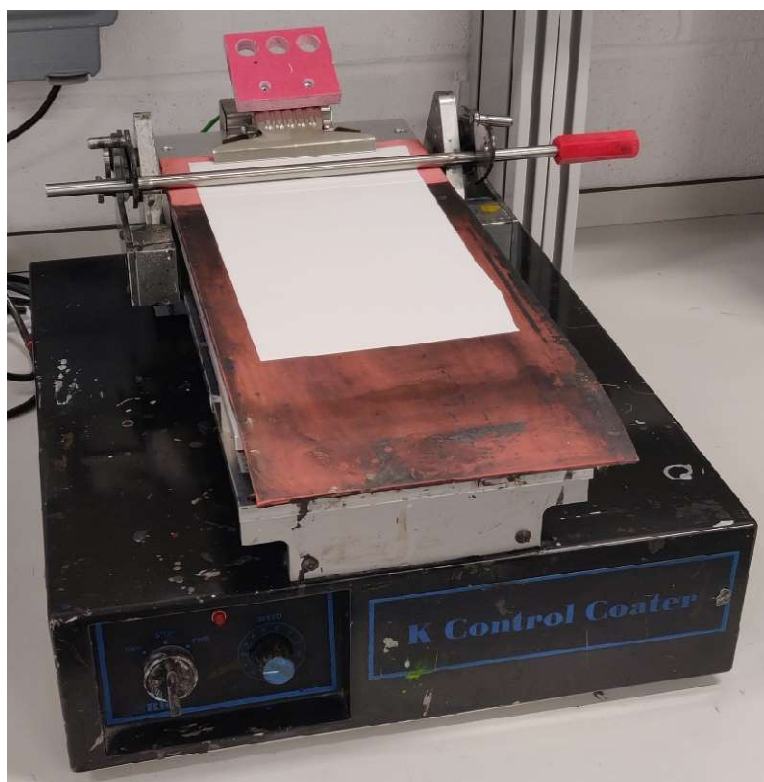
Figure 19. K Control Coater setup with protective PET substrate on the print bed to stop contamination of the equipment with phenol formaldehyde precursor resin.

In a preliminary study, bar coating showed good repeatability in deposition layer thickness due to the simple procedure with minimal changeable parameters. The preliminary bar coating study for deposition layer quality revealed the speed setting had negligible impact on the print quality of this particular phenol formaldehyde resin. A low print speed was chosen to maximize quality and layer thickness repeatability at the nominal 2m/min setting. This setting was checked to measure the actual speed by recording a video of the

print speed and measuring the distance travelled and time taken, using the video the real print speed value is calculated to be circa 1.1m/min when the dial is on nominal 2m/min.

A variety of theoretical wet depositions were explored, from 4 to 40µm using close-wound bars of which the details are displayed in figure 20. Bar sizes 0, 1 and 2 provided the most stable layer thicknesses depending on the carbonization process. Size 0 was used for the photonic curing method whereas sizes 1 and 2 were used in the conventional thermal carbonization method.

BAR No.	COLOUR CODE	WIRE DIAMETER		WET FILM DEPOSIT	
		INCH	MM	INCH	µM
0	White	0.002	0.05	0.00015	4
1	Yellow	0.003	0.08	0.00025	6
2	Red	0.006	0.15	0.0005	12
3	Green	0.012	0.30	0.0010	24
4	Black	0.020	0.51	0.0015	40

Figure 20. List of close wound bar coating K-bars that were tested using the PrintCoat Instruments K Control Coater in the preliminary study to determine print speed and deposition layer thickness.

The substrate on which precursor was bar coated was a 100µm thick 316 stainless steel. Prior to bar coating the precursor, the substrate was thoroughly cleaned with isopropanol. The phenol formaldehyde is then deposited when the IPA has evaporated off the substrate surface to minimize the chance of contamination before coating. After coating, the phenol formaldehyde must be thermoset cured at 220°C for 30 minutes as per the data sheet provided by the supplier, Bitrez Ltd. This results in a set, amber coloured, phenol formaldehyde layer of approximately 50% reduced thickness from the initial theoretical wet deposition layer thickness.

Figure 21. Thickness measuring instruments used to check layer thickness of phenol formaldehyde on stainless steel substrate. Digital micrometer thickness gauge (top) and magnetic probe thickness gauge (bottom).

The carbon coating layer thickness was measured using a digital micrometer thickness gauge and a magnetic probe thickness gauge as shown in figure 21. The magnetic probe thickness gauge has the higher precision at 0.1 microns compared to the digital micrometer gauge which has precision to 1 micron. Hence the magnetic probe was used for the following thickness measurements in table 1. For the characterisation comparison between thermal carbonized glassy carbon and photonic cured glassy carbon materials, 4 phenol formaldehyde resin large area samples were produced on the 100µm stainless steel substrate of area ~ 15x25cm². The sample coating thickness was measured with 10

repetitions for reliable average and standard deviation values, the average coating thicknesses of 4µm theoretical wet deposition thickness cured phenol formaldehyde coatings on stainless steel is displayed in table 1. This magnetic probe recorded the thickness of the substrate with the coating together, hence the thickness of the stainless-steel substrate is measured without any coating at 102.4 ± 0.3 µm which is subtracted from the total thickness to find the layer thickness. From the data in table 1, its observed that ~22.5 – 32.5% of the theoretical layer thickness is retained as cured resin thickness. The precision of the instrument is a limiting factor, but these thickness measurements yield an indication of dried resin layer thickness of the chosen coating bar size. Large samples of area ~15x25cm^2 were then cut into 24 smaller samples of ~3x3cm^2 for carbonisation study.

Table 1: Average dried phenol formaldehyde resin precursor layer on 100µm stainless steel substrate coated with theoretical wet deposition thickness of 4µm for 4 different bar coated samples of area ~15x25cm^2. The sample standard deviations are measured using an average value over 10 measurements.

N = 10	Sample 1	Sample 2	Sample 3	Sample 4
Film thickness [µm]	0.9 ± 0.3	0.8 ± 0.3	1.0 ± 0.3	1.3 ± 0.4

4.3 Thermal Carbonization to Glassy Carbon

This section is dedicated to the identification of the thermal carbonisation process parameters to produce glass carbon from a phenol formaldehyde precursor resin and the challenges encountered.

To produce a glassy carbon thin film on a stainless-steel substrate, the literature was closely studied to identify thermal carbonization parameters, literature suggests glassy carbon is produced between 600°C and 2000°C in inert atmosphere (nitrogen or argon) at ramp rates <5°C/min (24–27,30,47). Using 25µm 316 stainless steel foil substrate, the available heat treatment temperature range is reduced to between 600°C and 900°C, because 316 stainless steel keeps its structural integrity up to temperatures of ~900°C (84,85).

A heat treatment temperature of 700°C with a dwell time of 2 hours was chosen as a starting point for the carbonization of phenol formaldehyde to produce glassy carbon in the

Carbolite tube furnace while keeping a nitrogen induced inert atmosphere as discussed in chapter 3. Heat treatment temperatures of 800°C and 900°C were also explored, 900°C caused severe warping of the stainless-steel substrate of both 25μm and 100μm thickness. A set point temperature of 800°C caused warping on the 25μm stainless steel substrate but did not structurally affect the 100μm substrate, thus 800°C was chosen as the final set point heat treatment temperature to carbonize glassy carbon on stainless steel substrates. The dwell time throughout is kept at 2 hours.

Figure 22. Warped 25μm stainless steel substrate with patches of glassy carbon coating post heat treatment at 800°C in the tube furnace.

A ramp rate of 5°C/min and a nitrogen gas flow rate of 1L/min are recurring values in the literature mentioned above, thus these are taken as starting parameters. The two main challenges searching for optimal carbonization parameters using a tube furnace were the delamination of the glassy carbon layer off the stainless steel substrate and the warping of the stainless steel substrate, both of which are demonstrated in figures 22 and 23 respectively.

The initial ramp rate was set at 5°C/min, two other values are explored to minimize layer delamination and warping of the substrate. 1°C/min and 2°C/min experience negligible difference in results between each other but both experience less layer delamination and warping of the substrate through the heat treatment cycle. 2°C/min is chosen as the final ramp rate to same time, energy and nitrogen gas spent during heat treatment.

The initial batches of producing glassy carbon layers on stainless steel foil were coated on 25μm stainless steel, of which all carbonizations resulted in warping of the substrate causing the carbon layer to delaminate. A change to 100μm 316 stainless steel foil from the same manufacturer (Advent Materials, UK) resulted in reduced warping of the substrate.

Figure 23. Image of complete surface fracturing resulting in delaminated glassy carbon off stainless steel substrate in ceramic tube furnace boat post heat treatment.

A variety of nitrogen flow rates were trialed to study the effect on the adherence of the glassy carbon to the stainless-steel substrate, from 0.33 to 2L/min. These changes were found to have no effect on the delamination or the warping issues experienced using this method of producing glassy carbon coatings on stainless steel. 1L/min was kept as the final parameter for the nitrogen flow rate because this was the minimum flow rate that consistently pushed exhaust gases through the gas outlet of the tube furnace, creating an inert atmosphere during carbonization.

These discussed parameters were applied to phenol formaldehyde coatings with a range of different precursor layer thicknesses between 4μm and 40μm theoretical wet deposition thickness. Initial carbonizations of this range of precursor thicknesses on 25μm stainless steel substrate resulted in delamination of the carbonized precursor and warping of the substrate as shown in figures 22 and 23. After the change to 100μm stainless steel substrate, the warping at all coating thicknesses tested was reduced and the resultant glassy carbon layers are stable from theoretical wet deposition layers 4μm to 12μm, 24μm and 40μm theoretical wet deposition precursor layers also fractured on the thicker substrate.
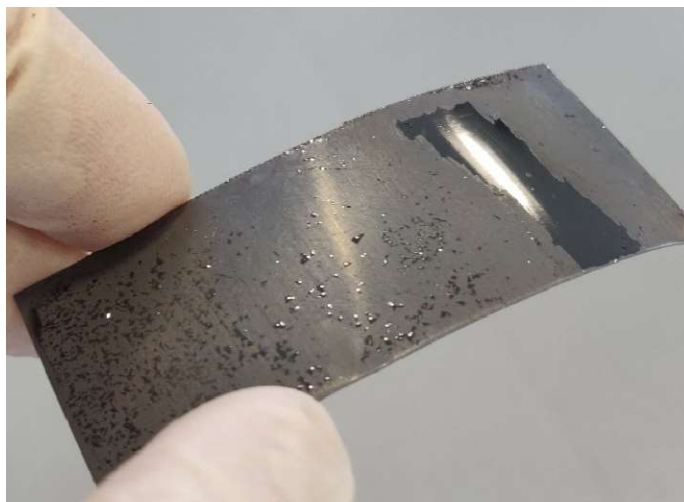
Figure 24. Patch of glassy carbon remaining on 100µm stainless steel, no warping but still significant delamination of the carbon layer.

Although the thin theoretical wet precursor layers (4, 6, 12µm) show improved stability on the thicker 100µm stainless steel substrate, some fracturing and delamination remains, as seen in figure 24. To improve adherence between the carbon thin film and the substrate the surface roughness is increased by using sandpaper of varying grit sizes. Grit sizes 120, 400, 600 and 1000 were tested in a preliminary study to determine suitability of use. Grit sizes 120, 400 and 600 were observed to be increase the surface roughness too much, causing incomplete phenol formaldehyde precursor coating coverage. The 1000 grit resulted in good adherence between the carbon coating and the substrate as seen in figure 25, without any warping or delamination. The surface roughness was not measured but the stainless steel surface was lightly sanded until the surface was visually homogeneous. The substrates were cleaned with acetone followed by IPA to avoid any contamination into the coating material.
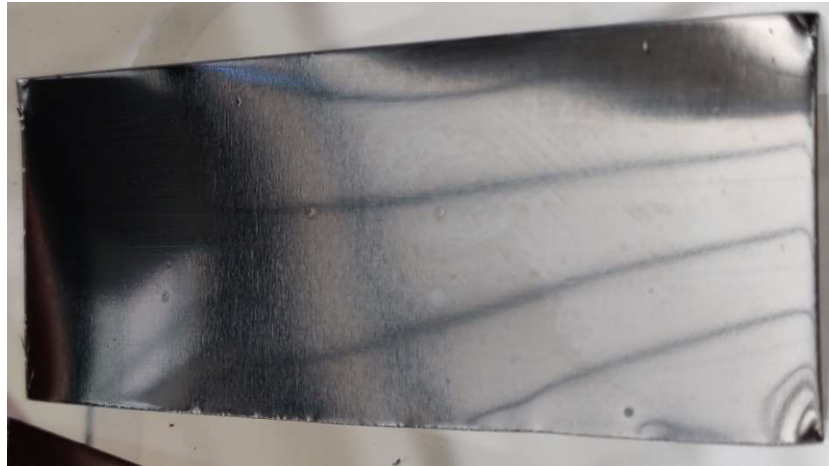
Figure 25. Representative sample of thermal carbonized glassy carbon thin film on 100µm stainless steel substrate (ca 8 x 2 cm)

All samples for characterization will be made using the parameters shown in the flow chart in figure 26. Precursor phenol formaldehyde is bar coating with wet layer deposition thickness 4, 6 or 12µm on 316 stainless steel substrates with manipulated surface roughness using 1000 grit sandpaper. Heat treatment with a set point of 800°C, a ramp rate of 2°C/min, a dwell time of 2 hours and a nitrogen flow rate of 1L/min through the tube furnace to keep the atmosphere inert during heat treatment.
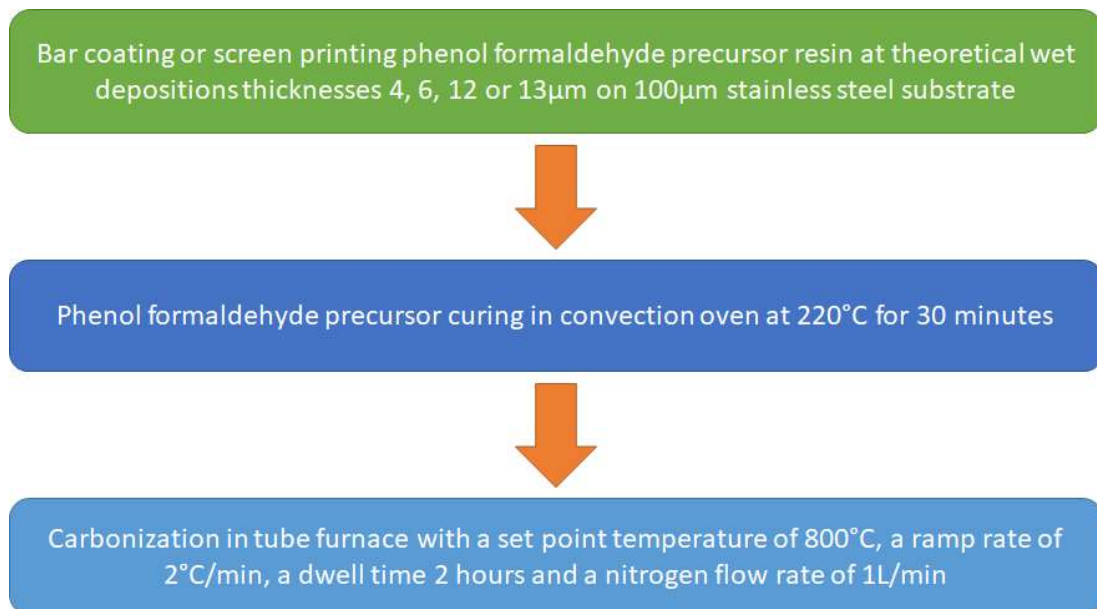
Figure 26. Flow chart of the complete thermal carbonization method from phenol formaldehyde resin precursor to glassy carbon on 100µm stainless steel substrate.

4.4 Photonic Curing as a New Carbonization method

As part of my doctorate research, the application of photonic curing is explored as an alternative method of carbonising the precursor phenol formaldehyde resin into glassy carbon. This section discusses the parameters, results and challenges encountered during the process of producing a carbon thin film layer using a Novacentrix Pulseforge 1200 photonic curing system.

A range of theoretical wet deposition thicknesses were trialled in a preliminary experiment to observe the behaviour of the phenol formaldehyde precursor resin during photonic curing. These preliminary tests were done using 1 – 18 pulses with lamp voltages 350 – 450V at 5 – 20ms exposure time. The resultant energy density output is calculated by the Novacentrix software that controls and manages the photonic curing equipment. Theoretical wet deposition of 4, 6 and 12µm were investigated because these proved most stable in the conventional thermal carbonization method studied. Precursor coatings of 6µm and 12µm theoretical wet deposition experienced incomplete carbonization and fractured coating surface as seen in figure 27. Precursor coatings of 4µm displayed stable surfaces at 20 pulses using 450V lamp voltage at 20ms exposure time as seen in figure 28. Thus from the preliminary study of precursor layer thickness the chosen phenol formaldehyde theoretical wet deposition thickness is 4µm for future photonic curing carbonization.

A Novacentrix Pulseforge 1200 photonic curing system with the settings shown in table 2 below, yields a projected energy output of 26.96 J/cm^2 to the surface of the phenol formaldehyde resin coated on stainless steel. The projected energy output displayed in table 2 is calculated by the Novacentrix software that controls and manages the photonic curing equipment. Using the parameters from table 2, a change in pulse number is studied to discover the amount of energy required to carbonize the precursor using high intensity light. The lamp voltage and lamp limit were the maximum achievable energy output parameters of the specific lamp installed on the Pulseforge 1200 that was used to produce glassy carbon thin films. The sample chamber, a steel container with a quartz window as shown in figure 7 (section 3.3.3), was continuously flushed with nitrogen gas before, during and after exposure to the pulsed light.
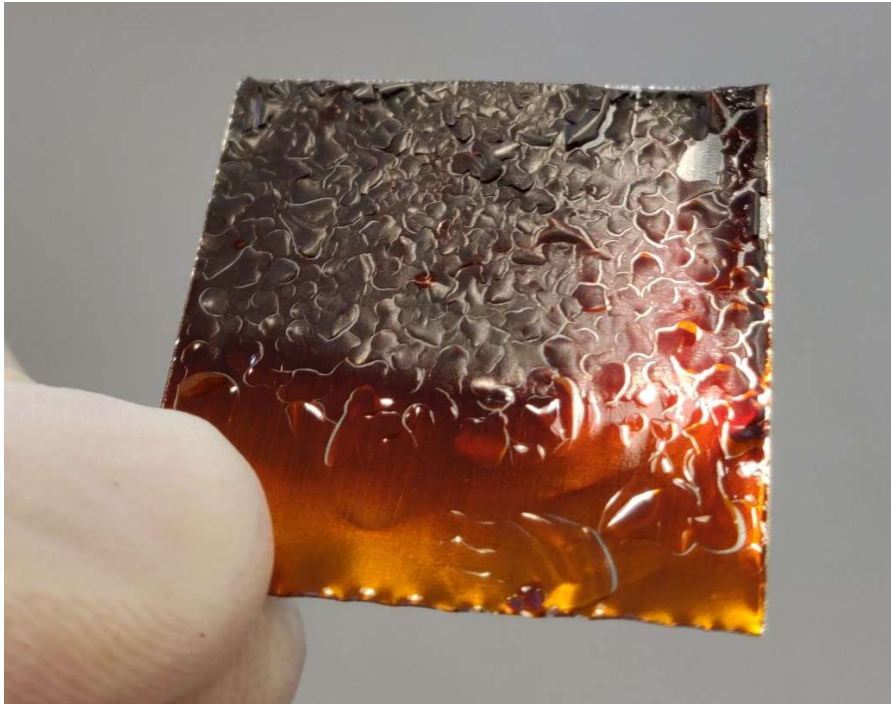
Figure 27. Photonic cured phenol formaldehyde precursor of 12 μm theoretical wet deposition thickness on 100 μm stainless steel substrate of area 2x2cm. Partial carbonization of the precursor with surface fractures resulting in delamination of the coating off the substrate.

Table 2: Final experimental parameters of the photonic curing process to carbonize phenol formaldehyde resin into glassy carbon using the Novacentrix Pulseforge 1200.

Parameter	Value and Unit
Lamp voltage	450V
Exposure time	20ms
Frequency	0.3Hz
Lamp limit	12.8%
Lamp Position	75mm
Base height	31mm
Projected energy density output	26.96 J/cm^2

The phenol formaldehyde precursor coatings were converted at 1, 2, 3, 4, 5, 6, 7, 8, 9, 10, 15 and 20 pulses. Six samples were produced per pulse number for repeatability, standard deviation and the ability use samples for characterisation including destructive methods. Photonic curing as a method to carbonize the phenol formaldehyde precursor was observed to be successful from 3 pulses onwards using the previously discussed parameters.

Figure 28. Photonic cured carbon thin film on stainless steel, carbonized on the NovaCentrix 1200 Pulseforge using 20 light pulses of 27 J/cm^2 energy density output.

The Novacentrix Pulseforge 1200 malfunctioned soon after these samples were produced, preventing further study of using photonic curing as a method to produce glassy carbon thin films.

4.5: Characterisation of Thermal and Photonic Cured Carbon

This subchapter is dedicated to the characterisation and performance comparison between glassy carbon thin films produced using the same phenol formaldehyde precursor with alternate carbonization methods in conventional thermal carbonization and photonic curing. The characterisation results of these two methods are compared to each other as well as to literature to verify the quality of both carbonization methods.

4.5.1 Gas Chromatography - Mass Spectrometry of Carbonization

Gas chromatography – mass spectrometry (GC-MS) is utilized to study the chemical off gases from the phenol formaldehyde precursor to glassy carbon and to study the mass loss of the precursor as it goes through the carbonization process. For a direct comparison to

the thermal carbonization process discussed above, the mass spectrometer heating parameters were matched wherever possible. GC-MS tests were performed by Dr. Geraint Sullivan in the candidate's presence and support.

Using a PerkinElmer Clarus 600T mass spectrometer, a small crucible is filled with the precursor phenol formaldehyde resin already thermoset at 220°C, the precursor is then carbonized in an inert atmosphere by way of nitrogen gas flushing at a ramp rate of 2°C/min up to a set point of 800°C with a dwell time of 2 hours. The only parameter that couldn't be exactly matched was the nitrogen flow rate because the heating chamber and the amount of precursor that is carbonized is significantly different from the manufacture of glassy carbon thin films in a tube furnace.
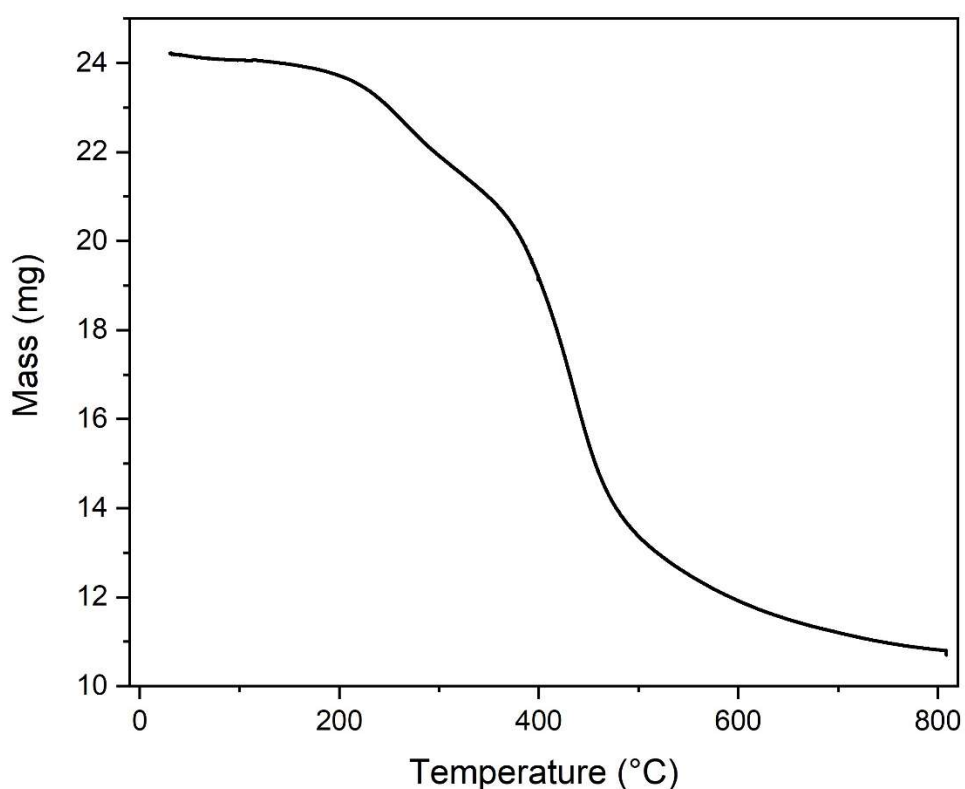
Figure 29. Recorded mass of the precursor resin as it transitions to glassy carbon through thermal carbonization.

The initial mass of phenol formaldehyde (dry) is measured by the mass spectrometer at 24.2mg and the final mass of the glassy carbon after the carbonization process is measured at 10.7mg, thus the precursor to glassy carbon thermal carbonization process experiences a mass loss of 55.9%. From figure 29, it's observed that the majority of the mass loss occurs in the temperature window of 300 to 500°C. From room temperature to 300°C the

precursor experiences 17.1% of its total mass loss, from 300 to 500°C the precursor starts to carbonize and experiences 63.2% of its total mass loss, and finally from 500 to 800°C the now predominantly carbon material experiences the remaining 19.7% of its total mass loss. From literature (24,61) it is understood that carbonization starts in the temperature range 500-600 °C. The mass spectrometer identifies the chemical off gases throughout the carbonization process, in table 3 below the chemicals are listed in the previously discussed temperature windows with a relative response rate of >10% in decreasing quantities. The chemical 3,4, dimethyl phenol occurs in both temperature windows as it takes a longer time at elevated temperatures to off-gas from the precursor.

Table 3: Chemical off gases from phenol formaldehyde through carbonization process from room temperature to 800°C in order of relative quantity in each temperature window.

20 - 300°C Temperature Window Chemical	300 - 500°C Temperature Window Chemical	500 - 800°C Temperature Window Chemical
2-Butene	1-Butene	2-methyl phenol
	2,4,6 Trimethyl Phenol	M-cresol
	3,4 Dimethyl Phenol	1,2,3 trimethyl benzene
	Formic acid butyl ester	3,4, dimethyl phenol
	3,4,5 Trimethyl Phenol	3,5 dimethyl phenol
	2,3 Dimethyl Phenol	O-cresol
	4-Ethyl-3,4-dimethyl-2,5-cyclohexadien-1-one	Phenol
		O-cymene

4.5.1: Coating Topography of Carbonised Coatings

Following the carbonisation process, the photonic and thermal cured carbon coatings were both well adhered to the stainless-steel substrate under manual handling. Both methods yielded uniform, smooth and durable carbon coatings. The coatings did not readily delaminate when exposed to bending of the coated foil, see figure 30. The glassy carbon coatings on stainless steel were able to be manipulated in dimensions after carbonization

with scissors and/or a die-cutter for specific geometries for potential coin- or pouch-cell usage without damaging the coatings in any way.
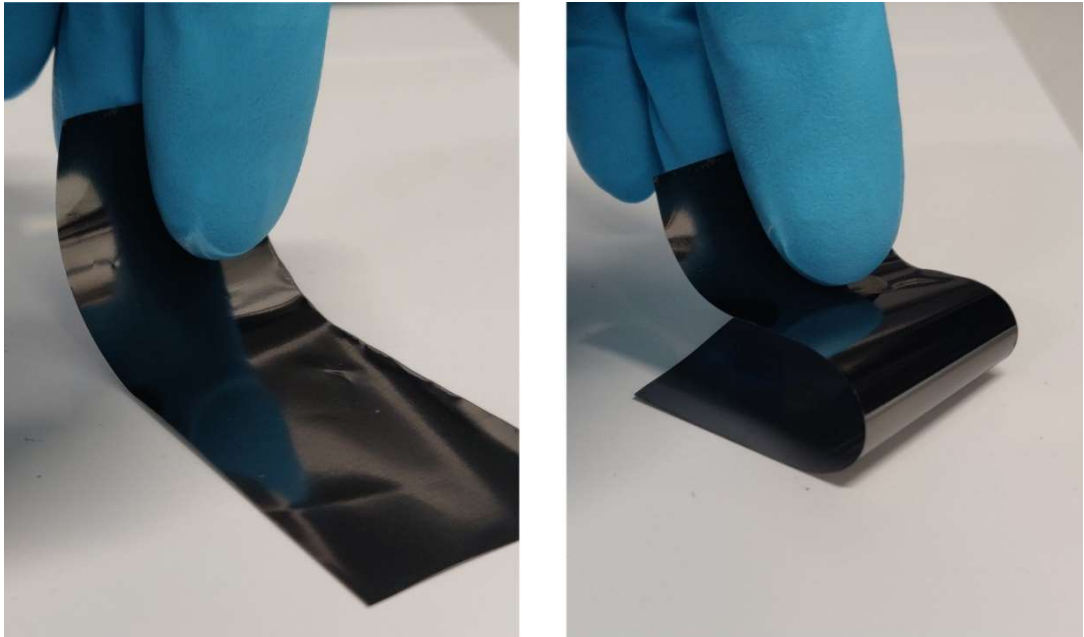
Figure 30. Carbon coating on stainless steel substrate flexed in multiple directions to test adhesion

SEM images of the photonic cured carbon and thermal cured carbon samples are presented in figure 31. To provide a contrast for SEM imaging, between the coating and the underlying steel substrate, part of the coating was removed. The images show the photonic cured samples after different exposure times (10, 15 and 20 pulses) as well as the thermal cured material at a magnification of 30,000 times. Regardless of the preparation method, the carbon coatings presented a highly smooth surface and were consistent without evidence of any defects such as pinholes, delamination or scratches based on the surface area surrounding the human induced imperfections shown in figure 31. Thermal and photonic derived surfaces presented similar visually glossy appearances, showing no discernible difference between the two carbonisation methods. For future characterisation a range of magnifications could be explored to potentially observe some more macroscopic sized imperfections in the coatings.
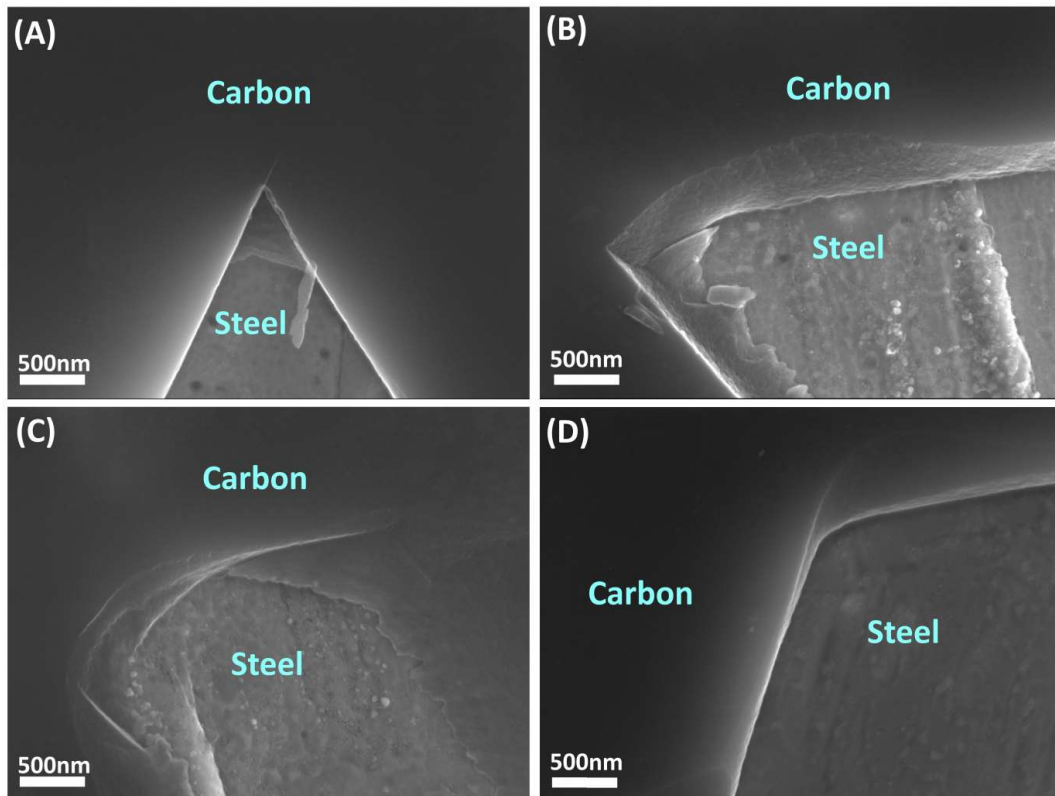
Figure 31. Scanning electron microscopy images of photonic cured carbon coatings at different amounts of pulses and thermal cured carbon with exposed stainless-steel substrate at 30,000x magnification. A: 10 pulses, B: 15 pulses, C: 20 pulses, D: thermal cured carbon.

White light interferometry measurements show a full three-dimensional surface profile over the coated surfaces. A total of 5 measurements are taken for each sample with average surface roughness measurements (Sa) calculated over the measured surface, in contrast to Ra which is measured across a single plane (116), the errors are calculated using standard deviation. These average surface roughness measurements are compared in figure 32. The untreated phenol formaldehyde resin precursor had an average surface roughness, Sa, of 470nm. Upon treatment, the roughness of the surface was reduced, and the Sa values of both the photonic cured carbon coatings and the thermal cured carbon coating were similar and in the range of ~110-140nm. This data demonstrates that both thermal and photonic carbonization methods resulted in similar carbon surface topographies.
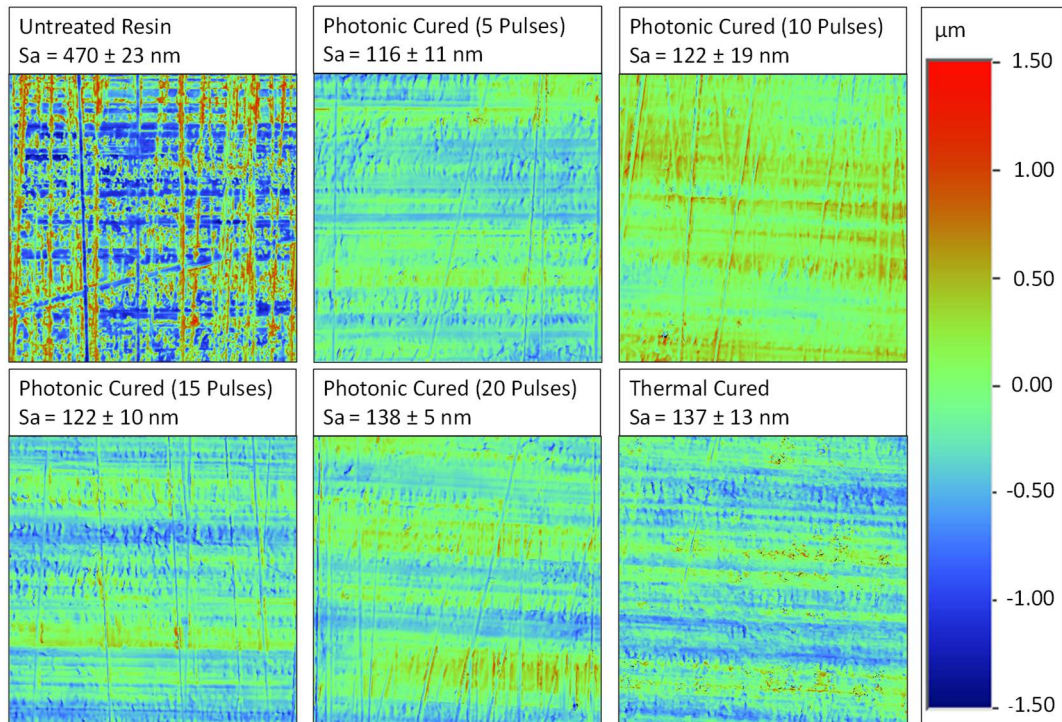
Figure 32. White light interferometry images of phenol formaldehyde resin, photonic cured carbon samples and thermal cured glassy carbon. All Images are of 200x200 μm dimensions.

4.5.2 Raman spectroscopy

The Raman spectra of both the thermal cured carbon and the photonic cured carbon are presented, discussed, and reviewed in this section.

Figure 33 presents Raman spectroscopy data of the precursor exposed to a different number of pulses via the photonic curing method, ranging from 0 to 3 pulses. The precursor itself is not Raman active, whereas the glassy carbon is Raman active, this provides a simple method of detecting carbonization of the precursor. The development of carbonization using photonic curing displayed in figure 33, this illustrates that it takes 3 pulses of 27 J/cm^2 energy output to start carbonizing a 1-2μm layer of phenol formaldehyde precursor on stainless steel.
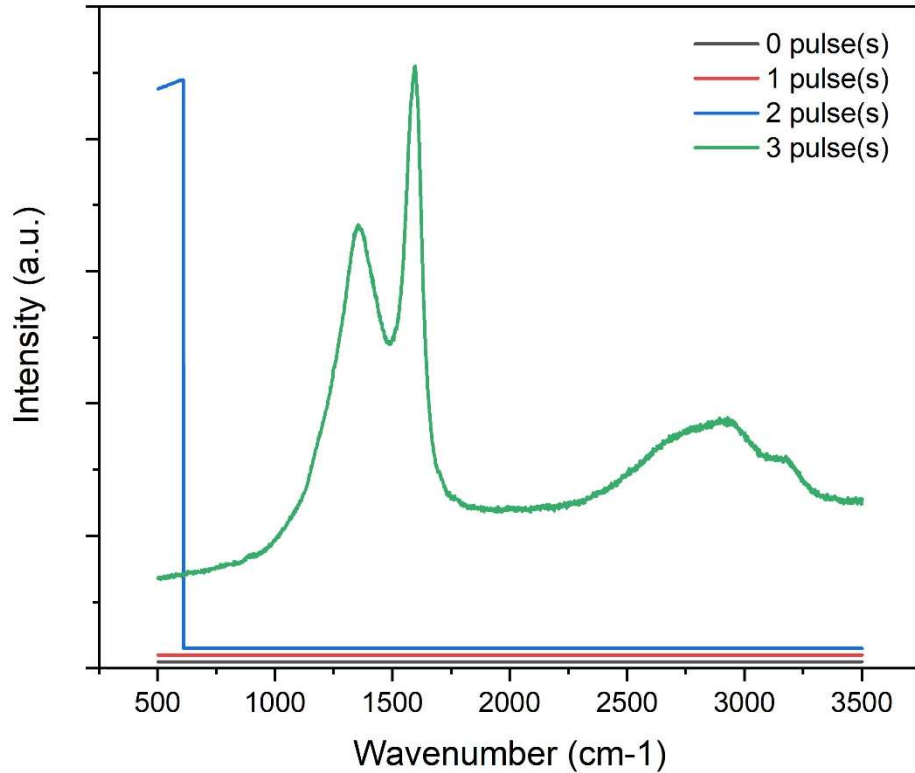
Figure 33. Raman spectroscopy of the phenol formaldehyde precursor and its transformation to a predominantly carbon material with an increase in pulse number.

Raman spectroscopy of carbons revolves around 4 major peaks; *D*, *D'*, *G* and *T* band peaks (at around 1360, 1620, 1590 and 1060 cm^{-1} respectively). From the locations, shapes and relative intensities of these 4 peaks the carbon-carbon bond structure can be deduced. The two main sp^2 bonded carbon peaks are the *D* band (carbon ring breathing mode) and the *G* band (sp^2 bonded carbon stretching mode) at ~1360 cm^{-1} and ~1590 cm^{-1} respectively. The *T* peak (~1060 cm^{-1}) is an indicator for sp^3 bonded carbon in the sample. The *D'* peak is an indicator of the grain size of the carbon material, located at 1620 cm^{-1} (51,86–88). This *D'* peak becomes more prominent as the grain size increases, which in the case of glassy carbons is associated with an increase in carbonization temperature. From the amorphization trajectory in the study of disordered carbons by Ferrari *et al.* (55), the *G* band location and the relative intensity ratio between the *D* and *G* band (referred to as *I(D/G)*) can be used to estimate the relative sp^2 and sp^3 content of the carbon samples.

The Raman spectra of photonic cured (5, 10, 15 and 20 pulses) and thermal treated coatings are compared in figure 34. Mean I(D/G) ratios are indicated together with standard deviation based on three repeat measurements at different locations on each sample. The Raman spectra of the polymer precursor without thermal treatment was not

Raman active. The Raman spectrum of the conventionally thermal treated coatings showed the typical glassy carbon shape that would be produced at the low end of the typical heat treatment temperature (HTT) range. The *D* peak was less intense than the *G* peak, whereas its full-width half maximum (FWHM) was approximately 3 times the that of the *G* peak. The secondary peaks in the 2000-3500 cm^{-1} range were present but at low intensity and merged. All these Raman characteristics are typical of low HTT glassy carbon from literature (39,47,52,53,86,87).
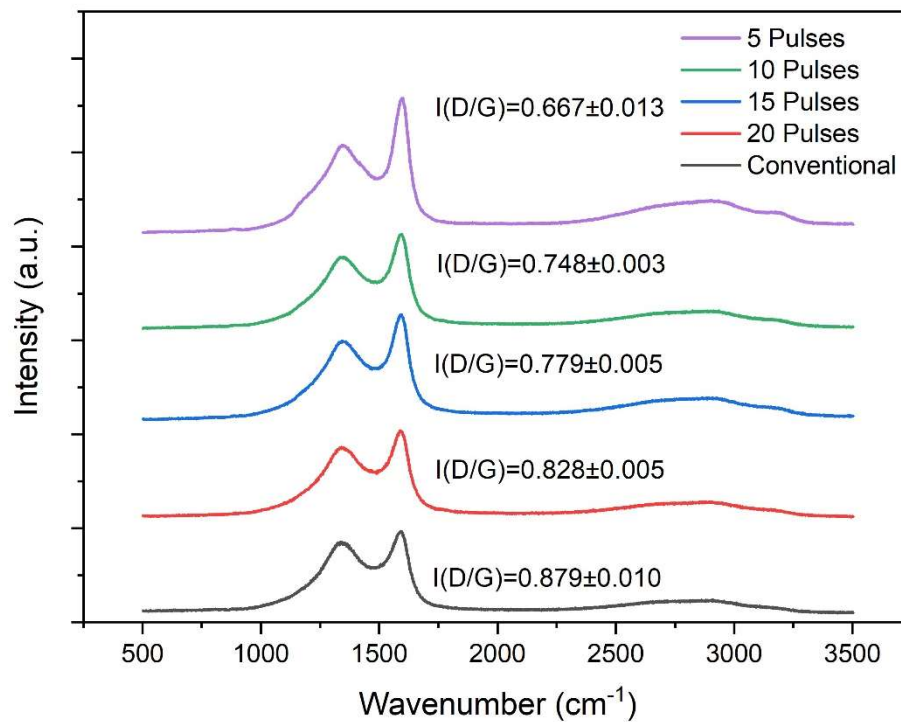
Figure 34. Raman spectra of photonic curing progression compared to conventional thermal carbonization method.

For the photonic cured samples, progressing through the number of pulses emitted, the first Raman active sample was observed after 5 consecutive pulses, amounting to a total of 100 ms exposure time and ~135 J cm^{-2} energy density exposure. A bulge was evident at ~1150 cm^{-1} in the sample subjected to 5 pulses but it steadily diminished with longer photonic curing treatment (figure 34). Carbon *D* and *G* band peaks were present in all samples, the *D'* peak was obscured by the *G* band peak suggesting a small grain size in the carbon coatings which is consistent with the relatively low carbonization temperatures used to produce these coatings (52,55). There was an increase in the intensity ratio between the *D* and *G* band as the number of pulses increased, starting with an *I(D/G)* ratio

of 0.67 after 5 pulses, increasing to 0.83 after 20 pulses, and compared with 0.88 for conventional thermal treatment. A high degree of consistency was observed in repeat measurements on the same sample, with standard deviations all being below 2% of the mean. This increase in *I(D/G)* with an increase in number of pulses is analogous to behaviour observed in literature with increases in the heat treatment temperature when producing glassy carbon (47) since more pulses means higher material temperature. From the 'Three stage model' presented by Ferrari *et al* (52,55), it is known that that the combination of a *G* peak location between 1580-1600 cm^{-1} coinciding with an *I(D/G)* value ranging between 0.5-2.0 indicates a dominance of *sp^2* bonded carbon (39,47,52,53,86,87). Hence the Raman spectroscopy data shows that carbon coatings produced using thermal heat treatment and photonic curing methods both predominantly consisted of *sp^2* bonded carbon.

The 20 pulses photonic cured sample was the most similar to the thermal cured carbon coating. The underlying individual Raman peaks were fitted and compared in more detail for the thermal cured and 20 pulses photonic cured samples in figure 35. Both of these spectra consisted of the same primary and secondary peaks, thus demonstrating fundamental similarities between the two resultant carbon coatings. The primary peaks were due to the *D* band (carbon ring breathing mode) and *G* band (*sp^2* bonded carbon stretching mode) at ~1360 cm^{-1} and ~1590 cm^{-1} respectively. The secondary peaks consisted of the *2D* band (~2600 cm^{-1}) and the *D+D'* band (~2900 cm^{-1}).

The *G* band in both carbonization methods is located at 1590 cm^{-1}, the D bands are in similar positions, 1357 cm^{-1} for the thermal curing method and 1360 cm^{-1} for the photonic curing method. The full-width half maximum (FWHM) of the G band peak correlates directly to the measure of disorder, with an increase in FWHM demonstrating greater disorder (55). The conventional method Raman spectrum *G* band had a FWHM of 102 cm^{-1} while the photonic curing *G* band gave a FWHM of 97 cm^{-1}. This indicates that the materials produced from both methods had similar levels of disorder in their structures.
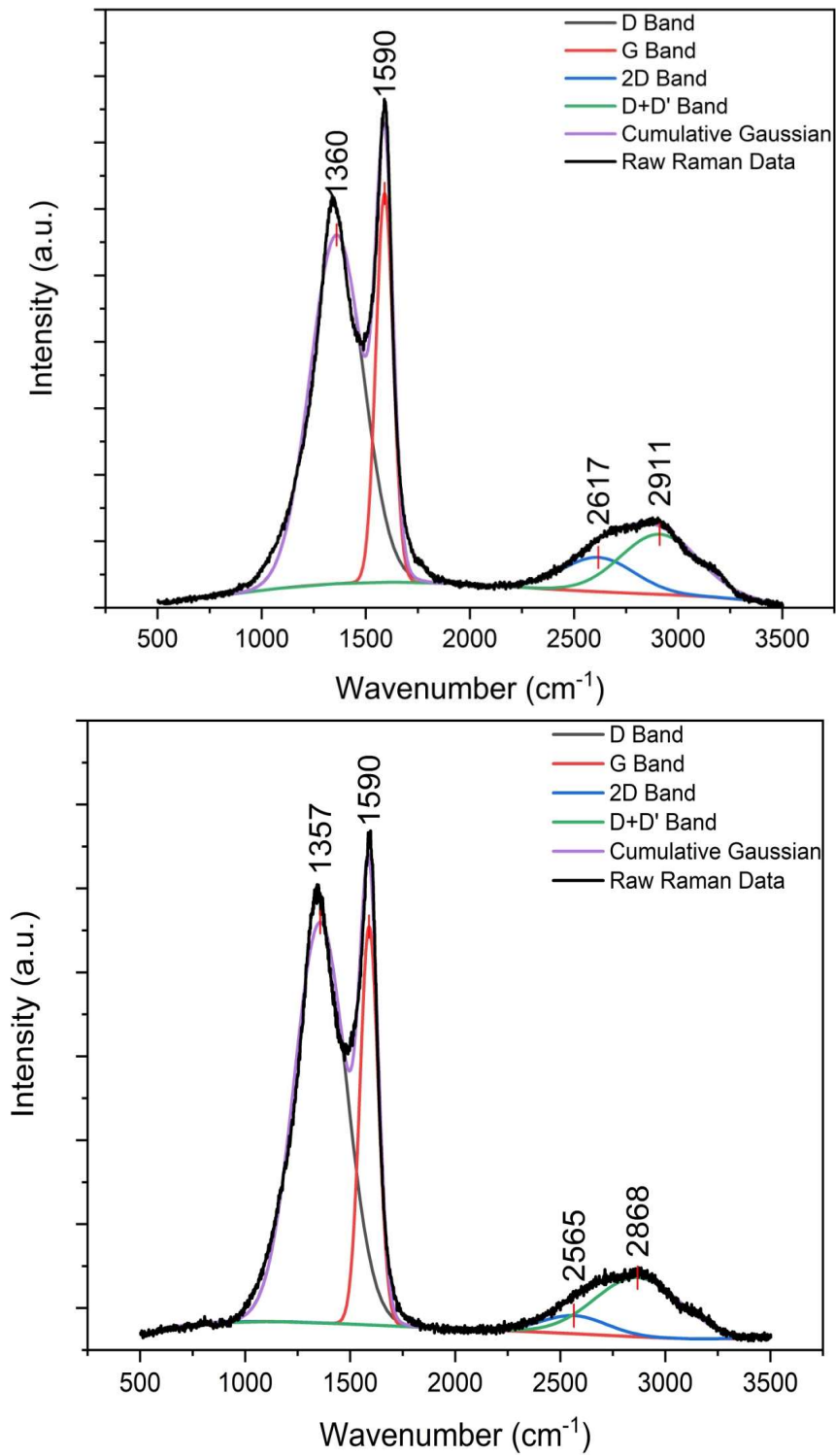
Figure 35. Raman spectroscopy curve fitting of carbon coatings carbonized using the 20 pulses photonic curing method (top) and the thermal curing method (bottom)

4.5.3 XPS analysis of treated materials

This section is dedicated to the characterisation method of X-ray photoelectric spectroscopy. The XPS spectra of both the thermal cured carbon and the photonic cured carbon are presented, discussed. The XPS data was collected by Dr. James McGettrick, who also aided in the interpretation of the XPS data.

The XPS spectra of photonic cured (5, 10, 15 and 20 seconds) and thermal treated coatings are compared in figure 36 and show primary peaks at ~284-285 eV and ~ 531-533 eV binding energies. These two peaks are indicative of carbon-carbon (C1s) and carbon-oxygen (O1s) bonds which are expected for carbon material derived from an organic polymer precursor (79,89,90). Figure 36, further, demonstrates the similarity of the chemical content distribution of the carbon coatings and allows the chemical distribution of each coating to be calculated using the relative areas under the peaks. Conventional method GC coatings contain ~97% carbon content and ~3% oxygen content, compared to the photonic cured coatings which contain ~96% carbon content and ~4% oxygen content. The oxygen content difference between the carbonization methods is negligible and these values are in line with similar studies on commercially manufactured glassy carbon from Lim *et al*. (48) and Yi *et al*. (17).
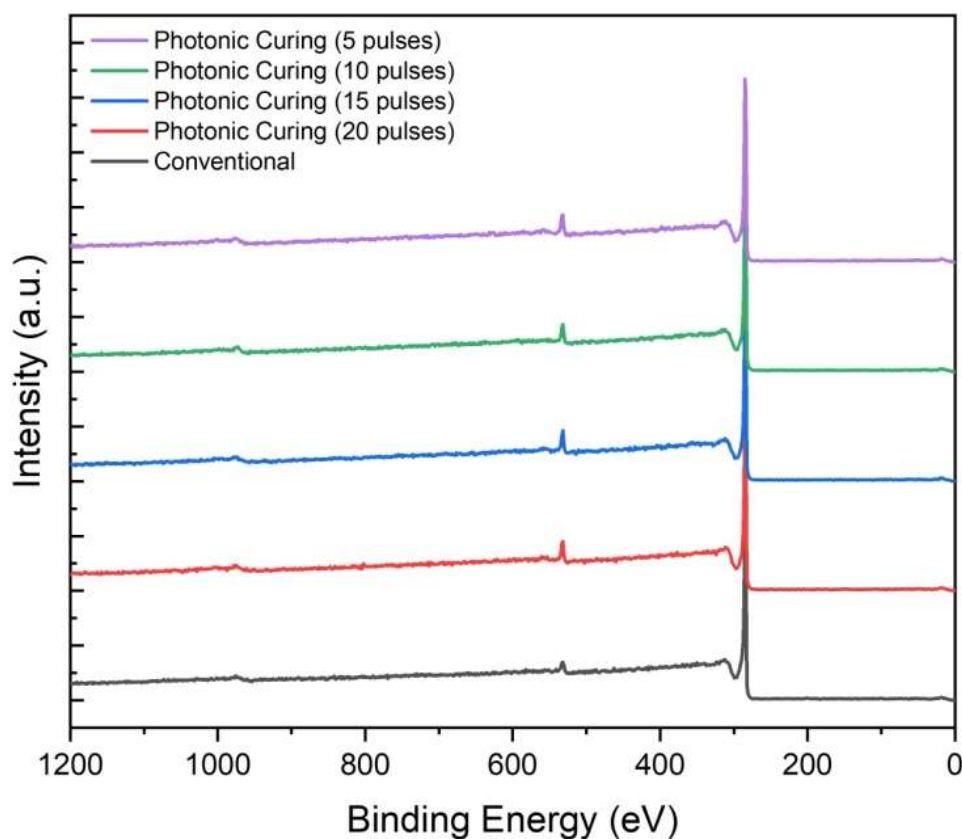
Figure 36. Surface chemistry analysis XPS spectrum comparing carbon coatings manufactured using the photonic curing method (red, blue, green, purple) and the conventional method (black).

The primary carbon peaks (C1s) of the carbon coatings are compared in figure 37 against graphite (exclusively sp^2 bonded carbon) and diamond (exclusively sp^3 bonded carbon), the reference materials that reside on either extreme of the carbon bonding spectrum. The location and shape of the peaks in figure 37 show that the thermal and photonic cured carbon peaks are located in the same position as the reference graphite sample (sp^2 only) at ~285.0 eV and that they are of similar shape, with a high binding energy tail indicative of the presence of sp^2 carbon. The sp^3 diamond peak is clearly located at a lower binding energy of ~283.5 eV and has a different shape with a bulge on the lower binding energy side of the peak. Unlike graphite or the glassy carbon coatings, with their expected high sp^2 carbon content, and ability to resupply electrons, the diamond required charge neutralisation and hence shifted to a lower binding energy. These results indicate that the photonic cured and thermal cured carbon have similar carbon-carbon bond structures to the graphite reference sample.
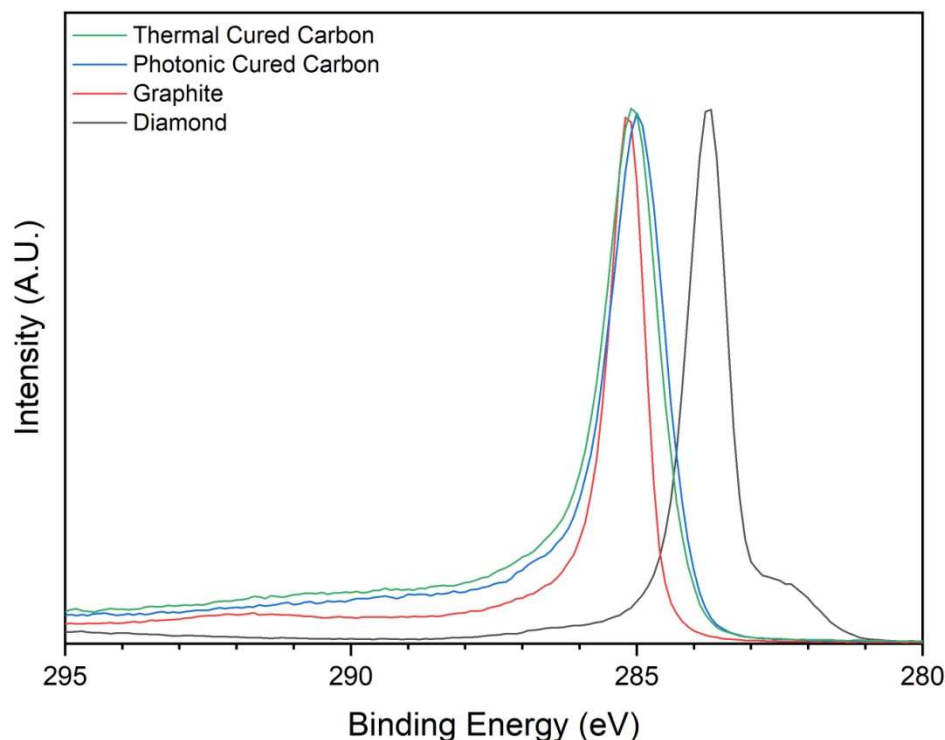
Figure 37. XPS highlighting the carbon (C1s) peaks exclusively, comparing photonic and thermal cured carbon to reference materials (graphite and diamond).

A further XPS test was performed on the samples at a higher binding energy (1190-1250 eV) (figure 38). In this range, carbon materials have another peak known as the Auger peak (C KLL). This Auger peak is the observation of an electron going through a unique transition between energy levels known as the Auger electron (90,91). With mathematical manipulations to the Auger peak data an empirically derived value known as the *D* parameter can be calculated. The *D* parameter is defined as the binding energy difference between the position of highest peak and the lowest trough of the Auger peak (C KLL) and is calculated from the first derivative between these positions, and has been used to empirically determine the sp^2/sp^3 bonded carbon ratio of carbon materials (89,90). Using the CasaXPS software, the C KLL peak data were smoothed and differentiated as suggested by Kaciulis *et al.* (79). Adopting the assumption that diamond has 0% sp^2/100% sp^3 carbon bonds and graphite has 100% sp^2/0% sp^3 carbon bonds, a linear relationship between the *D* parameter and the sp^2 content percentage can be established as demonstrated in figure 38 *(right)*.   Using this empirical linear relationship, estimates for carbon materials with unknown sp^2/sp^3 ratios can be made, leading to thermal cured glassy carbon having an estimated sp^2 content of 96-100%, while photonic cured carbon on the other hand showed a more even sp^2/sp^3 split at 55±4% sp^2.
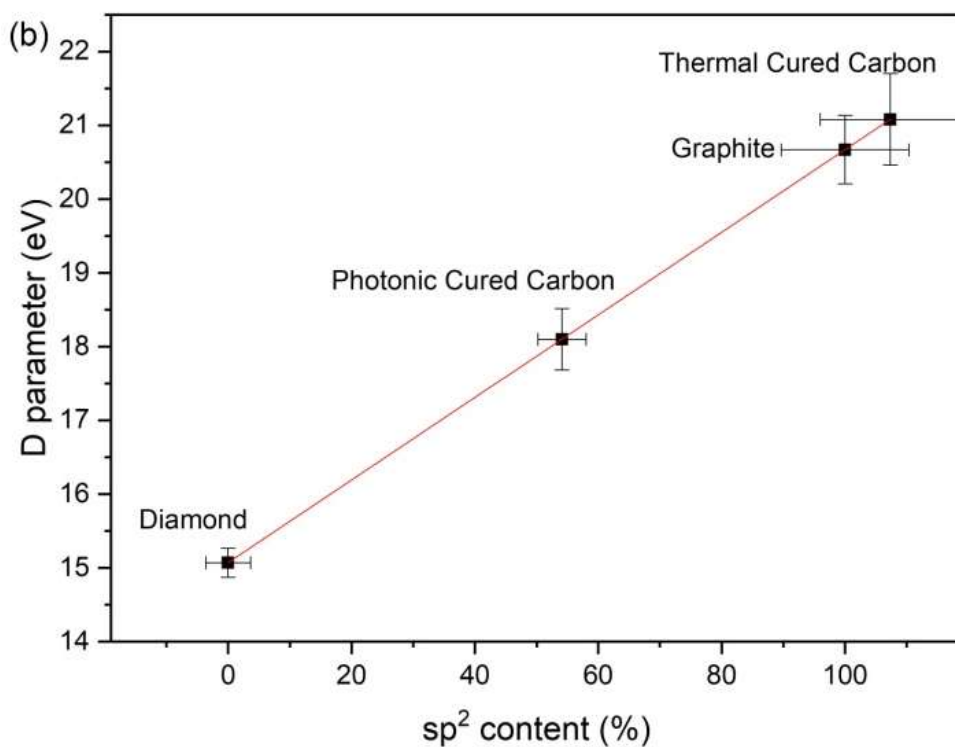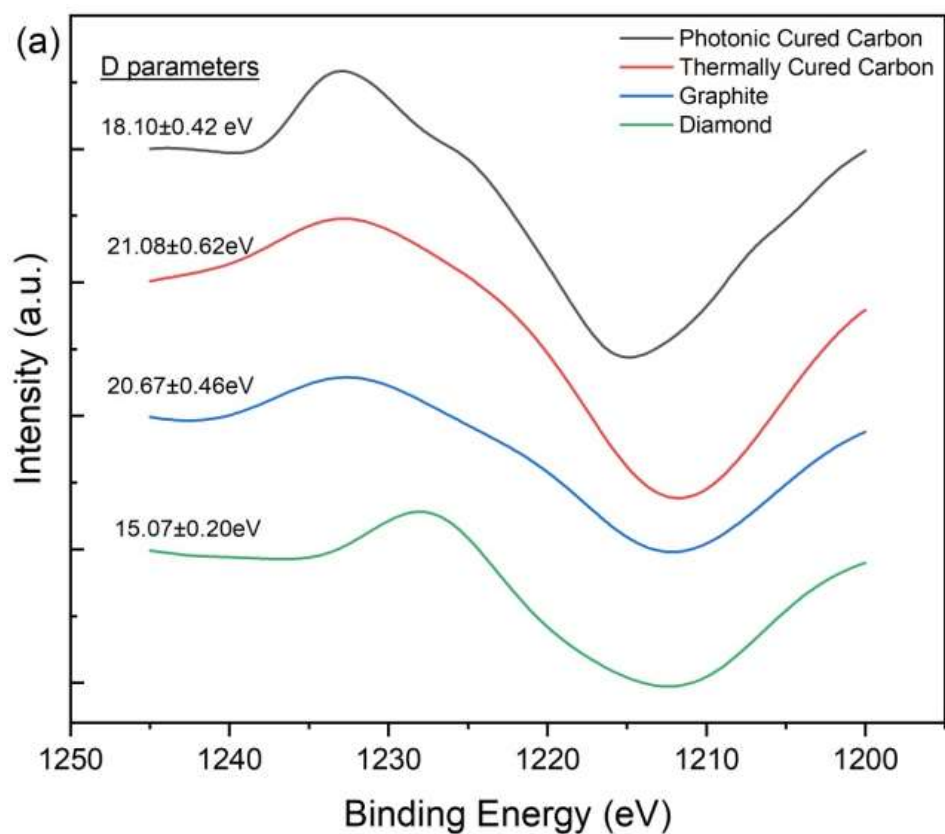
Figure 38. First derivative of Auger peaks of carbons in the 1190-1250 eV range (top) with comparison of the D parameters for evaluation of percentage sp2 bonded carbon (bottom).

The apparent sp^2 content differed depending on the analysis technique used. Using Raman spectroscopy, predominantly sp^2 content was observed both for photonic and thermally derived carbon coatings. However, XPS analysis indicated a mixed ~55% sp^2 structure for the photonic derived carbon and a much more exclusively sp^2 structure for the thermally derived carbon coatings. A key distinction between these two analysis techniques is the penetration depth. The penetration depth of Raman spectroscopy is dependent on the wavelength of the laser as well as the reflectance of the studied material. The penetration depth of Raman spectroscopy is ~60nm using a 514.5nm laser when studying glassy carbon, whereas the same laser wavelength in a tetrahedral amorphous carbon achieves a penetration depth of 1.5 micron, demonstrating the dependency on both wavelength and reflectance of the material. Thus the 532nm wavelength Raman spectrometer laser used to acquire the Raman data in this thesis is expected to have similar depth of penetration, and is therefore more representative of the bulk characteristics compared to the XPS data. The conclusions drawn from the Raman data are however limited by the single wavelength of the instrument used. (117). On the other hand, XPS is focussed on the chemistry at approximately 5-10 nm from the surface, and is therefore primarily indicative of the surface. This suggests a difference in the morphology at the immediate surface of the photonically cured coating when compared with the bulk. This might be associated with the local environment around the transitioning samples. Conventional thermal conversion takes place in a consistent environment at 800°C, with a slow and continuously purged carbonisation process. The photonic conversion occurred at close to ambient temperature, with heat directed at the sample surface and not the gas space around it. There are also differences in the rate at which the off-gases are produced by the different techniques, which might affect the chemical content of the gas space. This could potentially be explored with a larger sample enclosure and more aggressive purging. Despite this the photonic route offers a rapid means of producing glassy carbon, in seconds or minutes compared with hours, with potential for a host of new applications, even on temperature sensitive substrates which would be destroyed with conventional processing.

4.6 Follow-on Photonic Testing

Following the experimental trials and presented above, the photonic curing unit from Novacentrix malfunction and hence therefore could not be used for further evaluation of photonic cured carbon on alternative substrates. An attempt was made to produce glassy carbon coatings using photonic curing on alumina, aluminium and glass substrates by using

facilities at Precision Varionic International (PVI) in Swindon, UK. A photonic curing system manufactured by Novacentrix was used with a lamp of output ~14 J/cm2, which is about half the energy density output of the university lamp. Even with maximum energy output settings the energy output was not enough to successfully carbonize the phenol formaldehyde precursor on the alumina, aluminium, and glass substrates. Pulse numbers in excess of 100 were used to try to achieve complete carbonization of the precursor compared to the 20 pulses used in the university photonic curing system. A preliminary conclusion was drawn that a smaller number of pulses using higher energy output is more efficient at carbonizing than a high number of pulses using a lower energy output, even if the total energy output is the same.

4.7 Chapter closure

Characterisation of the photonic cured carbon demonstrates a structural and material close match to thermally cured carbon.

Comparing the photonic and thermal cured carbons visually they both look like glassy carbon, a super-smooth flexible sheet deep shiny black reflective coating deposited on 316 stainless steel in this case. Taking a closer look at the SEM images, it's observed that this ultra-smooth surface also exists when we look at an image of approximate 3x4 micron. Self-inflicted surface defects are required to see the carbon surface against exposed steel, otherwise you'd be looking at a uniform grey haze. Using white light interferometry to quantify the surface roughness it's observed that the photonic and thermal cured carbon have surface roughness's after conversion that lie within standard deviation with *Sa* in the range of ~110-140nm. This surface roughness may be partially imparted by the roughness of the substrate but can't be exclusively due to the substrate as the precursor coated on the same substrate had a significantly higher *Sa* at 470nm.

To analyse the carbon-carbon structure Raman spectroscopy was employed Raman spectroscopy of the wavelength used has a penetration depth of ~1μm in carbons, therefore it's a reflection of the overall structure of the studied carbon layers. Theoretically glassy carbon consists of an sp^2 dominated carbon-carbon structure, therefore its expected that its Raman spectrum is dominated by a D-band peak and a G-band peak at wavenumbers ~1360 and ~1590cm^{-1}. The photonic and thermal cured carbon has dominant peaks at these locations. The "low-energy" photonic cured carbon at 5 pulses clearly

demonstrates a bulge at ~1150cm^{-1} which disappeared with increasing the number of pulses thus likely to be an effect of incomplete carbonization. The intensity ratio between the D and G band peaks in glassy carbon are an indicator into the heat treatment temperatures used to carbonize the precursor, I(D/G) increases with heat treatment temperature. This is further confirmed when observing this intensity ratio change with the number of pulses using the photonic curing method, and therefore the amount of energy put into the surface of the precursor. The photonic cured samples of 5, 10 and 15 pulses have I(D/G) = 0.67, 0.75, 0,78 respectively demonstrating the increase in input energy results in an increase in I(D/G). The thermal cured glassy carbon has I(D/G) = 0.88 and the photonic cured carbon (20 pulses) has I(D/G) = 0.83, showing that 20 pulses of the given photonic curing settings results in a similar carbon structure as a conventionally carbonized glassy carbon at 800°C. As the phenol formaldehyde resin precursor is not Raman active it's clear that carbonization of the precursor starts after 3 pulses of a 27 J/cm^2 via photonic curing as the flat line of the precursor then changes to a recognizable Raman spectrum with a D and G band peak accompanied by a combination of secondary peaks. Raman spectrum secondary peaks, in the region of wavenumbers 2500-3200cm^{-1}, the spectra of the thermal and photonic cured carbon are identical, further reinforcing the similarity between the structure of these two materials.

X-ray photo electric spectroscopy (XPS) is used to further study the structure of the carbon layers manufactured by alternate methods. XPS has penetration depth of the order of nanometres, thus it analyses the surface structure of the studied carbon instead of the bulk of the layer in contrast to Raman spectroscopy. The XPS spectra of both the photonic cured carbon and thermal cured carbon show primary peaks at ~284-285 eV and ~ 531-533 eV binding energies, indicative of carbon-carbon (C1s) and carbon-oxygen (O1s) bonds which is expected for carbon materials derived from an organic polymer precursor (79,89,90). The chemical distributions of the photonic and thermal cured carbons are similar with the thermal cured carbon containing ~97% carbon and ~3% oxygen and the photonic cured carbon containing ~96% carbon and ~4% oxygen. These values are in-line with similar studies on commercially manufactured glassy carbon from Lim *et al*. (48) and Yi *et al*. (17). Studying the carbon primary peaks in depth, the photonic and thermal cured carbons are compared to reference samples of graphite and diamond which are exclusively *sp^2* and *sp^3* bonded respectively. The graphite reference sample (*sp^2*) has peak location 285.0 eV and the diamond reference sample (*sp^3*) has a peak at 283.5 eV, displaying a clear difference in location due to carbon-carbon bond type dominance. The photonic and

thermal cured carbon XPS spectra are of identical shape and location, also having peak location at 285.0 eV, sample as graphite reference sample, but are of wider FWHM which is indicative of other bond types which could be caused by some sp^3 bonded carbon or some types of carbon-oxygen bonding. The carbon produces a secondary "Auger" peak in the binding energy range of 1190 – 1250 eV, which is used to empirically derive the carbon bond type distribution. The graphite and diamond reference samples are analysed first to build the empirical spectrum between sp^2 and sp^3 bonded carbon. The photonic and thermal cured carbon data are then plotted on the same spectrum based on their D parameter, which is defined as the difference in binding energy between the peak and the trough of the first derivative of the Auger peak. This method concludes that the thermal cured carbon consists of 96-100% sp^2 bonded carbon and the photonic cured carbon consists of 55±4% sp^2 bonded carbon. This is the first (and only identified) difference between the thermal and photonic cured carbon, but it must be considered that XPS is strictly a surface chemical analysis only (nanometre thick), Raman spectra data suggests a near identical bulk structure. It could be envisaged that this surface difference could be induced by the surface being exposed to significant difference in temperature of surrounding air (ambient for Photonic cured vs high temperature in carbonisation) during the carbonisation process, it could be envisaged that due to rapidity of photonic curing the ambient temperature unable to influence the bulk of carbonisation, but only exposed nanometre-thick layer.

In conclusion, material characterisation demonstrated substantial similarity between the photonic cured carbon and the conventionally thermally cured glassy carbon, both matching literature definition of glassy carbon. Having developed a novel methodology to produce glassy carbon thin films using photonic curing, the next chapter will explore the use of thermal and photonic cured glassy carbon as the active anode material for energy storage devices. A comparison between the thermal and photonic cured carbon thin films for printed electronics and sensor applications was planned but not achieved due to the malfunctioning of the photonic curing system, thus only thermal cured carbon thin films are used in the chapter researching the viability of glassy carbon in printed electronics and sensors.

Chapter 5: Glassy Carbon Electrodes: Photonic Cured versus Thermal Cured Carbon

5.1 Introduction

The previous chapter underlined that, from a material characterisation perspective, there is substantial similarity between the photonic cured carbon and the conventionally produced thermal cured glassy carbon, both matching literature definitions of glassy carbon (2–9).

In this chapter the viability of using glassy carbon as an active anode material was explored by investigating the electrochemical performance between the two different carbonised glassy carbons. Electrochemistry is one of major field of application of glassy carbon, especially in the role of counter electrodes for its low reactivity, chemical resistivity and electrical conductivity (7,18,70,92). Electrochemical testing of the thermal and photonic cured carbon thin films aimed to compare crucial energy storage characteristics such as the voltage stability window, process type, equivalent series resistance, capacitance and Coulombic efficiency to compare the performance of two materials as anode electrodes. Cyclic voltammetry (CV), electrochemical impedance spectroscopy (EIS) and galvanostatic charge/discharge (GCD) are the chosen analysis methods. If glassy carbon thin films display usable energy storage characteristics they could have potential use in energy storage systems utilizing electrolytes of high reactivity.

5.2 Half Cell Testing: Glassy carbon as anode material

Half-cell testing adopting photonic cured and thermal cured carbon as anode materials was performed. All electrochemical testing of the thermal and photonic cured carbon coating materials were performed in a sodium sulphate (Na_2SO_4) electrolyte of 0.5 $moldm^{-3}$ concentration. Platinum coil was chosen as the counter electrode and silver-silver chloride (Ag/AgCl) was chosen as the reference electrode, as is standard in aqueous electrolytes. The photonic cured sample used in all the following experiments is one of the samples exposed to 20 pulses as this sample is characteristically most similar to the thermal cured carbon.
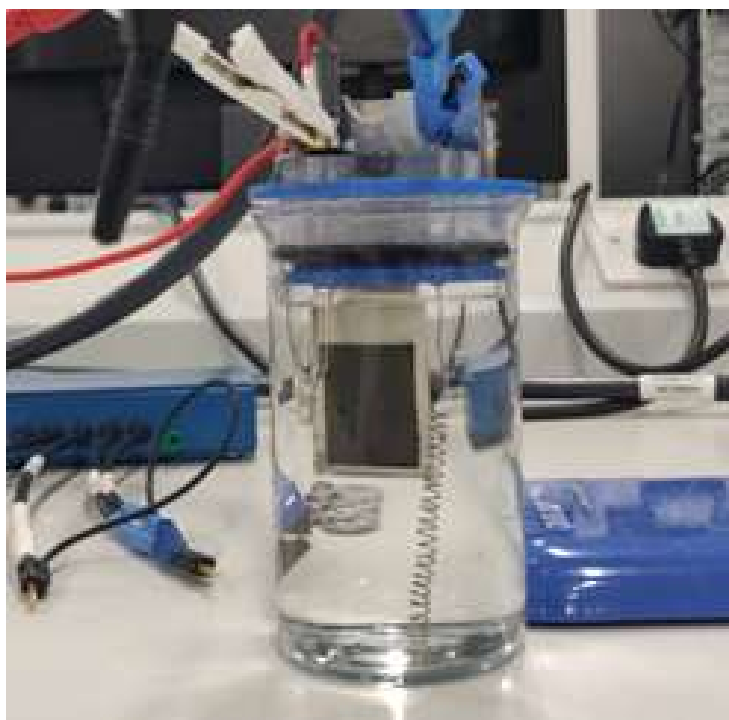
Figure 39. Aqueous half-cell setup with a photonic cured glassy carbon working electrode, silver/silver chloride reference electrode and a platinum coil counter electrode. Electrolyte is 0.5M sodium sulphate aqueous solution.

Scattered measurements are taken to minimize systematic error in all measurements. For example, for the cyclic voltammetry, instead of taking the measurements simple in ramping scan rate from 10mV/s to 1000mV/s, the measurements were taken by "leap-frogging" every other scan rate and measuring the left-over scan rates when the largest desired scan rate was measured. E.g., 10, 30, 50, 200, 400, 1000, 20, 40, 100, 300, 500 mV/s.

5.3 Cyclic voltammetry

Cyclic voltammetry is used as a starting point for the electrochemical performance testing to follow as it will determine what voltage and current windows to explore when studying the electrochemical impedance spectroscopy and the galvanostatic charge/discharge data of the two carbon materials.
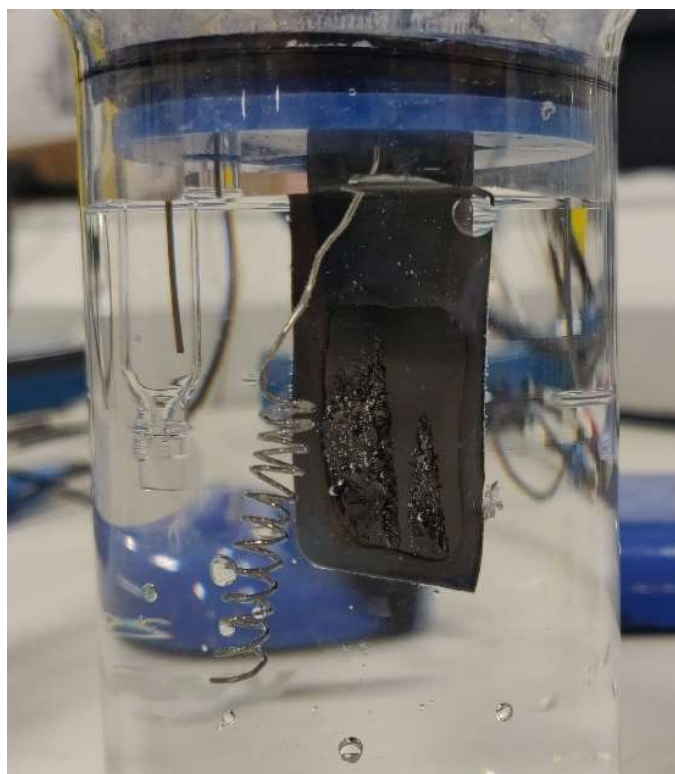
Figure 40. Glassy carbon delamination off stainless steel substrate during CV cycles and gas formation by pushing the voltage window to far while searching for the voltage stability window.

In figure 40 the half-cell setup is shown where the boundaries of the voltage potential window are pushed too far outside of the materials' stability window and some delamination of the carbon coating off the steel substrate is occurring as well as some gas formation by way of water splitting on the platinum wire coil counter electrode and on the edges of the working electrode.
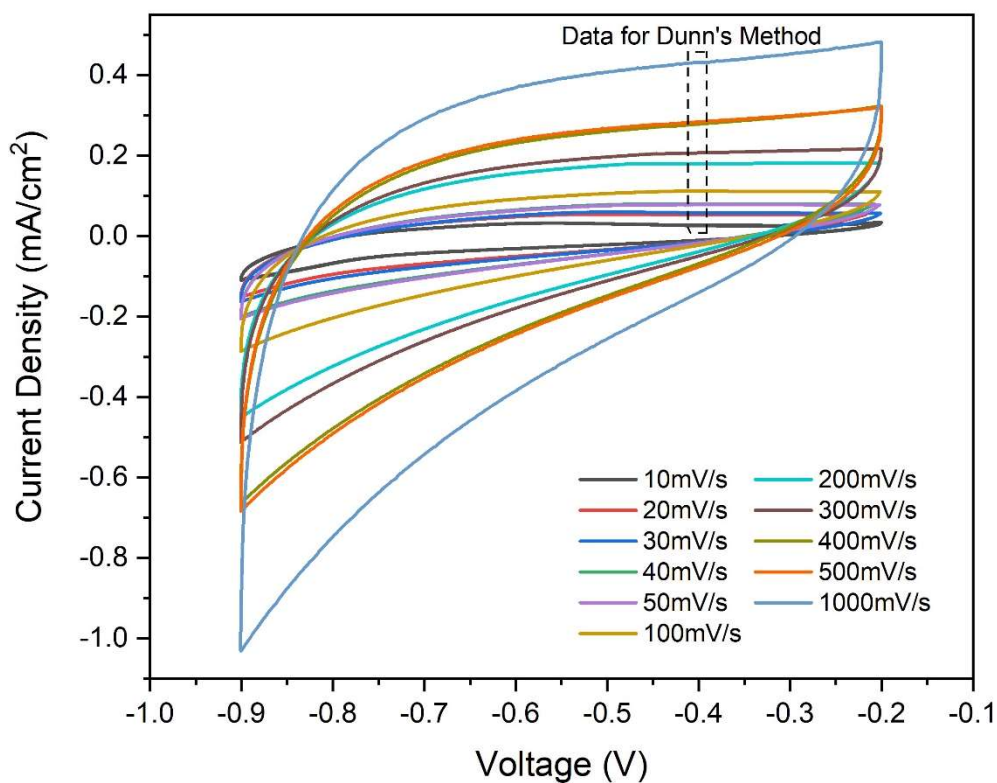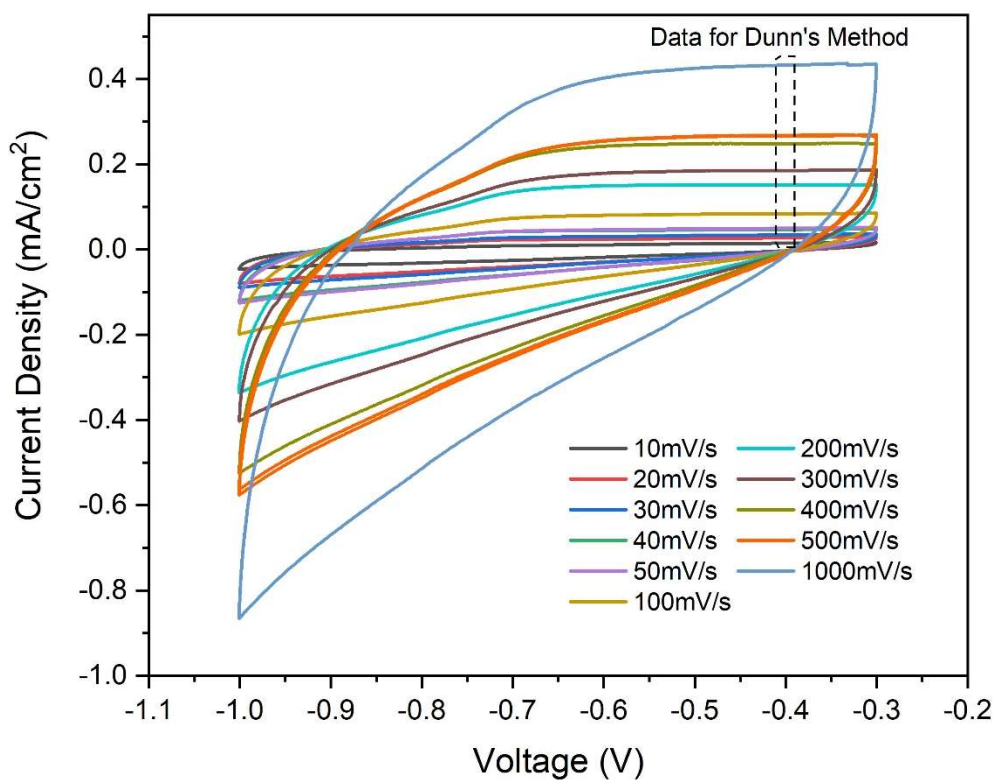
Figure 41. Photonic Cured 20 pulses sample (top). Stability window of ~0.5 between -0.35V and -0.85V. Thermal cured carbon sample (bottom). Stability window of ~0.5 between -0.3V and -0.8V. Box surrounding the data points at 0.4V taken for Dunn's method.

Both the photonic and thermal cured carbon coatings show similar CV shapes, a relatively flat top on the increasing potential sweep demonstrating it behaves like a capacitor in this region under increasing voltage conditions. On the decreasing potential sweep the slope is much steeper compared to the positive potential sweep, meaning it behaves more like a resistor under these conditions. A total of 5 CV sweeps were taken per scan rate per sample, this enables the ability to use 5 values for current density at 0.4V for Dunn's method (80–82,93), as demonstrated in figure 41. 5 values for current density were used to calculate an average with a standard deviation which is plotted against the scan rate in figure 42.
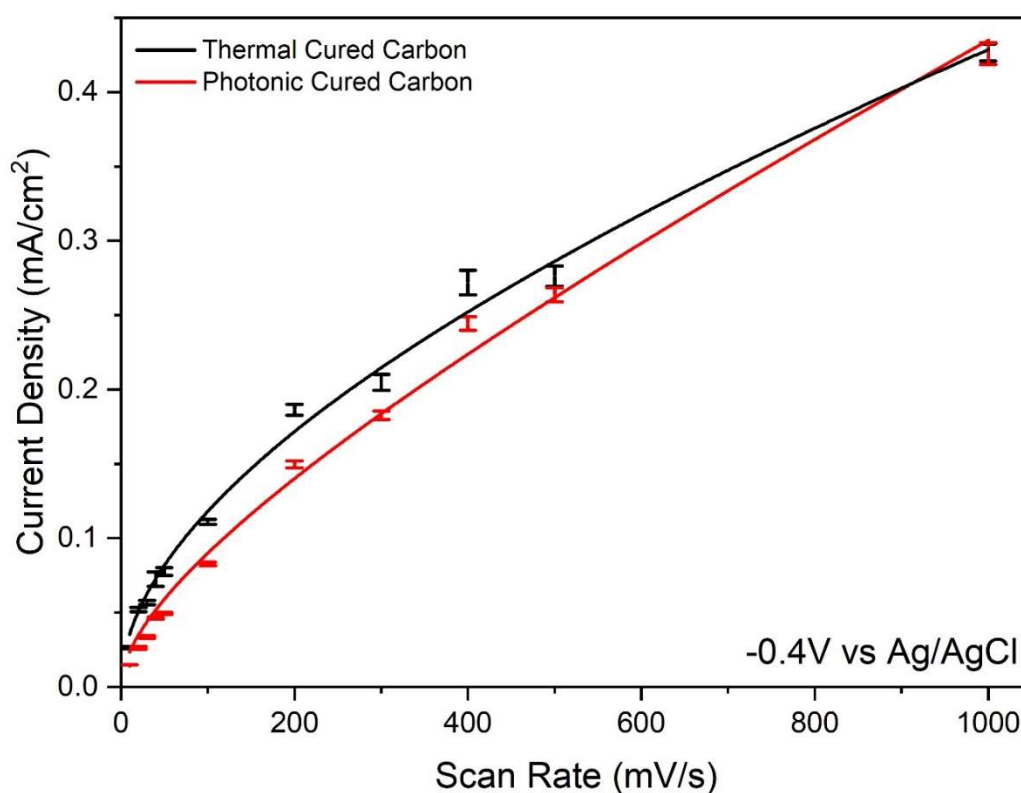
Figure 42. Dunn's method comparing photonic cured carbon to thermal cured carbon. Both current densities are taken on the ramping voltage part of the sweep at -0.4V which is a stable voltage for both samples.

Using Dunn's method in figure 42 we can determine what controls the carbon film charging/discharging process. If the carbon layer is a surface-controlled process the current would be proportional to the scan rate in a linear fashion;

$$I \propto scan\ rate.$$

If the carbon layer shows a diffusion-controlled charging process the current would be proportional the to square root of the scan rate;

$$I \propto \sqrt{scan\ rate}.$$

From figure 42 both the photonic and thermal cured carbon coatings exhibit a linear relationship between the current and the scan rate, and between the current and the square root of the scan rate. Thus, the reactions are being controlled by both diffusion and surface charging/discharge processes.

The fitted curve in figure 42 is modelled after a combination of previously discussed relationship between current and scan rate. Thus the current density is defined as

$$J = A\left(B\frac{dV}{dt} + (1-B)\sqrt{\frac{dV}{dt}}\right)$$

$$\therefore if\ B \ll 1, J \rightarrow A\sqrt{\frac{dV}{dt}}$$

$$\therefore if\ B \rightarrow 1, J \rightarrow A\frac{dV}{dt}$$

Where J is the current density and dV/dt is the scan rate. Parameters A and B are numerical values to fit the plot to the data. The numerical value of B determines whether the data suggests a surface-controlled process or a diffusion-controlled process of the studied material. If B<<1, the linear dV/dt component of the equation becomes negligible, and thus dominated by the square root of scan rate component suggesting a diffusion-controlled process. If B → 1, the square root component becomes negligible and the linear component dominates, suggesting a surface-controlled process of the studied material.

From the fitted data in figure 42 the numerical value of B = 0.007 for the thermal cured carbon and B = 0.031 for the photonic cured carbon. Therefore, the data concludes that both the thermal and photonic cured carbon are dominated by diffusion-controlled processes during cyclic voltammetry. Hence the reaction rate between the working electrode and the electrolyte is limited by the rate of transport through the electrolyte. For future investigation of glassy carbon electrodes, a baseline of the stainless steel substrate in the same 3-electrode cell would be useful remove the potential influence of the substrate on the electrochemical characterisation.

5.4 Electrochemical Impedance Spectroscopy

EIS makes use of representative circuits to describe the behaviour of the material and the type of cell being investigated (94–96). This representative circuit can use a theoretical Nyquist plot to fit the recorded data from the investigated system to make estimations on parameters such as charge transfer resistance, internal resistance, electrolyte resistance, and capacitance of the active material. The double layer capacitance can be replaced with a constant phase element to improve the data fit if the material isn't a perfect capacitor, which may be caused by surface disorder or by different crystallographic orientations (118,119). For the thermal cured and photonic cured carbon, a variation of the Randles circuit as shown in figure 44 is used to approximate the data, this Randles circuit was based on the structural composition of the carbon electrode and proved to be a good approximation to the raw EIS data, this may be due to the high disorder of the carbon crystallite structure.
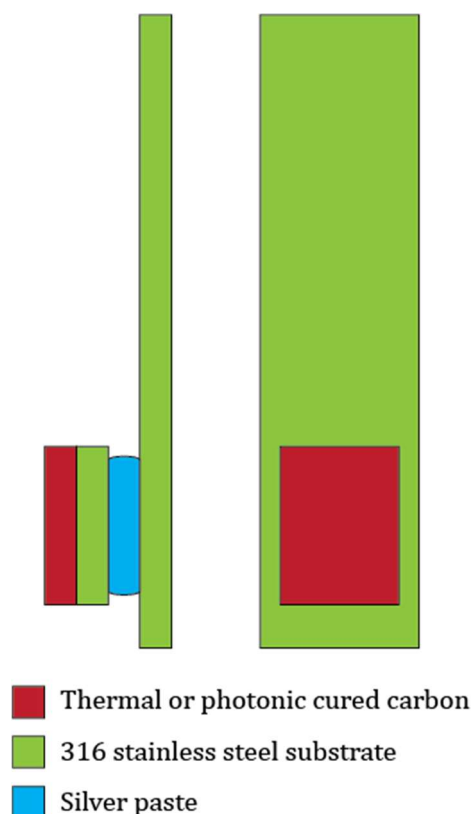
Figure 43. Schematic carbon electrode. Carbon coated on stainless steel which in turn is adhered to another stainless-steel substrate using silver paste.

Due to limited time using the Novacentrix Pulseforge 1200 photonic curing system only ~20x20mm photonic cured carbon coatings were manufactured. The half-cell testing jigs

(see figure 39) required the substrate to be ~80x20mm to comfortably get the reference and counter electrode in position near the carbon surface. Hence the carbon coatings on their stainless-steel substrates were mechanically and electrically connected to a new, larger stainless-steel substrate using a silver paste which is schematically shown in figure 43.
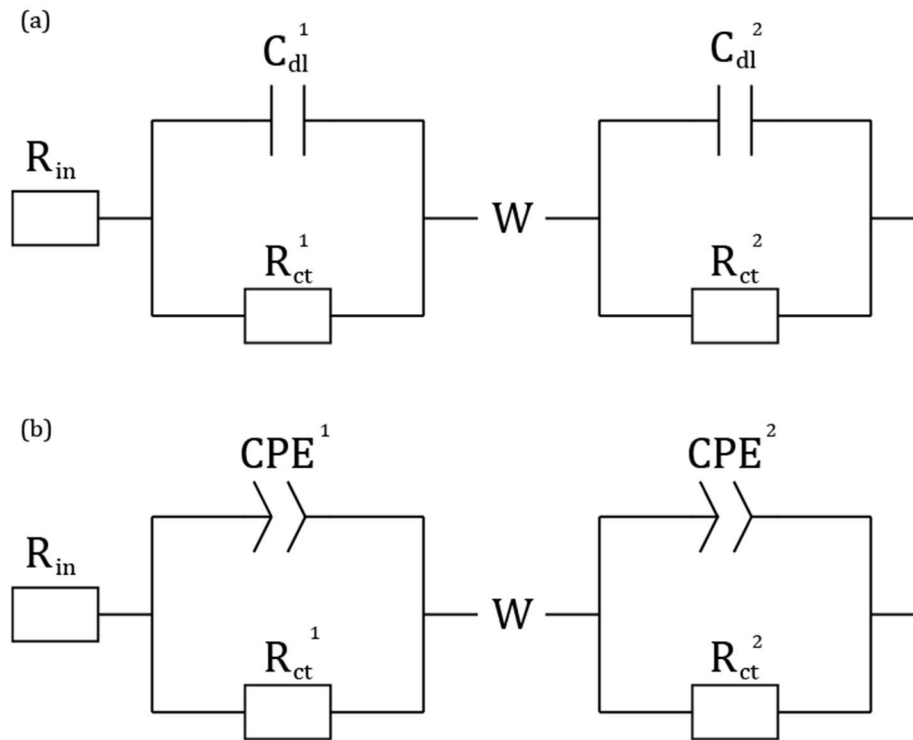
Figure 44. Randles circuit variations to fit the thermal and photonic cured carbon EIS Nyquist plot data. Part (a) is the classic combination of resistances with double layer capacitances whereas part (b) is the same circuit where the C_{dl} is replaced with a constant phase element. Both these circuits are used as a data fit in the following impedance spectra.

The Randles circuits displayed in figure 44 display the most accurate data fitting to the following EIS data of both the photonic and thermal cured carbon electrodes. Figure 44(b) replaces the double layer capacitors in the Randles circuit with constant phase elements to improve the data fitting to the raw EIS data. Warburg impedance between two sets of double layer capacitors in parallel with a charge transfer resistance suggests a diffusion layer between the carbon and the stainless-steel substrate and potentially between the two layers of stainless steel connected by silver paste. This diffusion factor is a contribution of reduction and oxidation species becoming a rate limiting factor. This is reinforced by the picture in figure 40, where the carbon layer is partially delaminating off the substrate allowing the electrolyte to dissipate between the two layers. It's difficult to say if the resin

is keeping the electrolyte from reaching the silver paste layer between the two stainless steel layers. The bilayer mechanics in the Randles circuit, the double layer capacitance and charge transfer resistance labelled with a superscript number 2, is an addition to the classic Randles circuit because of the geometric limitation of the photonic cured samples which required a standalone piece of stainless steel so that the carbon electrode fits the half-cell testing jig.
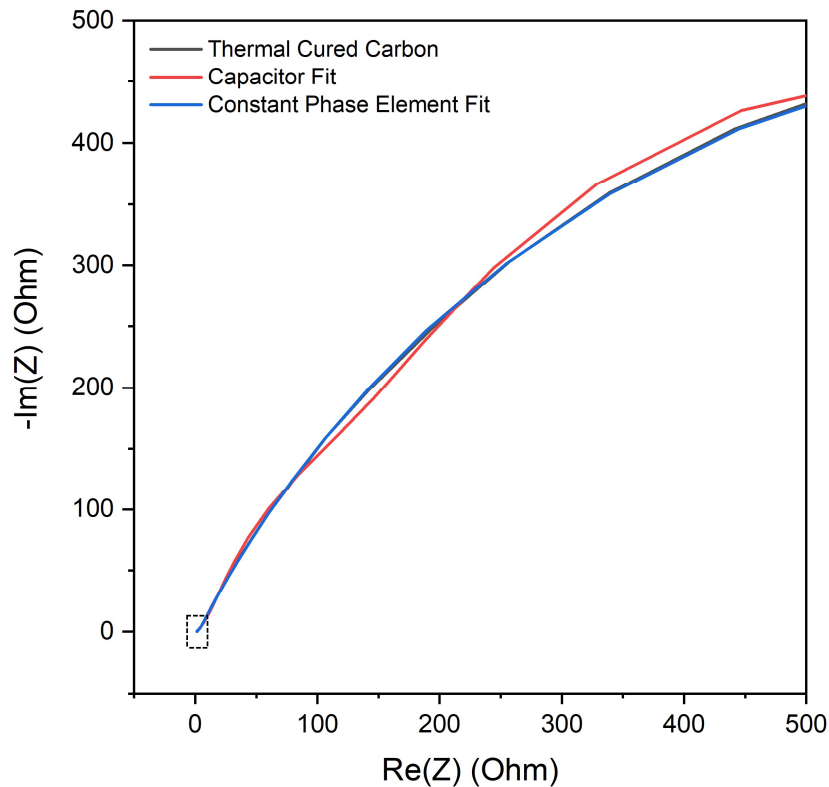
Figure 45. Electrochemical impedance spectroscopy of bar coated thermal cured glassy carbon on stainless steel substrate. The dashed-line box highlights the high-frequency end of the recorded data which is shown in figure 46.

In figures 45 and 46 the EIS data of thermal cured glassy carbon are shown alongside the fitted data of two different equivalent Randles circuits. In these figures the red data set (named capacitor fit) is an approximation data set which uses a Randles circuit with a double layer capacitance as shown in figure 44(a). The blue data set (named constant phase element fit) is an approximation data set which uses a Randles circuit with a constant phase element instead of a double layer capacitance as described in figure 44(b).
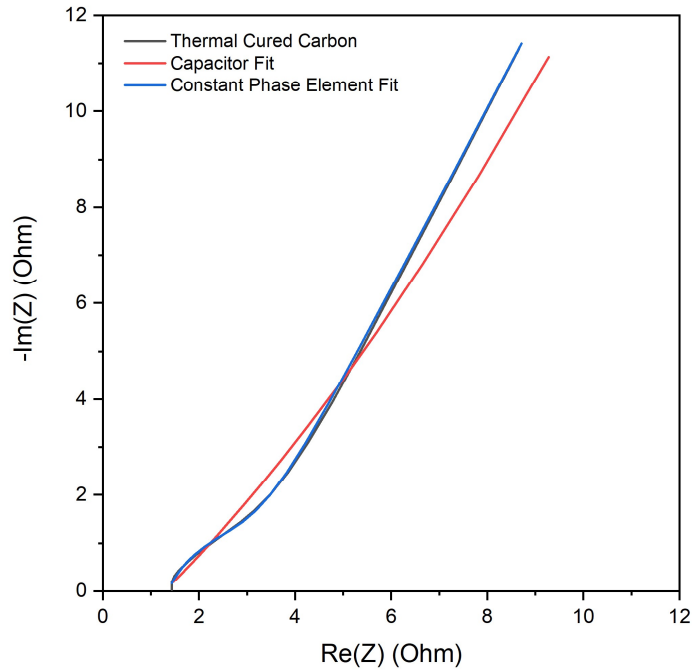
Figure 46. High frequency part of the thermal cured glassy carbon EIS spectrum.

From figure 46, the high frequency end of the impedance spectrum, it's observed that for the thermal cured carbon has a small ohmic internal resistance in the electrolyte, from table 4 we know this internal resistance is 1.33Ω. The start of a semi-circle shape is observed in the high frequency part of the thermal cured carbon spectrum, attributed to a resistor and capacitor parallel network. This semi-circle is not completed however, and it quickly transitions into a 45-degree linear function as the frequency decreases, indicating a low charge transfer resistance and is an indicator of double layer capacitance in the system. The 45-degree linear plot at the lower end of the frequency spectrum is an indicator that the material has diffusional impedance, also known as Warburg impedance. The EIS data from the photonic cured carbon in figure 47 and 48 shows a better-defined semi-circle at high frequency, but in this case it's also not a complete semi-circle and transitions early into the 45-degree linear function. The overall shape of the EIS data for both the thermal and photonic cured samples are similar, start of a semi-circle transitioning into 45-degree linear plot. The same Randles circuit proves to be a good approximation for both carbon's EIS data. Although the Randles circuit with the constant phase element is a closer fit, the circuit with the capacitor is a close enough approximation to get an estimate of the material specific capacitance without having to rely on further simulated mathematics.

Table 4: Thermal and photonic cured carbon EIS fitted data analysis by fitting the previously discussed Randles circuit as a model to the acquired data.

	Thermal Cured Carbon	Photonic Cured Carbon
Internal Resistance (R_{in}) [Ω]	1.33	1.67
Carbon Layer Resistance (R^1) [Ω]	361.1	358.0
Steel substrate Resistance (R^2) [Ω]	75.5	60.88
Carbon Layer Capacitance (C_{dl}^1) [mF]	4.84	7.16
Normalized Carbon Layer Capacitance (C_{dl}^1) [mF/cm^2]	2.42	2.39

The BioLogic potentiostat software extracts theoretical values for the approximated Randall circuit component applied to model the recorded data. In table 4 the resistances and the double layer capacitance of the carbon layers is estimated using the best fitting equivalent circuit data set. The capacitance obtained by EIS is the differential capacitance, which is an instantaneous value, unlike the integral capacitance obtained from the galvanostatic charge/discharge method (in the next subchapter) which an average value. The recorded EIS data is not normalized to the exposed carbon area during testing so for a better comparison of material capacitance the values from table 4 must be normalized to per square centimetre, yielding a capacitance of 2.42mF/cm^2 for the thermal cured carbon and a 2.39mF/cm^2 for the photonic cured carbon. This again demonstrating the similarity between the thermal and photonic cured carbon materials.
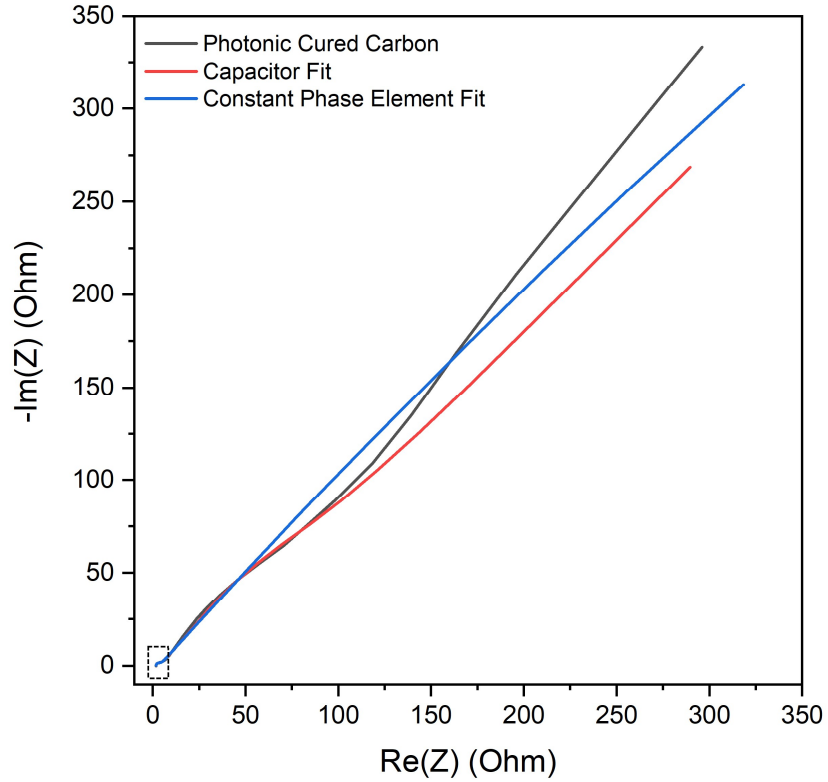
Figure 47. Electrochemical impedance spectroscopy of bar coated photonic cured glassy carbon on stainless steel substrate. The dashed-line box highlights the high-frequency end of the recorded data which is shown in figure 48.
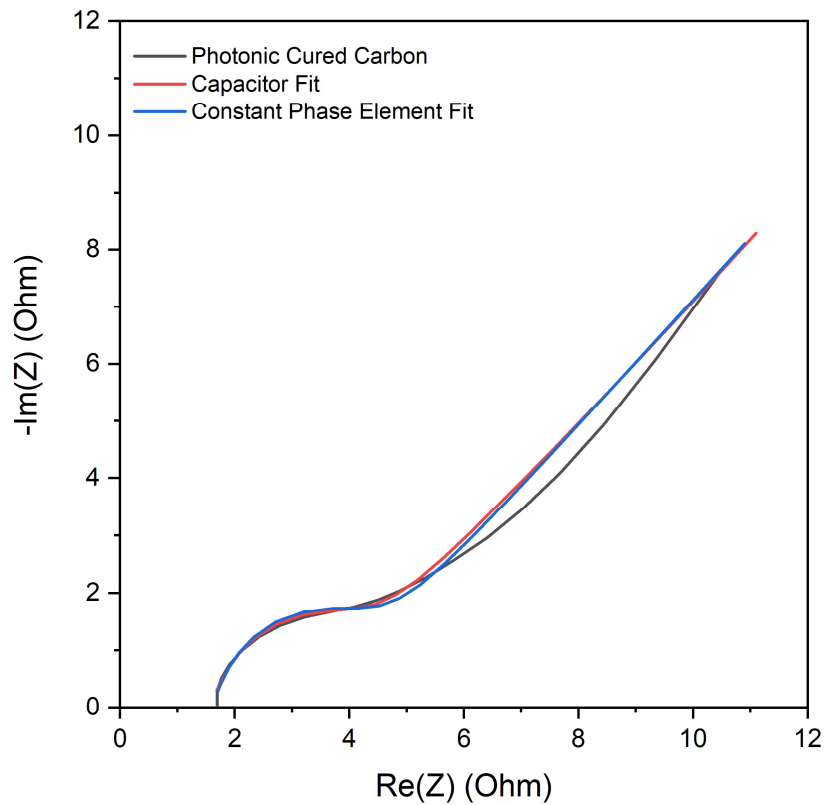
Figure 48. High frequency part of the photonic cured glassy carbon EIS spectrum.

To compare the two carbon coatings directly without any fitting of equivalent circuit data the photonic cured carbon and the photonic cured carbon Nyquist and Bode plots are compared below in figure 76 and 77. It's observed that the two carbon coatings have resistances of the same order of magnitude with the photonic cured carbon having a marginally higher resistance compared to the thermal cured carbon.
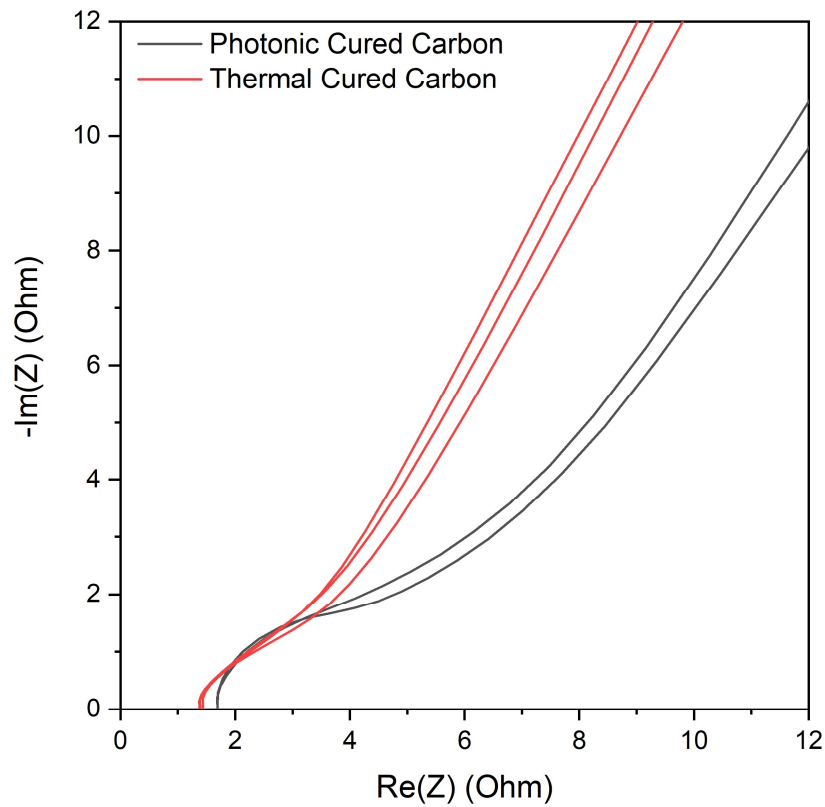
Figure 76. Nyquist plot comparison between photonic and thermal cured carbon in the high frequency part of the spectrum.
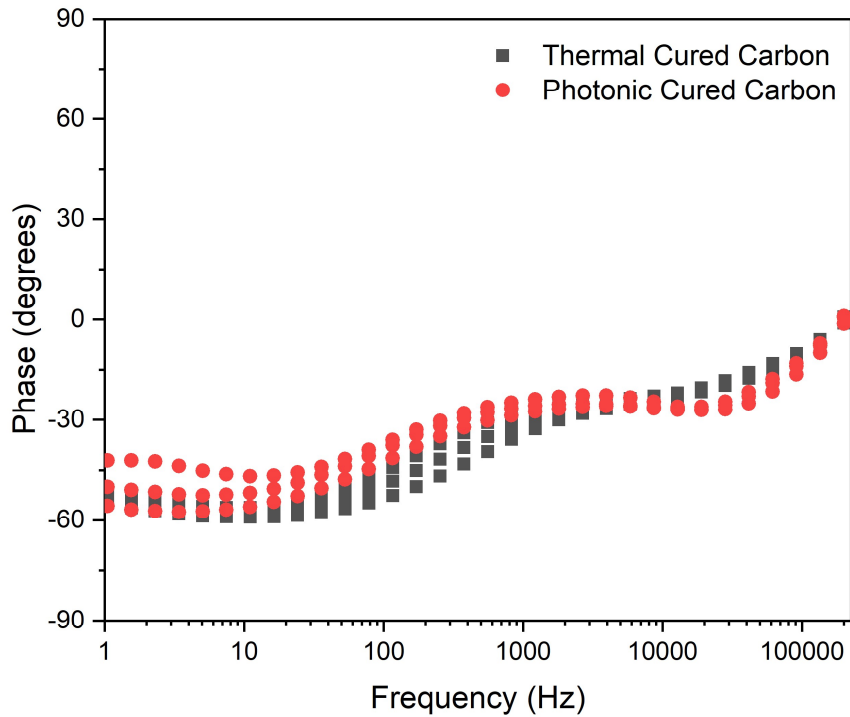
Figure 77. Bode plot comparing the thermal and photonic cured carbon data.

5.5 Galvanostatic Charge/Discharge

Galvanostatic charging and discharging (GCD) is a method where a cell is forced to reach an upper and lower potential by exposing it to a constant absolute current but changing the direction of flow once it's reached the set potential boundary. During charging and discharging using a chosen current, the voltage is measured against time. An array of currents is chosen so that a range of current densities may be studied, this results in the ability to calculate the equivalent series resistance, specific capacitance and the coulombic efficiency of the studied system.
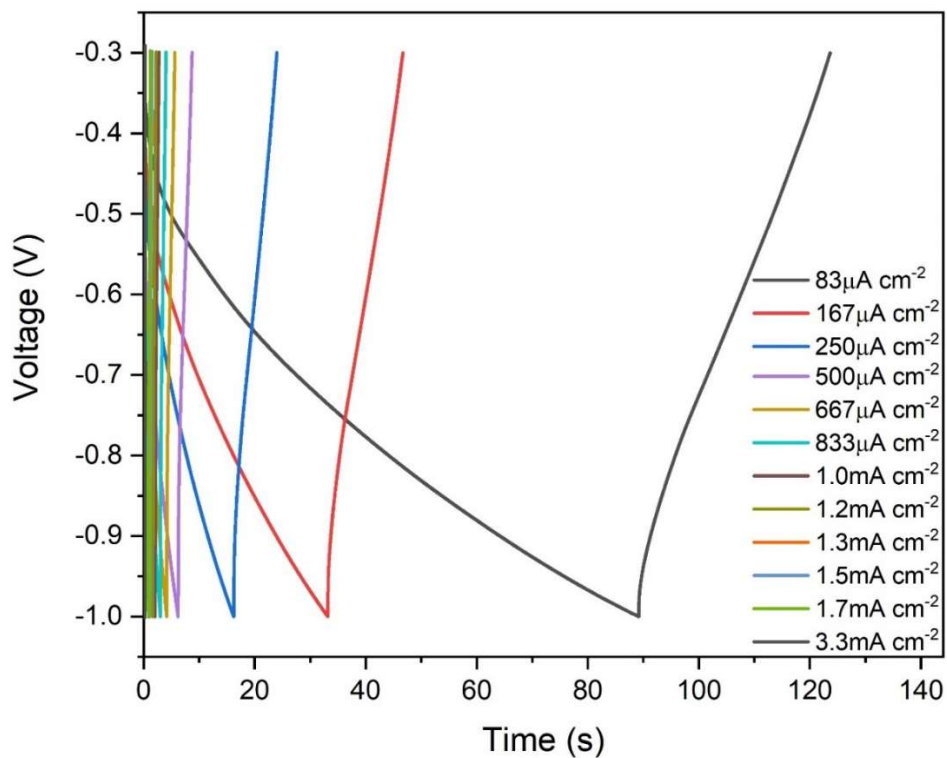
Figure 49. Galvanostatic charge/discharge curves of photonic cured carbon electrode under an array of different current densities.
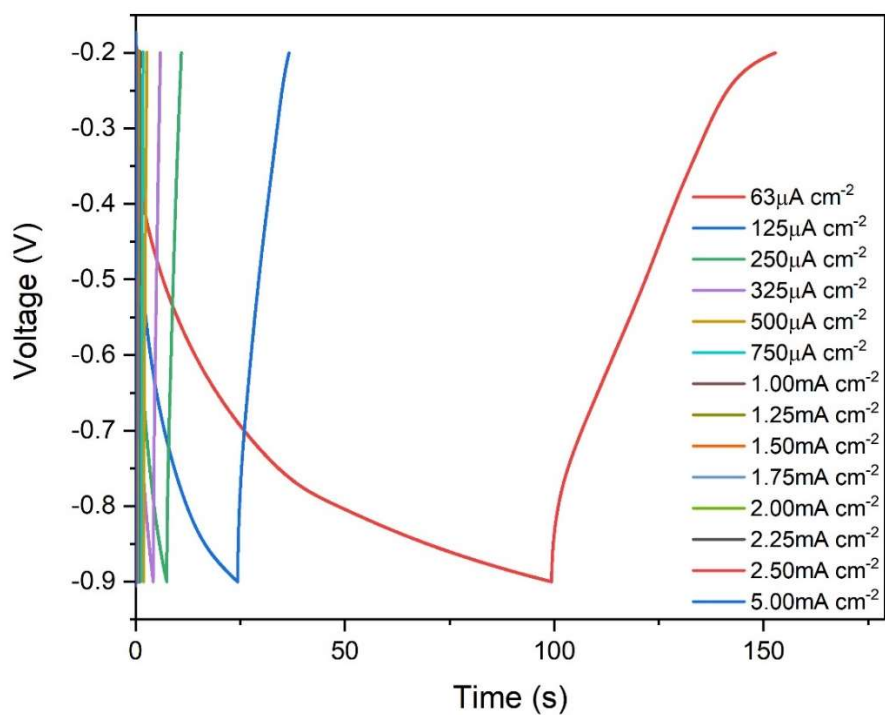
Figure 50. Galvanostatic charge/discharge curves of thermal cured carbon electrode under an array of different current densities.

The charge and discharge curves, change in voltage with time, for an array of different current densities are presented in figures 49 and 50 for the photonic cured carbon and the thermal cured carbon electrodes respectively. The behaviour of the two carbon coatings, photonic and thermal cured carbon, as anode material during a charge/discharge cycle is similar to each other. The photonic cured carbon voltage-time relationship is slightly more linear than that of the thermal cured carbon, although the time it takes to charge and discharge is practically identical per current density.

At the point where the GCD changes from discharge to charge a small instantaneous jump in voltage is observed, this is known as the voltage drop (ΔV_{CD}). The voltage drop can have many contributing factors such as the potential redistribution effect, charge redistribution effect, electrolyte starvation effect and memory effect (97–100). This voltage drop is directly related to the equivalent series resistance (ESR) and the current density. The total measured voltage is equal to the sum of the voltage of the equivalent series resistance and the voltage across the double layer capacitor part of the system. Capacitors store energy and thus it takes time for this energy to dissipate, thus at the point of changing from charge to discharge or vice versa, the voltage across the capacitor is momentarily in the opposite direction to the voltage across the equivalent series resistance. Hence around the point where the system changes from charge to discharge, it's found the total measured voltage during charging is equal to

$$V_{measured}^{charge} = IR_{ESR} + V_c$$

where the ESR voltage is IR_{ESR} and the capacitor voltage is V_c, while during discharge we have the total measured voltage equal to

$$V_{measured}^{discharge} = -IR_{ESR} + V_c$$

where the voltages are in opposite directions. And therefore, the difference between the measured voltages at the point of current change is equal to the voltage drop, which is defined by

$$\Delta V_{CD} = IR_{ESR} + V_c - (V_c - IR_{ESR})$$

$$\Delta V_{CD} = 2IR_{ESR}$$
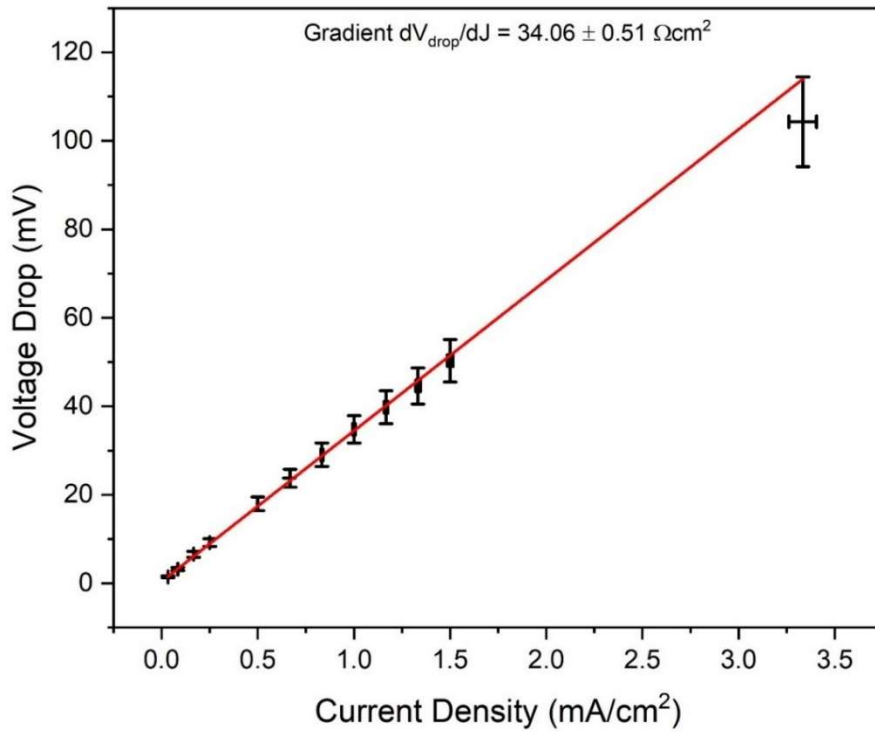
Figure 51. Photonic cured carbon galvanostatic charge/discharge voltage drop plotted against current density. The gradient is equal to 2R where R is equivalent series resistance.
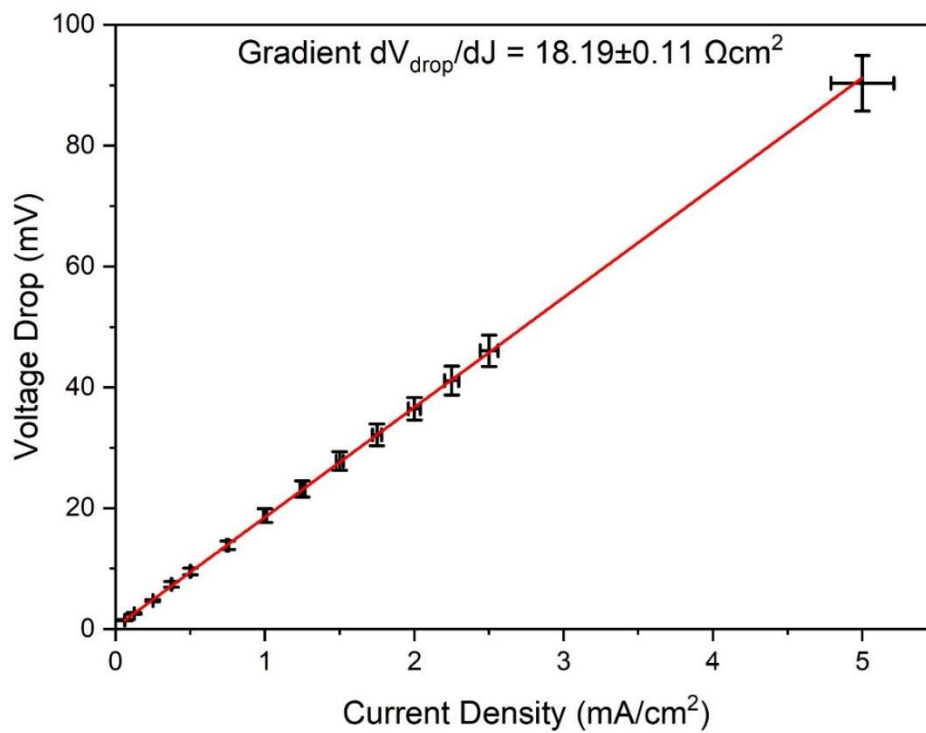
Figure 52. Thermal Cured galvanostatic charge/discharge voltage drop plotted against current density. The gradient is equal to 2R where R is equivalent series resistance.

Comparing the data from figures 51 and 52 its observed that the equivalent series resistance of photonic cured carbon is larger than that of the thermal cured carbon but is still of comparable value, as both resistances are of the same order of magnitude. The equivalent series resistances of photonic and thermal cured carbon are calculated to be 17.03 ± 0.26 Ωcm^2 and 9.09 ± 0.06 Ωcm^2 respectively. This equivalent series resistance could be due to the difference in carbon structure on the coating surface as determined earlier by the XPS data in chapter 4.2.3, in this chapter the D-parameter data shows that in the top nanometres of the carbon layer the photonic cured carbon has partial sp^2 and sp^3 bonded carbon structure, whereas the thermal cured carbon is exclusively sp^2 bonder carbon which is the more electrically conductive bond.

In figures 53 and 54 the integral capacitance (average capacitance) of the photonic cured carbon and the thermal cured carbon are plotted against current density. Both the charge and discharge capacities of the photonic cured sample are considerable larger than those of the thermal cured carbon working electrode. Comparing this integral capacitance to the differential capacitance values obtain in the previous EIS subchapter, observe that both methods produce values in the mF/cm^2 range as is shown in table 5. This shows the similarity between the two carbon thin films and that both methods of obtaining capacitances yield similar data. In literature, Sharma *et al.* (70) reports the use of porous glassy carbon electrodes for supercapacitor applications with capacities ranging between $3.14mF/cm^2$ and $4.28mF/cm^2$, which is consistent with the findings of this research displayed in table 5.

Table 5: Comparison of integral and differential capacitances obtained using galvanostatic charge/discharge and EIS methods respectively.

Specific Integral Capacitance (GCD)		Specific Differential Capacitance (EIS)	
Thermal Cured Carbon	Photonic Cured Carbon	Thermal Cured Carbon	Photonic Cured Carbon
$0.49 - 8.94$ mF/cm^2	$1.27 - 10.68$ mF/cm^2	2.42 mF/cm^2	2.39 mF/cm^2
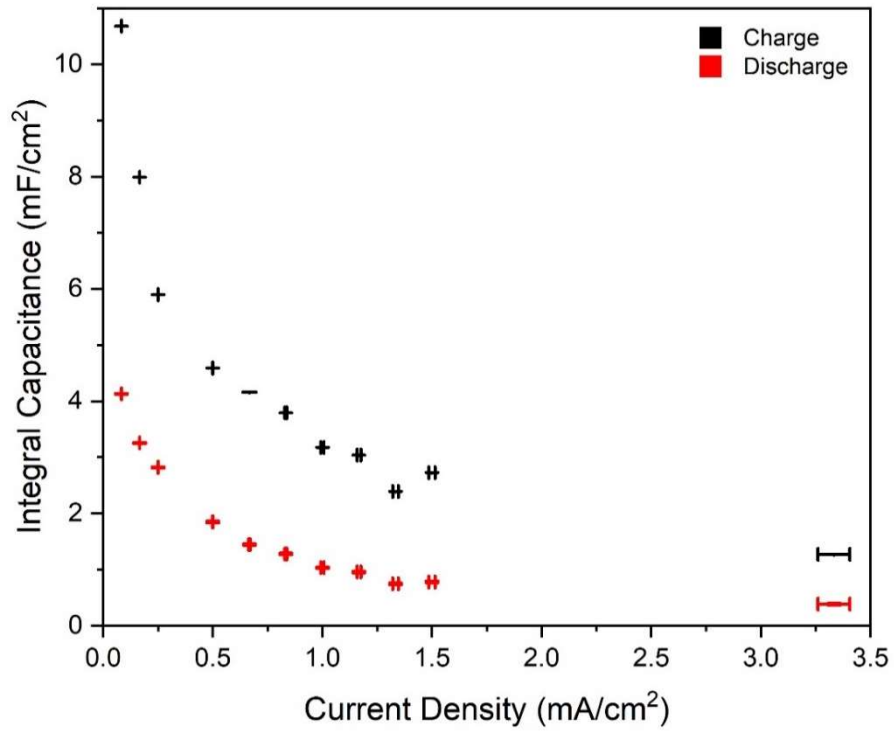
Figure 53. Integral capacitance as a function of current density of the photonic cured carbon working electrode in 0.5M aqueous sodium sulphate solution.
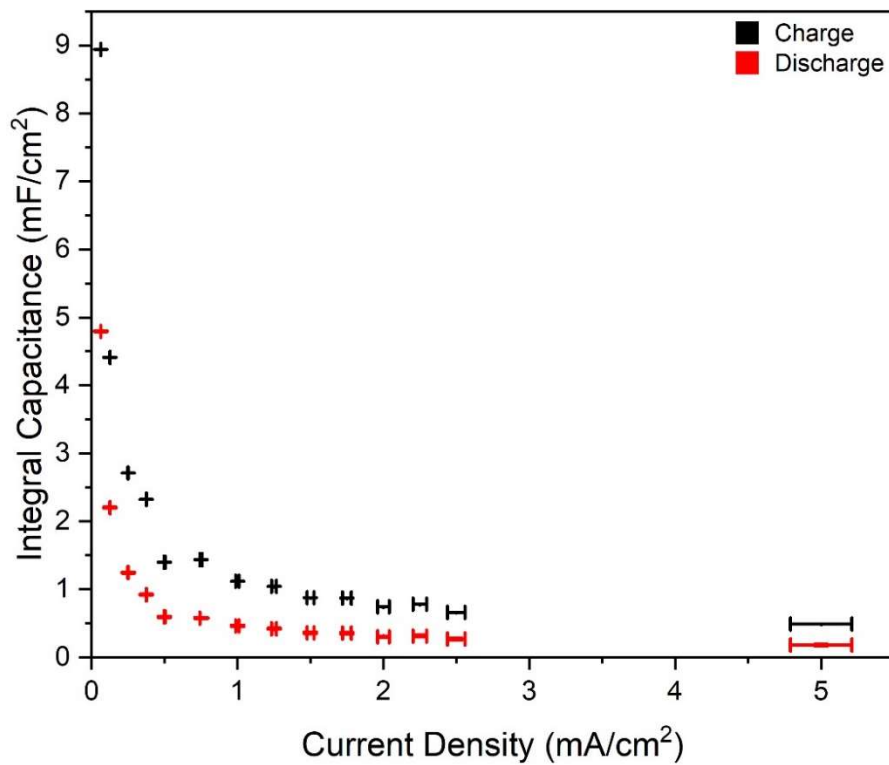
Figure 54. Integral capacitance as a function of current density of the thermal cured carbon working electrode in 0.5M aqueous sodium sulphate solution.

Although the integral capacitance of the photonic cured carbon was larger than that of the thermal cured carbon, the Coulombic efficiency of the thermal cured carbon is more stable at higher current densities as is observed from the data presented in figure 55. In figure 55 the coloumbic efficiencies of the two carbon coatings are plotted against the current density. It's clear that the thermal cured carbon shows to have a considerably higher coulombic efficiency than the photonic cured carbon as the thermal cured carbon stabilizes around 45% with increasing current density whereas the photonic cured carbon appears to stabilize around 32% towards the higher explored current densities. Extra data collection of further current densities could improve the accuracy of the determines coulombic efficiencies but from this data the thermal cured carbon clearly outperforms the photonic cured carbon.
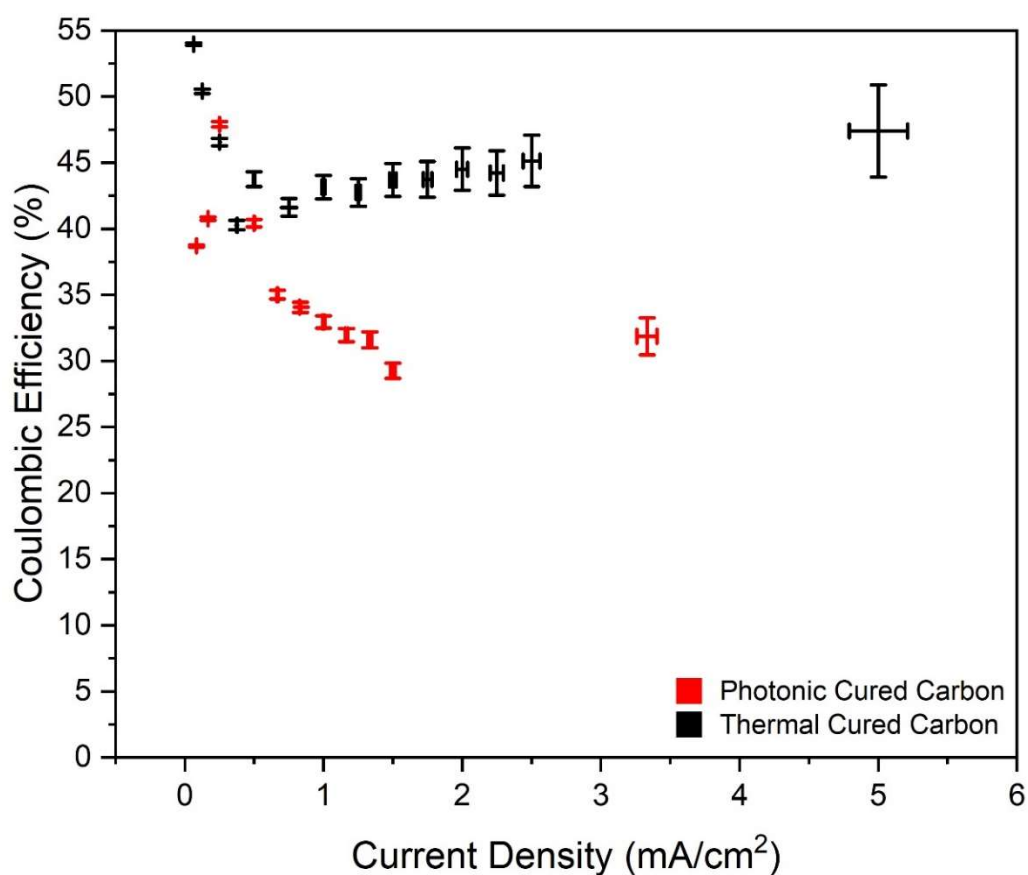
Figure 55. Coulombic efficiency of the thermal (black) and photonic (red) cured glassy carbon thin films as electrode active materials.

5.6 Chapter Closure

Electrochemical behaviour and performance are investigated with the thermal and photonic cured carbon thin films as working electrodes in a half-cell environment, both materials were tested in 0.5M Na_2SO_4 solution against a Ag/AgCl reference electrode and a platinum counter electrode. Techniques such as cyclic voltammetry, electrochemical impedance spectroscopy and galvanostatic charge/discharge were utilized to compare the two materials.

The CV curves consisted of similar shapes over essentially the same voltage window thus demonstrating the similarity between the thermal and photonic cured carbon in terms of electrochemical behaviour. The CV data was manipulated using Dunn's method, this allows us to distinguish whether a material is dominated by surface interactions or by diffusions interactions in an electrochemical cell environment, both thermal and photonic cured carbon are shown to be dominated by diffusion-controlled processes.

The internal resistance and the specific differential capacitances of the thermal and photonic cured carbons are calculated from the EIS data by fitting a Randles circuit model that describes the mechanics of the printed carbon layer on a stainless-steel substrate. The specific differential capacitances were measured to be 2.42 mF/cm^2 and 2.39 mF/cm^2 for the thermal cured and photonic cured carbon respectively.

The GCD data is used to calculate the ESR and the specific integral capacitance of the photonic and thermal cured carbons. The equivalent series resistances of photonic and thermal cured carbon are calculated to be 17.03 ± 0.26 Ωcm^2 and 9.09 ± 0.06 Ωcm^2 respectively. Across a range of current densities (0.06 – 5.00mA/cm^2), the specific integral capacitances were measured to be 0.49 – 8.94 mF/cm^2 and 1.27 – 10.68 mF/cm^2 for the thermal and photonic cured carbons respectively.

Sharma *et al.* (70) reports the use of porous glassy carbon manufactured using the same type of phenol formaldehyde precursor, carbonized in inert atmosphere at 900°C. These porous glassy carbon electrodes yield a specific capacitance of 3.14mF/cm^2 to 4.28mF/cm^2. These results are comparable to the findings for the capacitance of glassy carbon thin films in this chapter, for both the thermal and photonic cured carbon.

This chapter demonstrates an equivalence in performance between the two materials as glassy carbon electrodes by way of electrochemical testing.

Chapter 6: Glassy Carbon in Printed Electronics and Sensors

6.1 Introduction

In this chapter the potential application of glassy carbon into printed electronics were explored. Screen printing was used to deposit patterns of the phenol formaldehyde precursor on a non-conductive ceramic substrate. Conventional thermal curing was adopted for the conversion into glassy carbon (photonic curing was not tested following malfunction of the equipment). Using screen printing as the deposition method for glassy carbon thin films broadens the potential applications of the material as the geometries of the printed structure are completely customizable. In this work, glassy carbon conductive tracks were made to explore its use in printed electronics and temperature sensors and glassy carbon interdigitated structures were investigated as salinity sensors. Showing the viability of screen-printing the precursor and carbonizing it after printing would encourage future research into screen printing the precursor on flexible, temperature sensitive substrates and using the photonic curing method to produce glassy carbon tracks on flexible substrates.

6.2: Screen Printing Glassy Carbon

Screen printing was selected as printing method as commonly adopted printing technology in printed electronics and its suitability to the resin viscosity. In view of the health hazard linked to the resin, printing had to be performed in a fume cupboard, by hand, while wearing protective equipment. The ability of screen printing to control deposit primarily through the mesh selection was therefore important for reproducibility. In this section the screen design, print results and layer thicknesses are discussed.
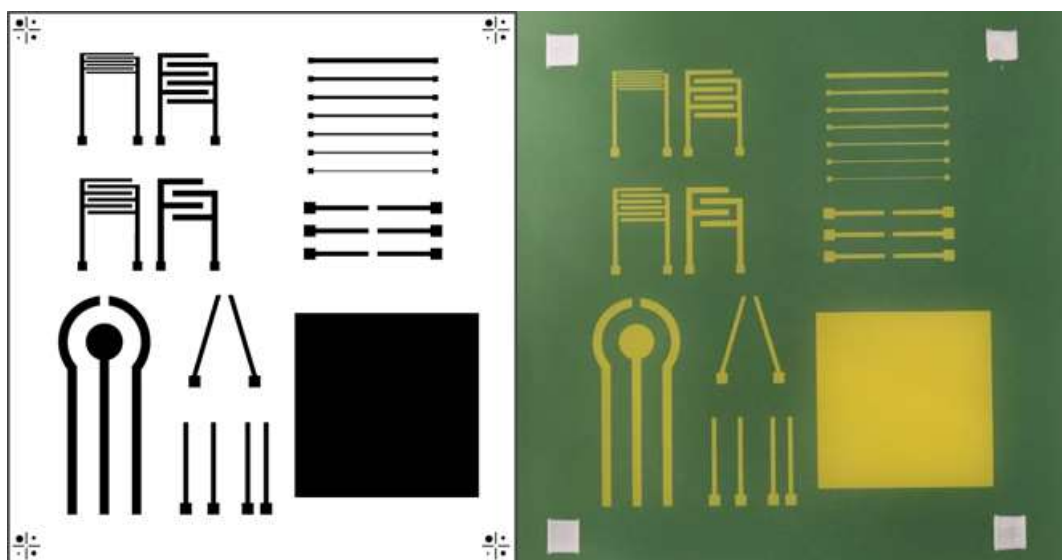
Figure 56. Screen template design made in Adobe Illustrator on the left. Screen manufactured by MCI Precision Screens with aperture of 13μm wet deposition on the right. The corner markings on the screen are 11x12cm in width and height respectively.

The screen in figure 56 features designs for six experiments. The 40 by 40mm square on the bottom right can be used to find the sheet resistance of glassy carbon followed by a long-term exposure to a salt solution to study the conductivity deterioration under those conditions. Printed lines on the top right can be used to study the line conductivity and to find the contact resistance glassy carbon. The parallel tracks in the centre bottom- and in-line tracks in the centre right can be used to study the materials ability to be soldered to devices such as LEDs. The intercalated fingers in the top left can be used to study the ability of glassy carbon to be used as a salinity sensor. The three-electrode setup on the bottom left may be used as a biosensor.

A 77/55 mesh of theoretical 13μm wet deposition was chosen to mimic the previously successful glassy carbon conversion with bar coating using 12μm theoretical wet deposition. The screen printing was done by hand to minimize contamination of the toxic precursor resin which deteriorates the print quality compared to using a screen-printing machine, an example of the hand screen printed precursor on alumina substrate is seen in figure 57. Following the screen printing, the resin was thermally carbonized following methods described in section 4.3, the resultant carbonized product is seen in figure 58.
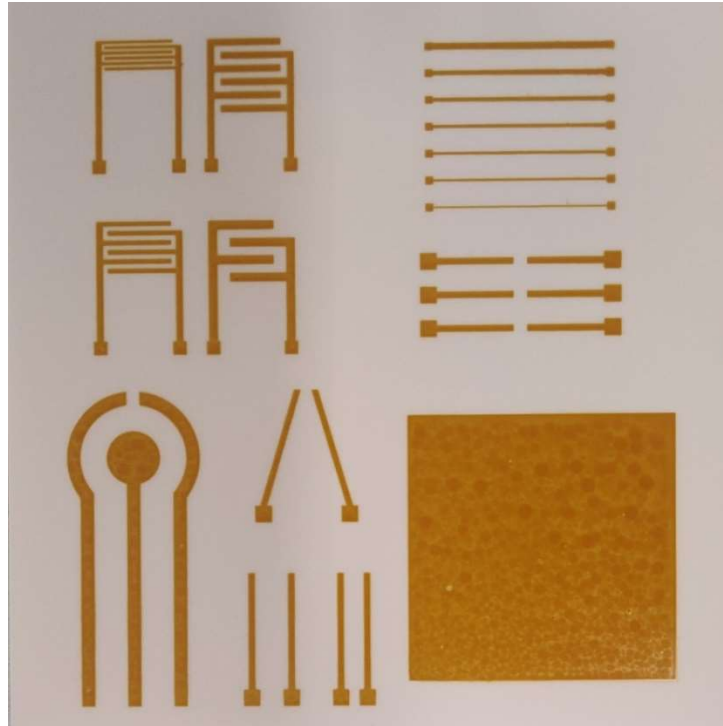
Figure 57. Screen printed phenol formaldehyde precursor using 77/55 mesh with a theoretical wet deposition thickness of 13µm.
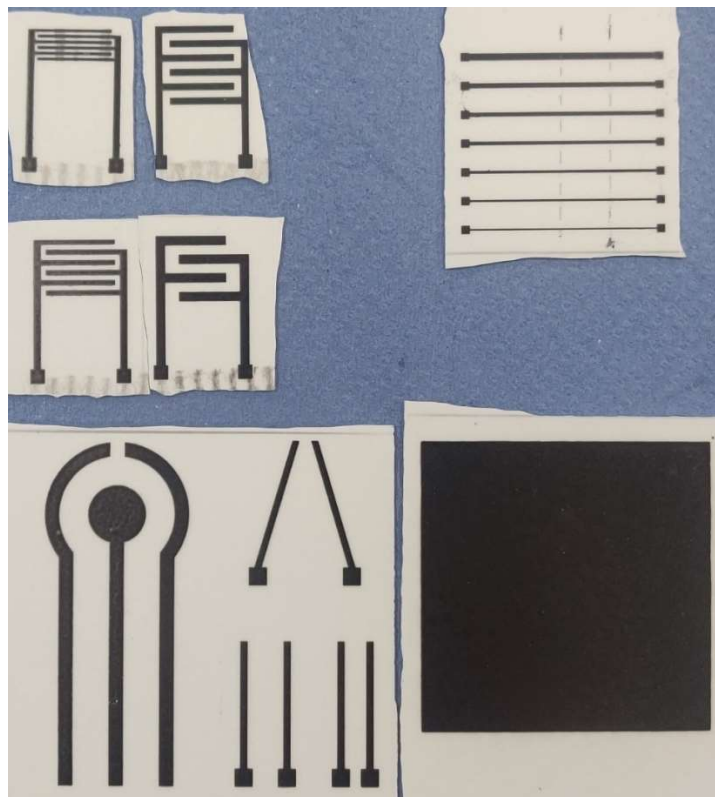
Figure 58. Thermal carbonised screen-printed samples from figure 57. Compilation of pictures as the original print on alumina must be cut to fit the tube furnace for carbonization.

Using stylus profilometry on a 40x40mm printed square of the cured phenol formaldehyde precursor before carbonization an edge layer thickness of 4.22±0.45µm is recorded across 5 measurements. Stylus profilometry was chosen for surface roughness, layer thickness and line width measurements on the alumina substrate because any optical methods wouldn't work due to the colour and pore geometry of the alumina substrate. Assuming the screen deposits its theoretical wet layer of 13µm, the curing process of the phenol formaldehyde precursor layer thickness retention of 32.5%. The same sample was studied after carbonization and thus converted to glassy carbon, a layer thickness of 3.35±0.37µm was measured across 5 measurements. Thus from deposited precursor to final glassy carbon the layer thickness retention is 25.7% and from cured precursor to post-carbonization is 79.3%. The measured percentage error is consistent between the printed precursor and the glassy carbon post-carbonization at 10.7% for the cured precursor and 11.1% for the glassy carbon layer.

Table 6: Screen print quality control, design printed line widths compared to measured line widths, indicated uncertainty is the sample standard deviation in the average presented value. N=6.

Designed Line Width [mm]	Measured Line Width [mm]
0.2	0.204 ± 0.007
0.3	0.288 ± 0.012
0.4	0.365 ± 0.016
0.5	0.460 ± 0.009
0.6	0.577 ± 0.016
0.7	0.654 ± 0.018
1.0	0.948 ± 0.014

Table 7: Screen print quality control, design printed interdigitated electrodes. Displayed uncertainties are sample standard deviations calculated using an average over 5 measurements.

N=5	Designed Line Width [mm]	Measured Line Width [mm]
Size 1	0.4	0.396 ± 0.013
Size 2	0.7	0.606 ± 0.017
Size 3	1.0	0.992 ± 0.015
Size 4	1.3	1.287 ± 0.007

From the line width measurements in table 6 and 7 it's observed that all printed line widths approach their theoretical widths but are always just under the theoretical width on average. From the surface roughness data presented in table 8, the difference between the glassy carbon surfaces produced using hand screen printing and bar coating quantified. The screen-printed glassy carbon surface yields approximately twice the surface roughness of the bar coated glassy carbon surface.

Table 8: Screen printed glassy carbon surface roughness measurements using white light interferometry. Comparison to bar coated glassy carbon. Displayed uncertainties are sample standard deviations calculated using an average over 6 measurements.

N=6	Fresh Screen-Printed Glassy Carbon Surface Roughness, Sa [nm]	Bar Coated Glassy carbon Surface Roughness, Sa [nm]
Sample 1	247 ± 15	
Sample 2	267 ± 27	137 ± 13
Sample 3	258 ± 22	

6.3: Testing Glassy Carbon Electrical Performance

The electrical performance of glassy carbon was then studied in terms of contact resistance, line conductivity, sheet resistance and its ability to be combined with devices to complete a circuit.

6.3.1 Printed line resistance

To measure the contact resistance the resistance of the glassy carbon printed lines is measured at full, half and quarter length which is 27.2mm, 13.6mm and 6.8mm respectively. These measurements are taken with a Keithley 2100 multimeter using a moving average filter across 100 measurements. These measurements are taken across 3 samples where each sample consists of 6 printed lines of different widths. Plotting the measured resistance against the length of the conductive line at 3 different lengths yields the ability to extrapolate a line to intersect with the resistance axis to give an estimation of the contact resistance between the glassy carbon and the measuring prongs. The measurement setup is shown in figure 59. where the prongs are held in place with stands and clamps to ensure no movement in the connection whilst the measurements are taken.
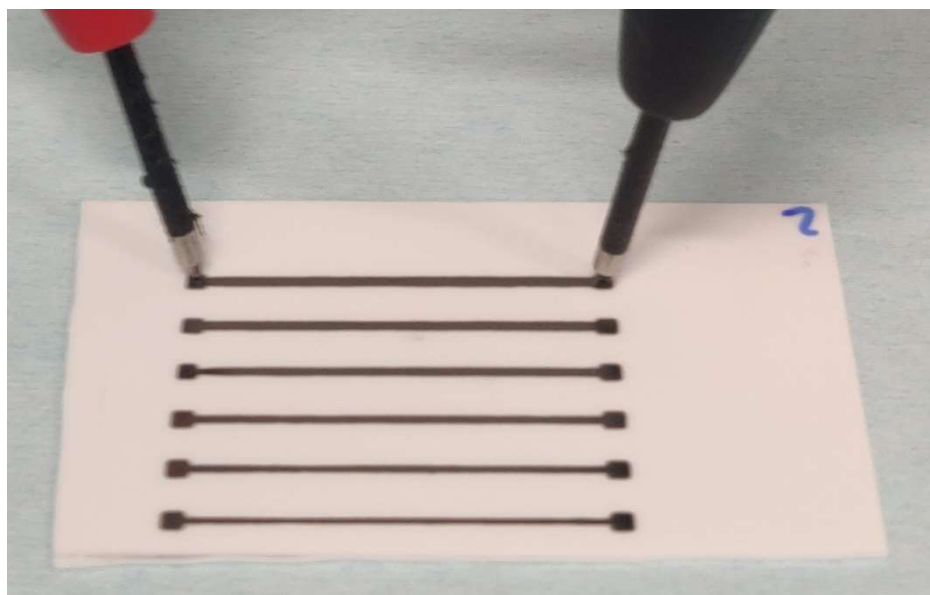
Figure 59. 2-probe setup for resistance measurements along printed glassy carbon lines.

In figures 60 to 62 the measured resistance in the glassy carbon lines is plotted against the length of the glassy carbon line. A linear extrapolation is made by plotting a linear fit line between the 3 data points of each line width. The Y-intercept of each extrapolated line gives an estimation of the contact resistance of the glassy carbon material.
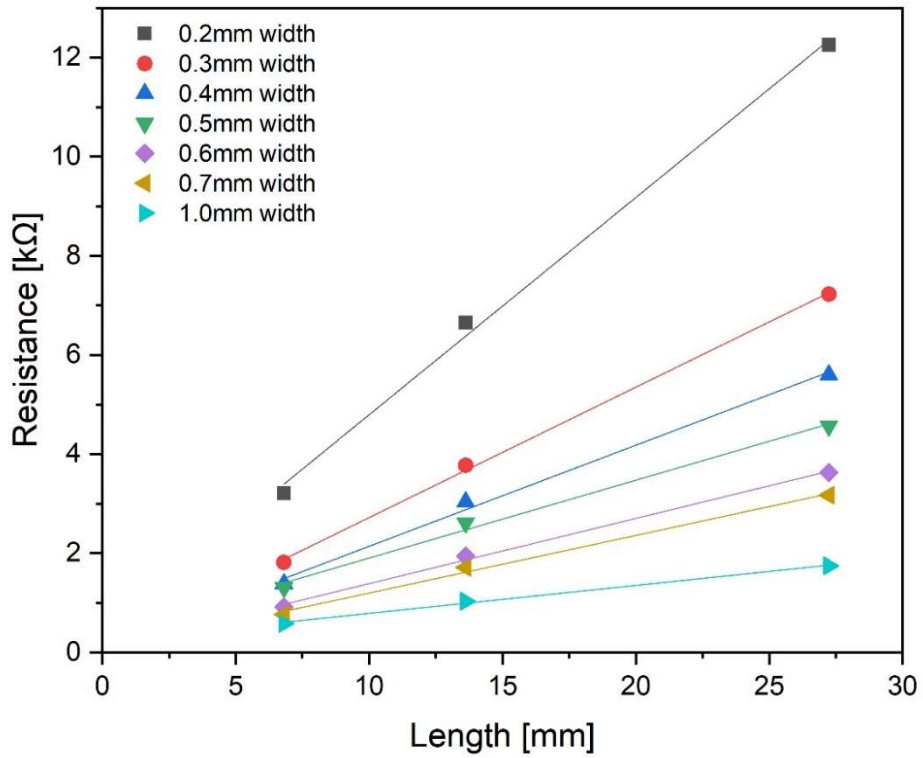
Figure 60. Measured resistance using the 2-point probe as a function of the length of glassy carbon lines plot for all the lines of different widths of sample 1.
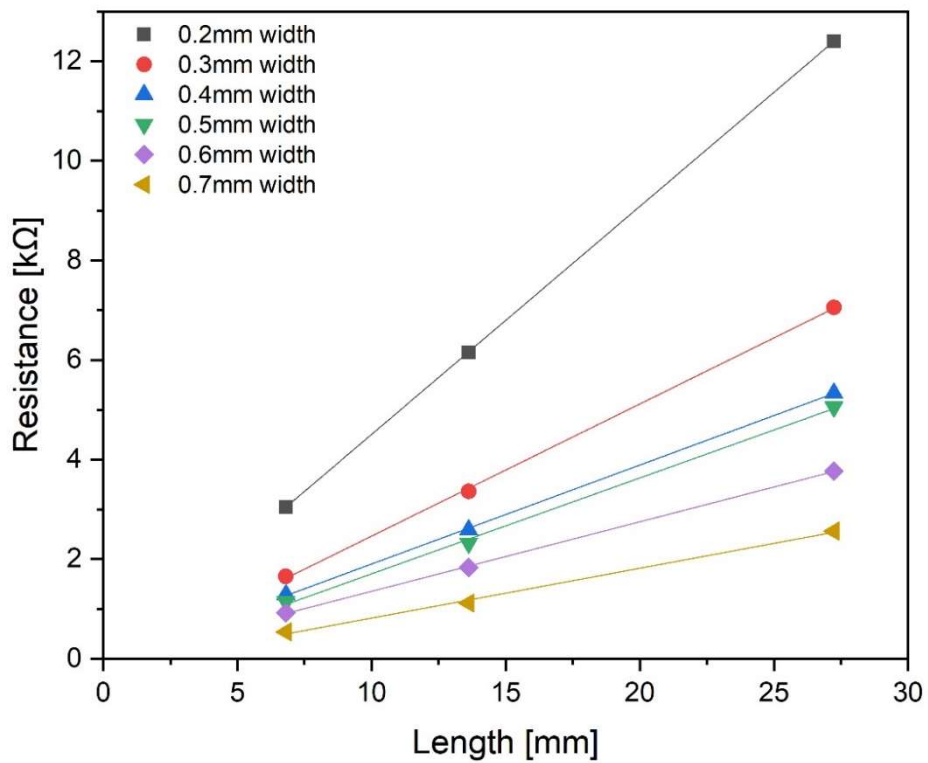
Figure 61. Measured resistance using the 2-point probe as a function of the length of glassy carbon lines plot for all the lines of different widths of sample 2.
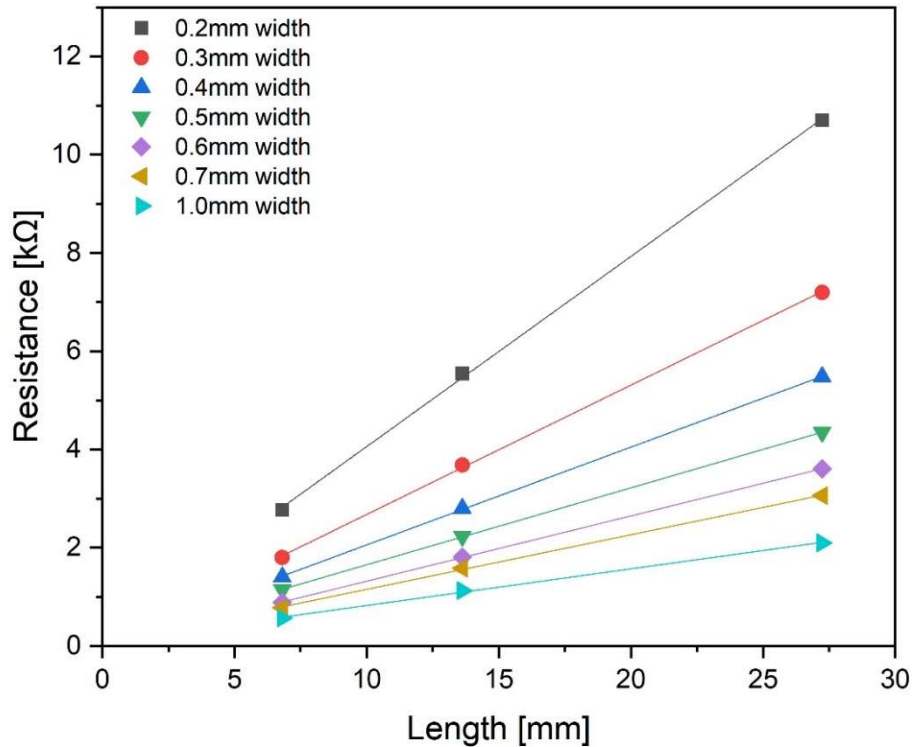
Figure 62. Measured resistance using the 2-point probe as a function of the length of glassy carbon lines plot for all the lines of different widths of sample 3.

Using the data from figures 60 to 62, it's found that the contact resistance of the glassy carbon printed lines, defined as the extrapolated y-intercept, is less than 300Ω for all samples. This contact resistance is therefore relatively minor to the following resistance printed line measurements.

6.3.2 Line Conductivity

The next logical step in analysing the electrical performance of printed glassy carbon is to study its electrical conductivity. In this subchapter the line conductivity is studied by using resistance measurements combined with geometric measurements of line length and the cross-sectional area of the printed lines.

Starting with the geometry of the printed lines, profilometry is used to measure the cross-sectional area and the length of the printed lines is measured using digital callipers. To ensure a reliable average and standard deviation 6 measurements are taken per printed line. Figure 63 is an example of a line cross section profile of a 1mm wide printed glassy carbon line recorded using a profilometer. In figure 63 a Gaussian line is used to approximate the shape of the printed line so that the area under the curve may be integrated to estimate the cross-sectional area of the printed line.
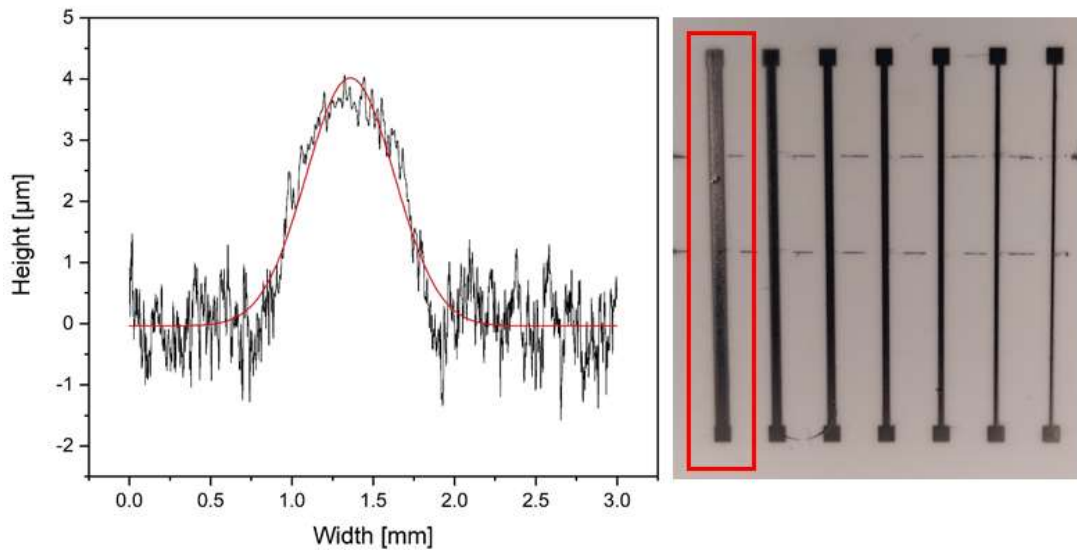
Figure 63. Profilometry profile of a 1mm wide printed glassy carbon line with a Gaussian fit in red on the left. On the right a picture of the glassy carbon printed lines with the 1mm wide line highlighted in red.

After fitting Gaussian approximations to the profilometer data, the curves are integrated to calculate the cross-sectional area of the printed lines. Due to the generates axes in figure 63 the calculated cross-sectional area of the is measured in units [μm*mm], these values were adjusted to units [m^2] to be displayed in table 9.

Table 9: Calculated cross-sectional areas of the printed glassy carbon lines using N=6 measurements per printed line for an average value and sample standard deviation.

Line Width [mm]	Calculated cross sectional area [$\times 10^{-10}$ m^2]
0.2	5.26 ± 0.60
0.3	7.43 ± 0.39
0.4	8.53 ± 0.77
0.5	13.87 ± 1.16
0.6	14.76 ± 1.15
0.7	18.55 ± 1.10
1.0	27.79 ± 3.37

Using these calculated cross-sectional areas from table 9, we employ Pouillet's law. Pouillet's law is a relationship between the line length, cross sectional area, resistance and resistivity of the conductive line given as

$$R = \rho \frac{l}{A}$$

Which may be rearranged to

$$\therefore \rho = R \frac{A}{l}$$

Where ρ is resistivity in [Ωm], R is resistance in [Ω], A is the cross-sectional area in [m^2] and l is the length of the line in [m]. Conductivity is defined as the inverse of the resistivity, thus we have

$$\sigma = \frac{1}{\rho}$$

To measure the resistance along the printed line a Keithley 2100 multimeter with two probes held in place by stands and clamps is used. A total of 3 samples with 7 printed glassy carbon lines each is analysed. Resistance measurements are taken with a moving average across 100 measurements. In table 10 the resistance measurements taken from the 3 chosen glassy carbon printed line samples are displayed. Sample 2 is missing the line of width 1mm hence no value for resistance, resistivity or conductivity was produced from that missing data point.

Table 10: Resistance measurements taken of glassy carbon printed lines of 7 different widths using 3 samples. Readings taken using a moving average over 100 measurements.

Line width [mm]	Sample 1: Resistance [kΩ]	Sample 2: Resistance [kΩ]	Sample 3: Resistance [kΩ]
1.0	2.005	-	2.051
0.7	3.001	2.467	2.908
0.6	3.434	3.634	3.464
0.5	4.296	4.893	4.100
0.4	5.360	5.226	5.195
0.3	6.936	6.825	6.883
0.2	11.976	11.989	10.336

With these data from table 10 an average resistivity and conductivity for the glassy carbon material can be calculated per sample. Due to the number of printed lines per sample the average and standard deviation is calculated from N=7 values for samples 1 & 3 and N=6 for sample 2. These average values with their accompanying standard deviations are displayed in table 11.

Table 11: Calculated average resistivity and conductivity per sample of screen-printed glassy carbon lines. Calculated using Pouillet's law.

N=7	Sample 1	Sample 2	Sample 3
Resistivity [$\times 10^{-4}$ Ωm]	1.93 ± 0.21	1.92 ± 0.33	1.86 ± 0.16
Conductivity [$\times 10^{3}$ S/m]	5.24 ± 0.57	5.34 ± 0.88	5.41 ± 0.49

Comparing the results from table 11 to literature, it's found that these resistivity and conductivity values are similar to those of graphite and carbon black based conductive inks (101), making glassy carbon printed lines a viable alternative to other carbon based conductive inks if there's an application requiring a more robust and/or chemically resistant conductive track. Resistivities of these inks are given in the range of 2.9×10^{-4} Ωm to 12.7×10^{-4} Ωm, thus the resistivity of glassy carbon lines is lower than that

of the mentioned conductive inks, demonstrating a similarity in performance compared to the best performing graphite and carbon black based conductive ink. Another graphite and carbon black based conductive ink reports 0.45×10^{-3} Ωm, which is factor 10 higher than the presented glassy carbon resistivity (102). Nano carbon inks derived by plasma processes best performer demonstrates a resistivity of 39×10^{-4} Ωm, which is factor 10 greater than the printed glassy carbon lines (103). Double walled carbon nanotube based inks investigated by Aziz *et al.* (104) demonstrate a conductivity of 3.6×10^{5} S/m, which is factor 100 higher than the conductivity of the printed glassy carbon lines, thus outperforming the glassy carbon.
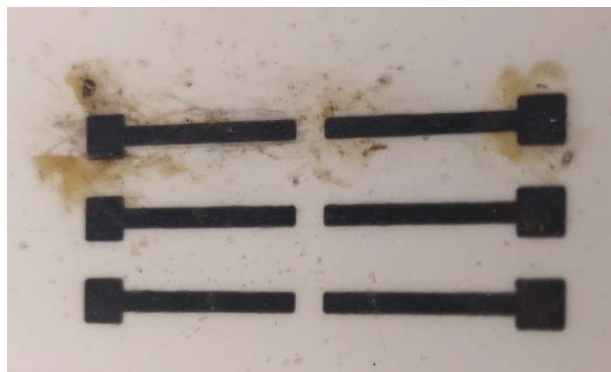
Figure 64. Picture of printed glassy carbon tracks stained by the flux of the soldering tin after a failed attempt at soldering wires to the glassy carbon surface.

To demonstrate the conductivity of the printed glassy carbon lines and its potential use as part of a circuit an attempt was made to solder wires and a device to the carbon layer which was unsuccessful. Figure 64 shows the flux from the soldering tin attaching itself to the alumina substrate but wouldn't adhere to the glassy carbon surface. The ability for the alumina substrate to disperse the heat from the soldering iron could be a factor into why soldering to the glassy carbon surface wasn't successful, hence another attempt was made to solder to the glassy carbon whilst being heated by a hotplate but to no avail.

Soldering, as a method to make an electrical connection, was replaced by making connections with a flexible silver paste made by the Gwent Group. This particular silver paste required curing at 120°C for 20 minutes. In figure 65 a picture demonstrates conductive wires attached to the poles of the glassy carbon tracks and an LED bridging the gap between the tracks. A set current and voltage of 30mA and 3.0V was applied to the LED and glassy carbon track circuit using a DC power supply. The result was the green LED lighting up as shown in figure 65.

Figure 65. Printed glassy carbon lines on alumina substrate. LED and metal wires installed on top of GC using silver paste. Induced current of 30mA with a 3.0V potential.

6.3.3 Sheet Resistance

In this subchapter the sheet resistance of printed glassy carbon squares of dimensions 40x40mm is studied to characterize the electrical performance of the printed glassy carbon material. The resistance across the surface of the printed glassy carbon measured using a four-point probe system where a small current is applied through the outer two poles and the voltage is measured through the inner two poles of the system, these 4 poles are seen in the right-hand image in figure 66. Using this measured resistance, the sheet resistance of the material is calculated using a correction factor which is determined by the ratio and geometry of the printed square relative to the poles. This sheet resistance may then be used to calculate the bulk conductivity and resistivity of the material when combined with film thickness measurements using a profilometer. These values are then compared to the values of conductivity and resistivity calculated in the previous subchapter studying printed glassy carbon lines.
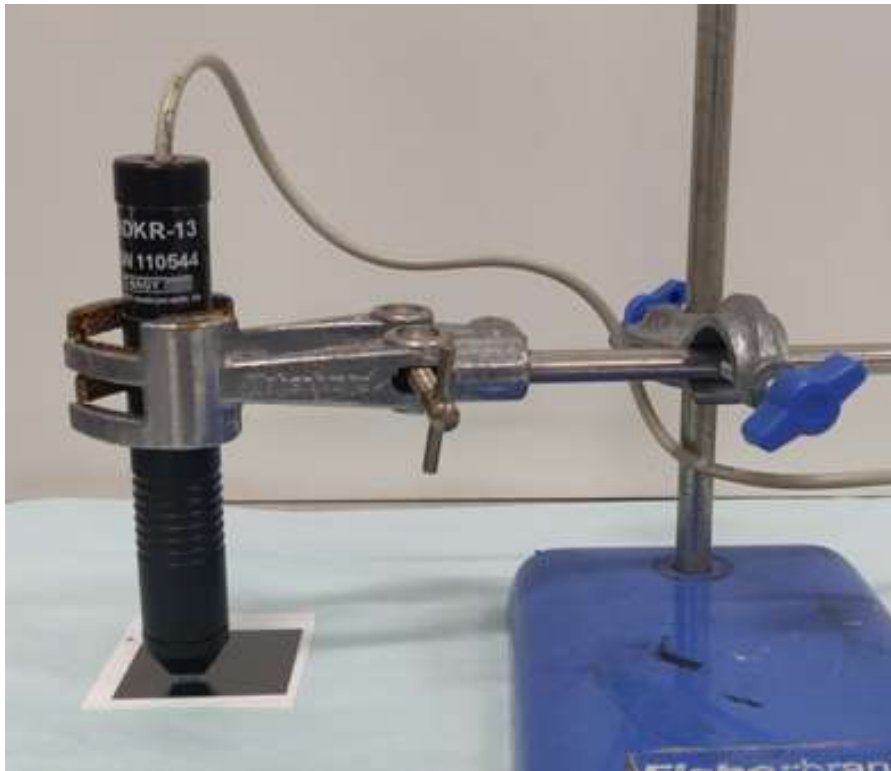
Figure 66. Four-point probe setup to measure sheet resistance of glassy carbon printed squares (40x40mm). Probe is held in place by stand and clamps, the height of the probe is set using the clamps for consistency in pressure between measurements.

The thickness of these printed squares is measured using a KLA Tencor D-600 profilometer. In figure 67 you see an example of a profilometry measurement taken from sample 3. All 3 printed glassy carbon squares were measured 16 times for film thickness, 4 measurements per side, allowing for a reliable average and standard deviation to be calculated.
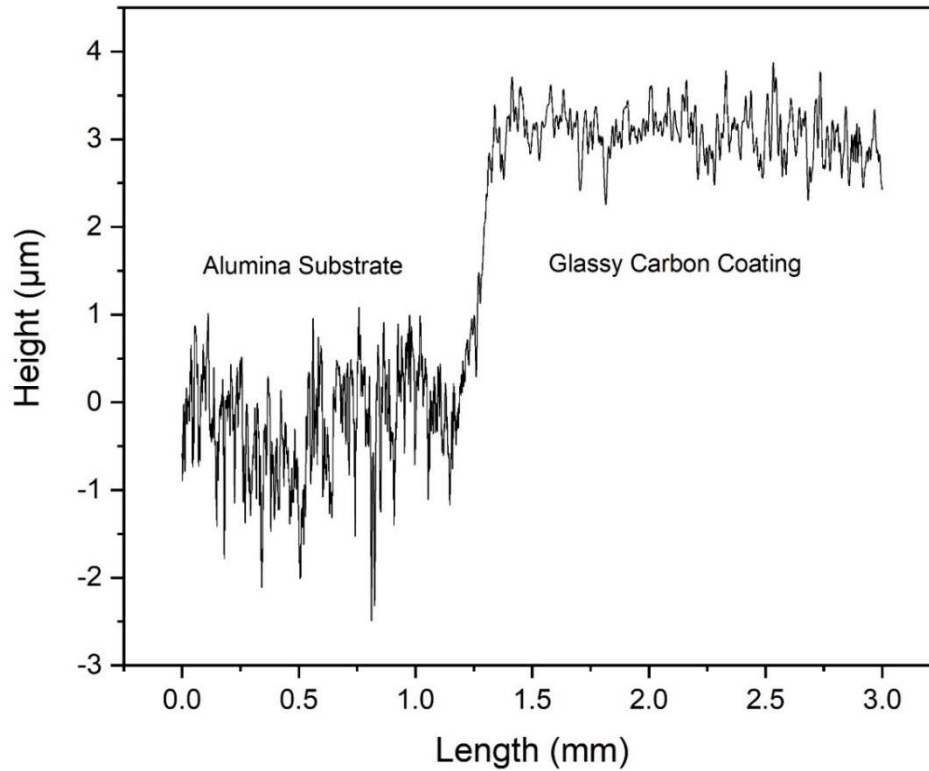
Figure 67. Profilometry of printed 40x40mm glassy carbon square demonstrating the step height which is quantified in table 12.

In table 12 the layer thickness of the glassy carbon printed squares on a ceramic alumina substrate are presented. The values are taken by calculating an average from 16 measured values, 4 per side of a square. These measurements were taken using a profilometer with a scan rate of 0.05mm/s and a stylus force of 10mg.

Table 12: Average layer thickness of 40x40mm square screen-printed glassy carbon with accompanying sample standard deviation values taken from 16 profilometry measured taken per sample.

N = 16	Layer Thickness [μm]
Sample 1	3.30 ± 0.64
Sample 2	3.35 ± 0.43
Sample 3	3.48 ± 0.39

Using a four-point probe system we can find the sheet resistance of printed glassy carbon. A printed square of 40x40mm is used as the measured sample. 3 samples are analysed. In

table 13 the raw data taken from the multimeter in combination with a 4 point probe is shown. Samples 1 and 2 demonstrate very similar readings whereas sample 3 is factor 1.6 higher than the other two, this could be due to inconsistency in the printing.

From Smits paper on sheet resistance correction factors (83) we know the correction factor for a 40x40mm square with a 4 point probe with 1mm spacing is 4.512. Therefore with the correction factor we arrive at an average sheet resistance for each of the 3 samples.

To use the measured film thickness and resistance to calculate the resistivity and the conductivity of the printed glassy carbon the following equation is used

$$\rho = R_s \times t$$

where ρ is the bulk resistivity, R_s is the sheet resistance and t is the film thickness. In table 13 the measured resistance using the four-point probe setup is displayed as multimeter resistance in [Ω] which is an average value taken from N=5 measurements. Using the correction factor taken from Smits *et al.* (83), the average sheet resistance is calculated per sample. With this corrected average sheet resistance and the film thickness measurements from table 12, the linear relationship between resistivity, sheet resistance and film thickness is employed to determine the bulk resistivity and subsequently the conductivity for printed glassy carbon over a 40x40mm square. These values are displayed in table 13. The uncertainty in the resistivity and conductivity measurements are calculated using the propagation of uncertainty product rule: $\left(\frac{\Delta A}{A}\right)^2 = \left(\frac{\Delta B}{B}\right)^2 + \left(\frac{\Delta C}{C}\right)^2$ if $A = B \times C$.

Table 13: Measured resistance using four-point probe setup of the 40x40mm glassy carbon screen-printed squares. Further calculations shown per sample gaining values for sheet resistance, resistivity and conductivity of glassy carbon printed squares.

N=5	Sample 1	Sample 2	Sample 3
Measured Resistance [Ω]	15.44	15.61	24.03
Average Sheet Resistance [Ω/□]	69.69 ± 5.31	70.41 ± 3.33	108.43 ± 9.05
Resistivity [$\times 10^{-4}$ Ωm]	2.30 ± 0.48	2.36 ± 0.32	3.78 ± 0.53
Conductivity [$\times 10^{3}$ S/m]	4.35 ± 0.90	4.23 ± 0.58	2.65 ± 0.37

Comparing these results to literature, it's found that these resistivity and conductivity values are similar to those of graphite and carbon black based conductive inks (101). Resistivities of these inks are given in the range of 2.9×10^{-4} Ωm to 12.7×10^{-4} Ωm, thus the resistivity of glassy carbon square samples 1 and 2 is slightly lower than that of the mentioned conductive inks. These conductive inks demonstrate a sheet resistance range of 38.7 to 252.2 Ω/□, depending on the graphite to carbon black ratio (101). Thus the printed glassy carbon is similar in performance to the best performing graphite and carbon black based conductive inks. A different graphite and carbon black based conductive ink reports 0.45×10^{-3} Ωm, which is factor 10 higher than the presented glassy carbon resistivity (102). The best optimised ink in this paper yields a sheet resistance of 22.73 Ω/□, which is approximately 3 times smaller than that of the presented glassy carbon.

Nano carbon inks derived by plasma processes yield resistivities of 39×10^{-4} Ωm to $3,440\times 10^{-4}$ Ωm, dependent on the heat treatment method, which is factor 10-1000 larger than the printed glassy carbon squares (103). Sheet resistances for these nano carbon inks range between 0.15-1.65kΩ/□ thus even the best samples of this material have a higher sheet resistance than the printed glassy carbon (103).

Double walled carbon nanotube based inks investigated by Aziz *et al.* (104) demonstrate a conductivity of 3.6×10^{5} S/m, which is factor 100 higher than the conductivity of the printed glassy carbon squares.

6.4 Use of Glassy Carbon as Temperature Sensor

In this subchapter the behaviour of the screen-printed glassy carbon lines on alumina substrate under changing ambient temperature conditions is studied to determine the usability of glassy carbon as a temperature sensor. The usability of a material as a temperature sensor is defined by its temperature coefficient of resistance, α. In its most general form, the temperature coefficient differential law is

$$\frac{dR}{dT} = \alpha R$$

where the resistance is solely dependent on temperature and thus α is independent of T. Integrating this relationship between T_0 and T the relationship between resistance and temperature is

$$\int_{R_0}^{R} \frac{dR}{R} = \alpha \int_{T_0}^{T} dT$$

$$R(T) = R_0 e^{\alpha(T-T_0)},$$

Which approximates to

$$R(T) = R_0\big(1 + \alpha(T - T_0)\big)$$

By applying the Taylor series approximation. Rearranging this for the temperature coefficient of resistance we arrive at

$$\alpha = \frac{R - R_0}{(T - T_0)R_0}$$

Where T_0 is room temperature and R_0 is the resistance measured at room temperature.

First the relationship between the resistance and temperature of the printed glassy carbon material to find the resistance – temperature differential dR/dT. Then using equation X combined with the entire measurement range the temperature coefficient of resistance is calculated. The experimental setup is a Keithley 2100 multimeter connected to temperature safe wiring running into an oven and connected to the printed glassy carbon lines using crocodile clips as shown in figure 68. One size of printed glassy carbon line is used, the theoretical 28.3x0.7mm line. Using the profilometer data line conductivity section, we know this line is 27.3x0.65mm. The existing internal resistance in the recording circuit (wires and crocodile clips) is measured and found to be insignificant compared to the measured resistances in the glassy carbon printed lines. These internal resistances range from 0.144 to 159kΩ from room temperature to 140°C respectively which is insignificant compared to the resistances measured across the carbon lines which are of the order of several kilo Ohms. All resistance measurements were taken using a moving average over 100 readings. A systematic error exists in this experimental setup as the temperature sensor of the oven positioned in the top of the oven, but the sample was located near the hole for the wires in the centre of the oven. Hence the actual temperature is less than the measured temperatures. This systematic error is assumed to be consistent through the measurements.
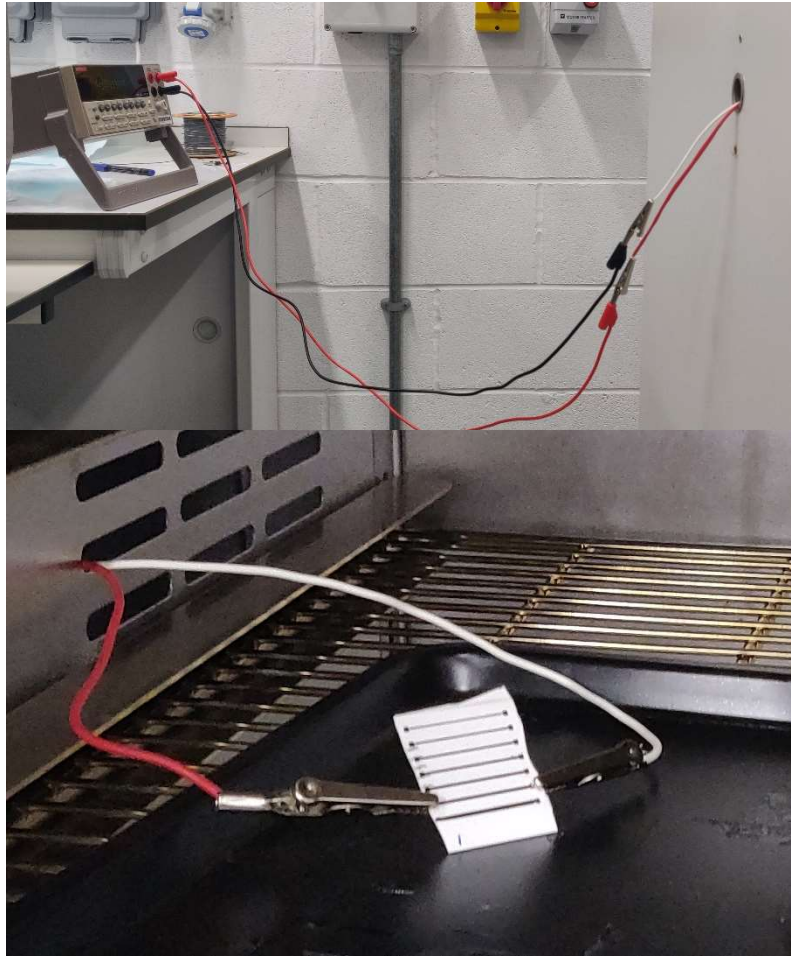
Figure 68. Temperature sensor measurement setup. Keithley 2100 multimeter attached to copper wiring travelling into a Votsch oven to complete the circuit through glassy carbon printed lines on alumina substrate.

A clear decrease in resistance is observed of the order of hundreds of ohms in the glassy carbon line with an increase in temperature across a temperature range from 20 to 140°C. From the data in figure 69 the relationship appears to be linear, thus dR/dT is constant. Using the data from the 4 main data sets displayed in figure 69, the average of rate of change of resistance with respect to temperature is calculated to be

$$\frac{dR}{dT} = -6.89 \pm 1.17 \; \Omega/°C$$
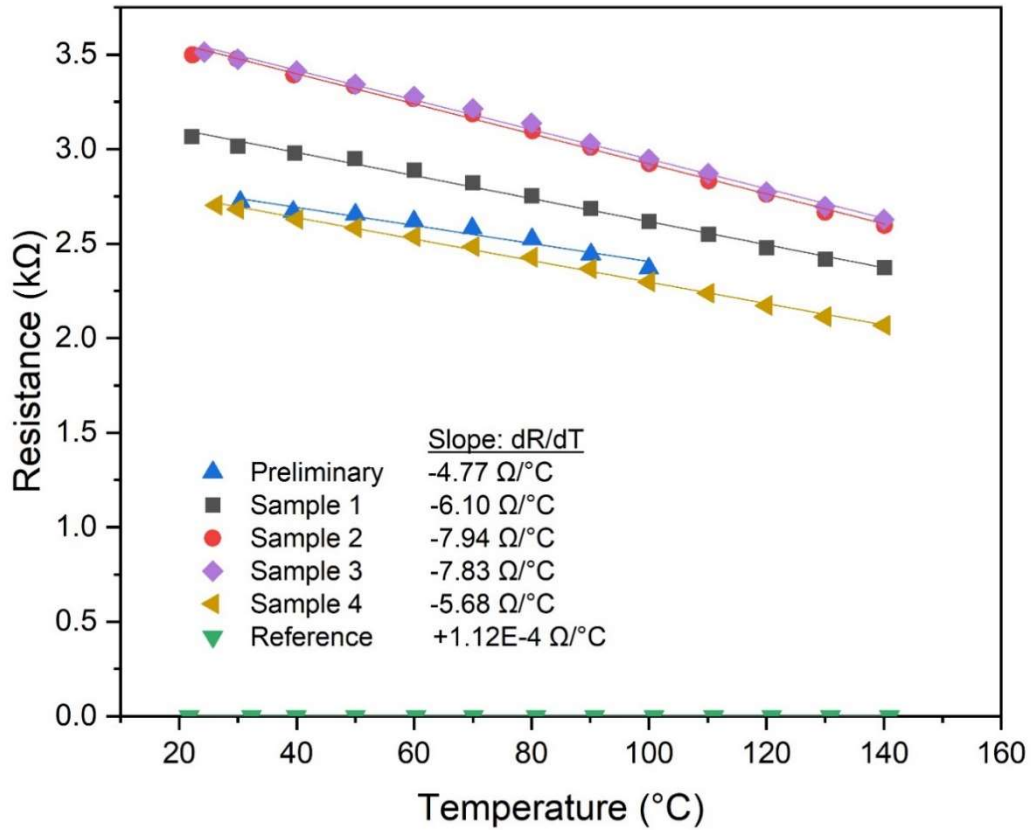
Figure 69. Resistance measured as a function of temperature from 5 independently printed lines of width 0.7mm and 28.3mm length. The preliminary data set has a temperature range of 30-100°C. The reference measurement is the copper wiring of the measuring setup.

In figure 69 all the recorded resistance data in terms of temperature is presented. The preliminary data set (blue) is of a shorter temperature range (30-100°C) because this data was recorded to give an idea of the general behaviour of the printed glassy carbon material. 4 glassy carbon printed line samples were tested at a larger temperature range (room temperature to 140°C) as well as the copper wiring and crocodile clips as a standalone reference sample (green) to check the internal resistance influence of the recorded data. The data from figure 69 shows a linear relationship between temperature and resistance measured on the glassy carbon track, showing its potential viability for use as a temperature sensor. However, there are clearly consistency discrepancies between samples, potentially due to the variance in printed line dimensions and quality as a result of hand screen printing the glassy carbon tracks. Compared to a commercial Pt100 and Pt1000 temperature sensors made by RS, the fundamental interval of the glassy carbon track is measured to be 708Ω on average, compared to the Pt100 and Pt1000 at 38.5Ω and 385Ω respectively. Hence the temperature sensitivity of the platinum temperature sensor in terms of resistance is relatively low at 0.385 Ω/°C compared to the glassy carbon

112

temperature sensor at -6.89 $\Omega/°C$ (120,121). The fundamental interval is the difference in resistance measured over a 100°C interval, usually measured between 0°C and 100°C. As the glassy carbon measurements started at room temperature, the glassy carbon fundamental interval was measured between 30°C and 130°C.

Using the equation

$$\alpha = \frac{R-R_0}{(T-T_0)R_0},$$

and the data from figure 69, the temperature coefficient of resistance is calculated from the 5 data sets to be

$$\alpha = -2043 \pm 150 \, ppm/°C$$

Glassy carbon has the potential of being used as a temperature sensor in chemically hostile conditions due to its chemical resistant nature.

6.5 Use of Glassy Carbon for Salinity Testing

In this section screen printed glassy carbon and intercalated structures are tested in saline solutions to observe the behaviour of glassy carbon in those environments. The printed squares are submerged in a saline solution for an extended period of time to observe the conductivity performance as a function of time spent in a saline environment. The printed intercalated structures are studied using EIS (Electrochemical Impedance Spectroscopy) to determine if the material is a viable option for salinity sensor usage.

6.5.1 Interdigitated Electrodes Salinity Testing

In this section printed interdigitated glassy carbon structures on alumina substrate are exposed to a range of saline solutions with different salt concentrations. The cell constants of the 4 different sizes are calculated using the exposed area and the distance between the two electrodes. EIS is employed to analyse the behaviour of the measured resistance as a function of frequency and as a function of salt concentration to determine the viability of glassy carbon interdigitated structures as a salinity sensor.

The interdigitated structures, or two-electrode cell, uses a connector that creates an electric contact point between a set of wires and the contact pads on the glassy carbon print as shown in figure 70 to make a stable connection to the potentiostat. Saline solutions were made using deionized water mixed with Saxa fine salt which consists of NaCl with

sodium hexacyonoferrate(II) additive. Mass measured using a high precision scale that measures to 0.1mg accuracy, the recorded values are displayed in table 14 along with the calculated concentrations by mass percentage.

Table 14: Measured salt and solution masses to calculate salt concentration of the saline solutions.

NaCl mass [g]	Total solution mass [g]	NaCl concentration [%wt]
0.1257	25.0263	0.50
0.2513	25.0355	1.00
0.3747	25.004	1.50
0.5009	25.0142	2.00
0.6248	25.0151	2.50
0.7505	25.0065	3.00
0.8745	25.0262	3.49
1.0012	24.9974	4.01
1.1261	24.9974	4.50
1.2519	25.0235	5.00
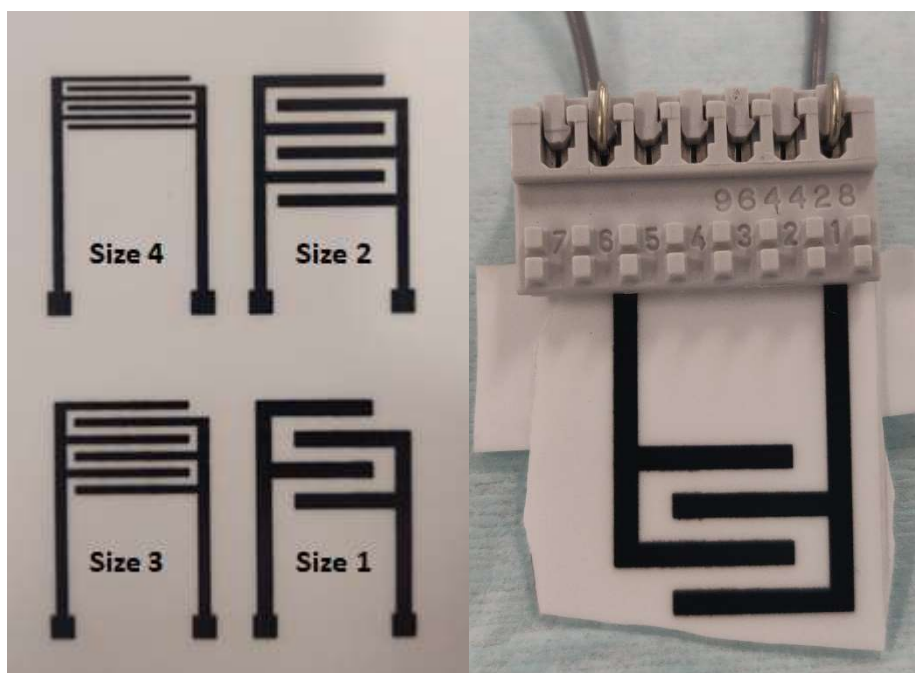
Figure 70. Different sizes of printed glassy carbon interdigitated structures on the left. Example of an interdigitated sample of size 1 attached to the connector to connect the interdigitated structure to the potentiostat.

Table 15: Using profilometry measurements the film thickness and width of the 4 different sizes interdigitated structures is measured. 5 measurements are taken per sample size, presenting an average value with sample standard deviation.

N=5	Film thickness [μm]	Line width [mm]
Size 1	2.55 ± 0.18	1.287 ± 0.007
Size 2	3.04 ± 0.11	0.992 ± 0.015
Size 3	2.01 ± 0.25	0.606 ± 0.017
Size 4	2.56 ± 0.25	0.396 ± 0.013

To find the stability window of the glassy carbon interdigitated structures in aqueous salt solution (see figure 71), cyclic voltammetry is used to explore its behaviour across a potential range. The potential range will always be symmetric around the 0V point as it's a symmetric full cell, hence the working electrode and the counter/reference electrode are made of the same material. From the data in figure 72 its observed that it's stable from -0.5V to +0.5V in a salt solution of 1% concentration my mass. This absolute stability

window of 1.0V is expected because as a water-based electrolyte, the range between water splitting in the form of hydrogen or oxygen $\approx 1.23V$.

Figure 71. Interdigitated glassy carbon structure on alumina substrate in salt solution (5% concentration by mass). Wires attached to an electrode connector which clamps onto the glassy carbon connection points to complete the circuit between the electrodes and the potentiostat.
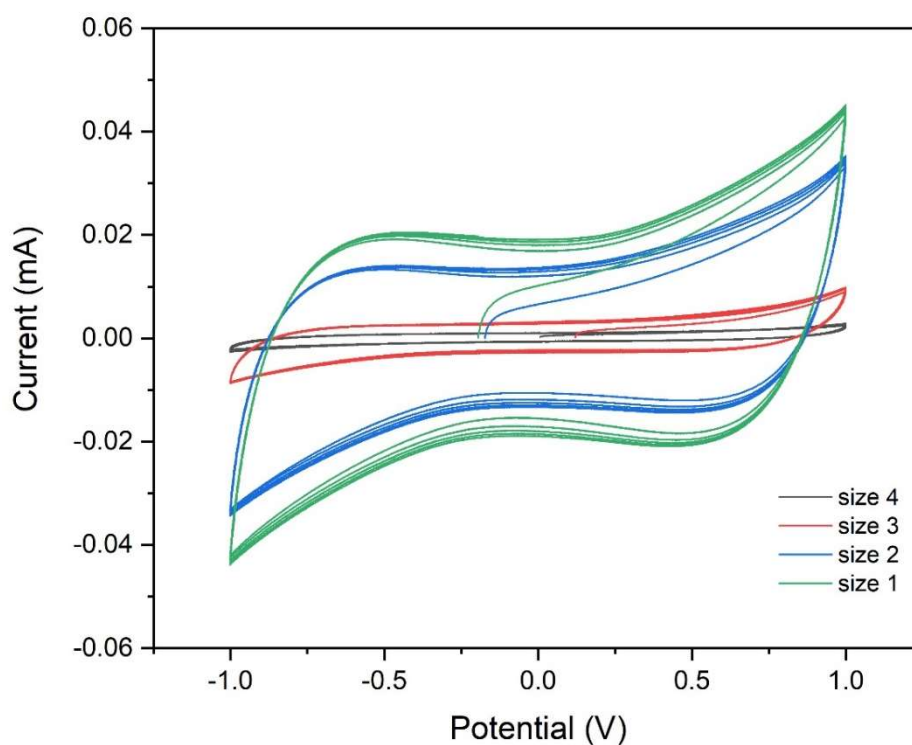
Figure 72. Cyclic voltammetry of the glassy carbon interdigitated structures in salt solution (1% NaCl concentration by mass) by size.

For each sample EIS measurements are taken using 5 voltages that lie in the stability window of the carbon material, these voltages are chosen at -0.50, -0.25, 0.00, +0.25, +0.50V. This yield enough data so that an average impedance may be calculated with an acceptable standard deviation. An example of this is shown in figure 73, where we see a very high impedance at low frequency which decreases with an increasing frequency where it eventually stabilizes. The real component of the impedance at high frequency is the important value as salinity sensors use a high frequency to record their measurements. The fact that the resistance stabilizes at high frequency indicates that glassy carbon can potentially be used as a salinity sensor material (105–107).
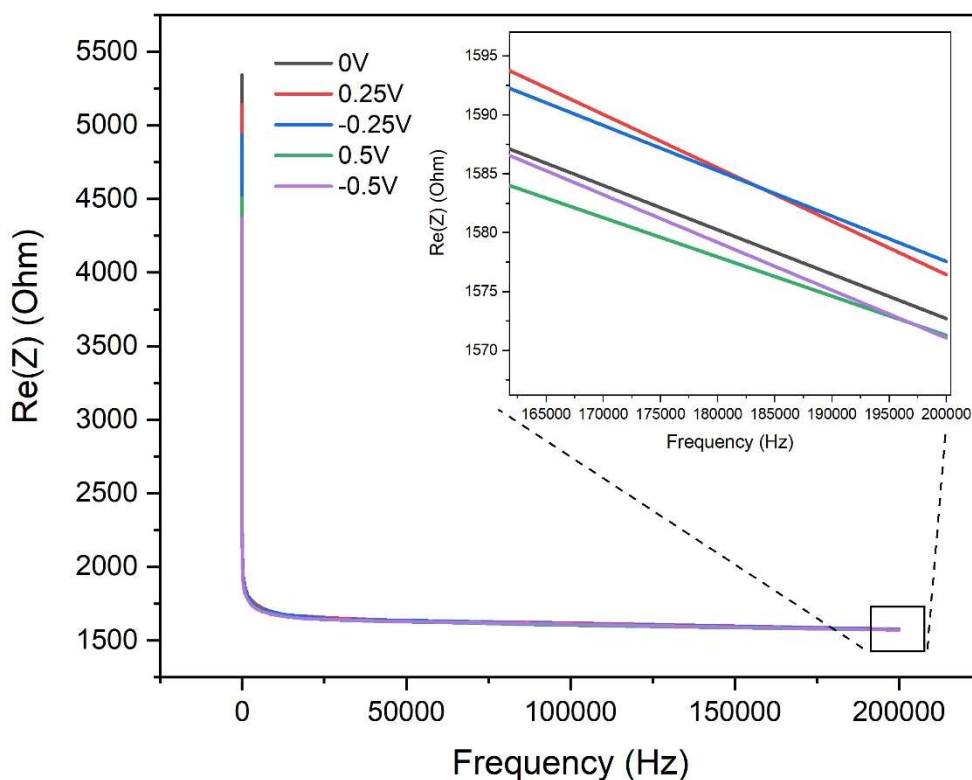
Figure 73. Real component of impedance plotted against the frequency of the AC current using the size 1 interdigitated structure sample using 5 different voltages.

Table 16: Dimensional measurements of the interdigitated structures to calculate the cell constant of each size of interdigitated structure. Where L = length of finger, S = gap between fingers, W = line width, N = number of fingers.

	L [mm]	S [mm]	W [mm]	N [number]	Cell Constant
Size 1	6.6	1.3	1.29	4	0.102
Size 2	9.0	1.0	0.99	6	0.045
Size 3	9.6	0.79	0.61	6	0.045
Size 4	10.7	0.40	0.40	6	0.038

The cell constant of an interdigitated structure is an empirical value that calculated by 4 factors of the geometry of said interdigitated structure. The geometry factors and the calculated cell constant per size of printed interdigitated structure is shown in table 16. The empirically derived equation for the cell constant is

$$K = \frac{2 \left(\frac{S}{E}\right)^{\frac{1}{3}}}{L(N-1)}$$

where K is the cell constant, L is the length of the fingers, S is the gap between the fingers, W is the line width and N is the number of fingers. This cell constant is a proportionality factor in the relationship between the conductivity, conductance, resistivity and the resistance of the electrolyte (105–107). The relationship between conductivity and resistance is described as

$$\sigma = \frac{K}{R} = KG$$

where σ is the bulk conductivity in [S/cm], K is the cell constant in [cm^{-1}], R is the measured resistance in [Ω] and G is the conductance in [S]. The cell constant can also be used to find the specific resistance of the electrolyte using

$$R = K\rho$$

where ρ is the specific resistivity of the electrolyte in [Ωcm].
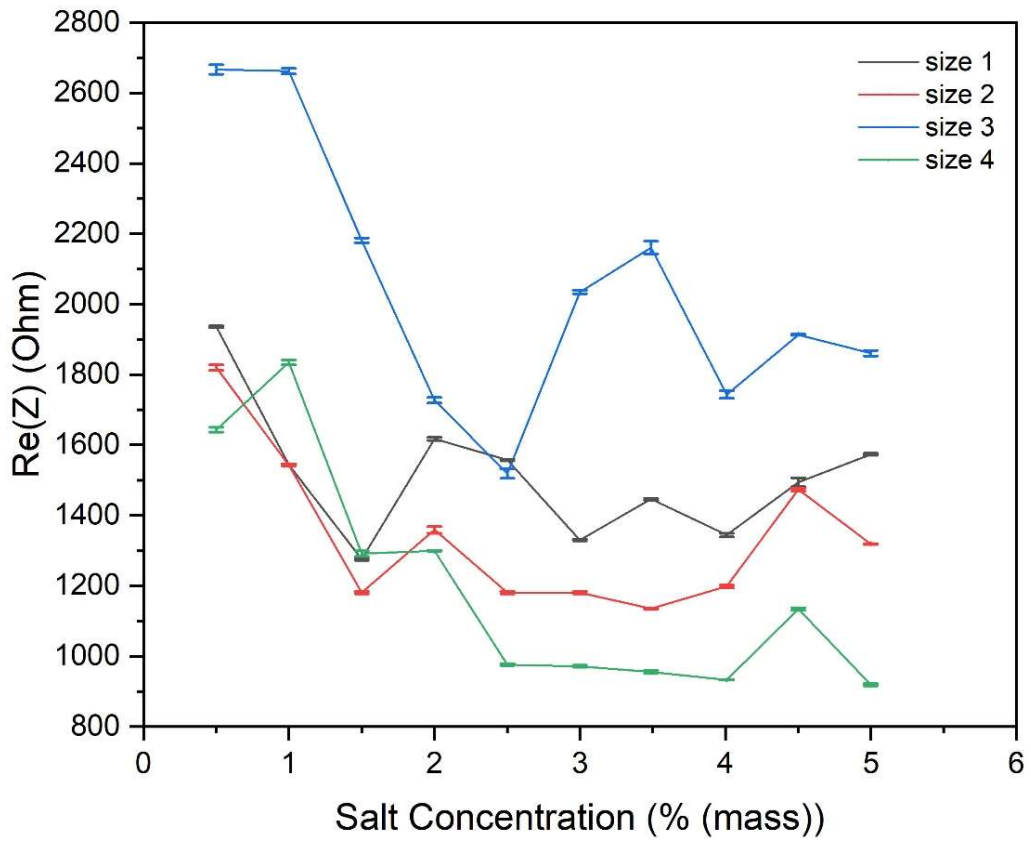
Figure 74. Real component of the impedance measured at each tested salt concentration using all 4 sizes of the interdigitated structures.

In figure 74 the real component is plotted as a function of the salt solution concentration. The error bars in the graph are produced by taking 5 measurements per sample per salt concentration, thus an average value with standard deviation is obtained. A linear relationship between the resistance and the salt concentration would indicate an interdigitated structure with the correct cell constant to measure that particular salt concentration range. The data in figure 74 shows that the 4 tested sizes of interdigitated structures were not of the correct cell constant to be used as salinity sensors for 0.5% to 5% mass concentration salt solutions, because there is no linear relationship between the measured resistance and therefore the specific resistivity or conductivity of the electrolyte and the salt solution concentration.

Future experiments should include a wide sweep of salt concentrations for these interdigitated structures with this range of cell constants or a batch of interdigitated structure with a wider variety of cell constants must be trialled to find the correct cell constant using glassy carbon for this salinity range.

6.5.2 Preliminary Long Term Saline Exposure Study

A short preliminary study was initiated to investigate the longevity of glassy carbon coatings to long term exposure to salt solutions. A screen-printed glassy carbon 40x40mm square is submerged in 5% concentration by mass saline solution for 8 days to measure the change in sheet resistance over this time period, of which the data is presented in table 17.
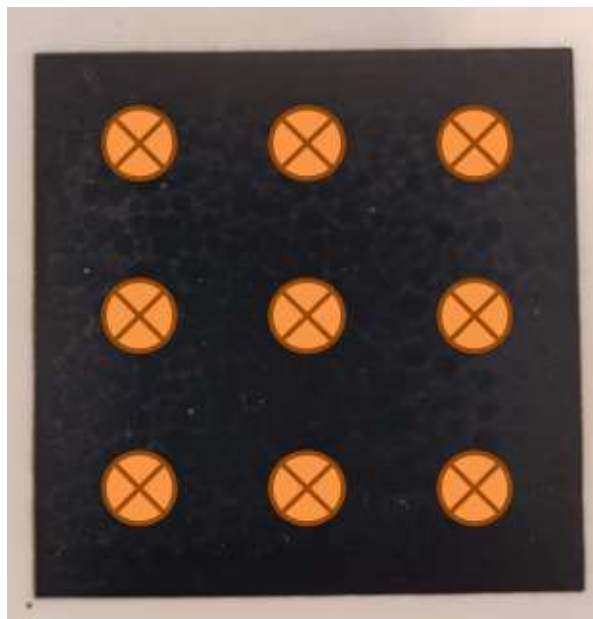
Figure 75. 40x40mm screen printed glassy carbon on alumina substrate with locations of sheet resistance measurements taken using the 4-point probe.

Table 17: Sheet resistance measurements taken over an 8-day period using the 4-point probe. 9 measurements were taken of the sample each day to produce an average value with sample standard deviation.

Day	Sheet resistance [$\Omega/\square$]	Standard deviation [$\Omega/\square$]
0	109.1	8.0
1	114.3	8.0
2	111.8	8.0
3	111.7	8.7
8	117.5	11.3
70	*Above recordable range*	*Above recordable range*

Table 18: Screen printed glassy carbon surface roughness measurements using white light interferometry. Sample 1 spent 70 days in 5% NaCl solution, samples 2 and 3 spent 70 days in air.

N=6	Fresh Screen-Printed Glassy Carbon Surface Roughness, Sa [nm]	70 Days after printing Surface Roughness, Sa [nm]
Sample 1	247.2 ± 14.7	395.6 ± 44.9
Sample 2	267.2 ± 26.6	359.5 ± 13.8
Sample 3	257.9 ± 21.8	371.0 ± 16.2

After 70 days of submersion in the 5% concentration saline solution the glassy carbon square was revisited. No sheet resistance measurements could be taken, indicating deterioration of the surface of the carbon layer. White light interferometry was utilized to check the difference between the surface roughness of a newly carbonized screen-printed glassy carbon square to the one exposed to a saline solution for 70 days. The data in table 18 shows the surface roughness of 3 printed squares after carbonization and after 70 days of either exposure to air or saline solution.

6.6 Chapter Closure

White light interferometry was used to demonstrate the difference in surface roughness of glassy carbon coatings produced by bar coating and screen-printing precursor deposition methods. Screen printing yielded a surface roughness of 247 ± 15nm, whereas the bar coating produced a surface roughness of 137 ± 13nm.

Screen printed glassy carbon lines of an array of widths (0.3 – 1.0mm) and screen-printed squares (40x40mm) were used to calculate the bulk conductivity and resistivity of glassy carbon. Both methods measured conductivities and resistivities in the same order of magnitude although the printed lines showed slightly better performance over the printed squares. The best printed lines had a resistivity of $1.86 \pm 0.16 \times 10^{-4}$ Ωm and a conductivity of 5.41×10^3 S/m, whereas the printed squares yielded a resistivity of $2.30 \pm 0.16 \times 10^{-4}$ Ωm and a conductivity of 4.35×10^3 S/m. This screen printed glassy carbon had similar conductivity to graphite and carbon black based conductive inks, better conductivity than nano carbon inks but is outperformed by double walled carbon nanotube based inks (101–104). Screen printed glassy carbon showed the ability to use glassy carbon as conductive tracks with comparable performance to carbon based conductive inks with the added benefits glassy carbon's natural chemical resistance and gas impermeability, which could be desirable material characteristics for electronics in harsh environments. The use of glassy carbon in electronics is clearly limited by the carbonization temperatures required to transform the printed precursor into glassy carbon. The novel method of using photonic curing to produce glassy carbon is recommended for future research into the use of glassy carbon in electronics. Photonic curing has the potential to carbonize glassy carbon on temperature sensitive substrates such as PET, to produce cheap and flexible conductive tracks with the chemical resistance, low reactivity and gas impermeability that glassy carbon offers.

Four screen-printed glassy carbon lines of dimensions 27.3x0.65mm, were used to explore the ability to use glassy carbon as a temperature sensor. The resistance across the printed lines was measured at a temperature range from 20°C to 140°C. These results showed that glassy carbon had a resistance differential with respect to temperature equal to $dR/dT = -6.89 \pm 1.17$ Ω/°C and a temperature coefficient of resistance equal to $\alpha = -2043 \pm 150 \, ppm/°C$. The resistance as a function of temperature was clearly linear thus glassy carbon showed potential to be used as a temperature sensor in the investigated

temperature range. The fundamental interval of glassy carbon was compared to commercial Pt100 and Pt1000 temperature sensor produced by RS (UK), glass carbon's fundamental interval was measured to be 708Ω compared to Pt100 and Pt1000's 38.5Ω and 385Ω respectively. This suggests that glassy carbon's resistance changes more with a change in temperature compared to the platinum based commercial sensors, in potentially allowing glassy carbon to make more accurate temperature measurements if the consistency discrepancies of the material can be solved. Print quality and dimension optimization for future work is recommended as a starting point for improving the use of glassy carbon as temperature sensors.

Screen printed glassy carbon interdigitated structures were used to test the viability of glassy carbon as a salinity sensor material. EIS was used to study the resistance of the interdigitated structures in an aqueous salt solution (NaCl) of concentrations 0.5 to 5.0% by mass. The resistance measured as a function of frequency showed a constant resistance at the higher end of the frequency spectrum, suggesting glassy carbon is usable as a salinity sensor. Resistance as a function of salinity, or salt concentration, does not seem to have a linear relationship and thus the interdigitated glassy carbon structures of these specific cell constants are not suitable for this salinity range. For future work on glassy carbons in interdigitated structures for salinity sensors a full study of a wide range of cell constants and aqueous salt solution concentrations is required to find the window where the glassy carbon could potentially be used as a salinity sensor. If successful, photonic curing could then be employed to produce these sensors on cheap and flexible substrates.

Chapter 7: Conclusions and Recommendations

7.1 Introduction

The aim of this thesis was to explore the manufacture of glassy carbon thin films using a novel rapid processing method in photonic curing and to expand the applications of glassy carbon in terms of energy storage and printed electronics.

The endeavours of the research into manufacturing glassy carbon using photonic curing resulted in a publication in the Journal of Material Science on the 3rd of January 2022, titled "Glassy carbon manufacture using rapid photonic curing" (1).

The research in this thesis is presented in 3 results chapters. The first results chapter compared the novel carbonization method of photonic curing to the conventionally used thermal carbonization, followed by a material characterisation comparison between the two methods. The second results chapter explored the usability of the glassy carbon thin films produced in the first results chapter as energy storage electrode active materials, comparing the two carbons to each other and to literature. In the third results chapter, the potential applications of glassy carbon in printed electronics and sensors were explored. In the final results chapter, the novel photonic cured carbon could not be compared to the conventional thermal carbonized carbon due to equipment malfunction.

This chapter presents conclusions from the performed research into glassy carbon manufacturing methods and applications, followed by recommendations for improvements and further research directions.

7.2 Conclusions

As a result of the research performed for this doctorate several conclusions have been made, of which the main points are summarised, and in-depth conclusions are made in the following paragraphs.

- Photonic curing was able to convert a phenol formaldehyde resin precursor into a bulk glassy carbon structure which was sp^2 dominant, as indicated by Raman spectroscopy, and closely resembled a conventional derived glassy carbon structure produced from thermal carbonization at 800°C.

- Photonic curing was able to carbonize the precursor in around 1 minute, a manifold reduction in processing time compared with the approximately 20 hours processing time when using a conventional thermal conversion method.

- Carbon coatings produced using photonic curing were flexible, highly smooth and did not show any evidence of surface defects, such as pinholes, delamination or scratches.

- The ability to rapidly manufacture glassy carbon coatings, by way of photonic curing, expands the potential window of applications of glassy carbons for high volume applications such as coatings for energy storage, rapid manufacture of complex electrically conductive shapes, and the opportunity to use temperature sensitive substrates.

- Photonic cured carbon showed comparable electrochemical performance to thermal produced glassy carbon and to porous glassy carbon in literature (70) in terms of specific capacitance.

- Screen printed glassy carbon structures yielded conductivities comparable to carbon based conductive inks (101–104), potentially expands the applications window for glassy carbon for devices requiring electrically conductive shapes with high chemical resistance, low reactivity and high thermal stability.

Photonic curing as a novel carbonization method to produce glassy carbon thin films from phenol formaldehyde deposition layer was achieved and verified by comparing photonic curing to thermal carbonization using material characterisation methods such as SEM, white light interferometry, Raman spectroscopy and XPS. Further verification through electrochemical testing using CV, EIS and GCD showed that the carbons produced using different methods perform similarly as active material electrode materials for energy storage.

The material characterisation of the photonic cured carbon and the thermal carbonized carbon showed that these carbon materials are a close match. Raman spectroscopy showed that both carbons are sp^2 hybridized bond dominated and that the crystallite size of a thermal carbonized carbon produced at 800°C is equivalent to that of a photonic cured carbon produced using 20 pulses of 27J/cm^2 output energy density. The XPS data showed an equivalence in elemental composition and binding energy peak locations between the thermal carbonized carbon, photonic cured carbon and a commercial graphite reference sample. Using the empirical D-parameter method for the carbon Auger peaks (C KLL) of the

XPS data, it was found that the thermal produced carbon was sp^2 dominated whereas the photonic cured carbon was a combination of sp^2/sp^3 hybridized bonds at the sample surface (top 5-10nm). This is likely associated with the different environmental conditions of the sample during carbonization.

Using photonic curing as a carbonization method to produce glassy carbon was limited by the coating thickness of the precursor. A theoretical wet deposition of 4µm, resulting in a ~1µm dry precursor coating was the thickest layer to be successfully carbonized and to adhere to the stainless-steel substrate. Theoretical wet deposition layer thicknesses greater than 4µm still carbonized by photonic curing but experienced surface fracturing and delamination off the substrate. Thermal carbonization to produce glassy carbon is also limited by the layer thickness of the precursor, although a wider range of thicknesses was found to make successful glassy carbon thin films compared to photonic curing. Thermal carbonization successfully carbonized theoretical wet deposition layers of 4µm to 12µm using bar coating on stainless steel substrates and 13µm using screen printing on alumina substrates.

From the CV manipulated data using Dunn's method, photonic cured and thermal carbonized glassy carbon thin films are both found to be dominated by diffusion-controlled processes at the electrode-electrolyte interface. The specific capacitance of the two carbon materials was calculated from the EIS and GCD data, $0.49 - 8.94$ mF/cm^2 and $1.27 - 10.68$ mF/cm^2 were measured for the thermal and photonic cured carbons respectively. Comparing these capacitances to the use of porous glassy carbon as a supercapacitor electrode in literature (70), which shows specific capacitances of $3.14 - 4.28$mF/cm^2, it's concluded that photonic curing can be used to rapidly produce glassy carbon thin films with capacitances that are competitive to other glassy carbon materials.

Screen printing the precursor resin onto alumina substrates in geometries for electrical performance testing and exploring the viability of glassy carbon as sensors of different applications resulted in finding glassy carbon has a bulk conductivity of 5.41×10^3 S/m, which is comparable to conductive carbon inks (101–104). Assuming that photonic cured glassy carbon is going to behave similarly thermal carbonized glassy carbon in terms of conductivity, as it has been similar to thermal glassy carbon in every other characterisation parameter, photonic curing could have potential applications in printed electronics and sensors by offering a rapid manufacturable, flexible, electrically conductive, thermally stable, chemically resistive thin film material.

Glassy carbon as a temperature sensor showed clear linear relationships between the measured resistance and the ambient temperature, making glassy carbon a viable option as a temperature sensor. The fundamental interval of glassy carbon was measured to be 708Ω, approximately twice that of a commercial Pt1000 temperature sensor made by RS (UK) which is advertised at 385Ω. This means that glassy carbon has the potential to give more accurate readings of smaller temperature changes compared to the platinum-based sensors, but the glassy carbon sensors were found to be inconsistent in absolute resistance measurements between samples. This inconsistency is likely caused by the screen printing performed by hand and would likely improve with the use of an automated screen printer with optimized printing parameters. Again, assuming that photonic cured carbon behaves like thermal carbonized glassy carbon as a temperature sensor, photonic curing would allow for the production of flexible glassy carbon temperature sensors. These would of course only be viable for temperature applications within the thermal stability of the chosen substrate.

The interdigitated structures that were produced by screen printing the precursor resin on alumina substrates were used to explore the potential use of glassy carbon as a salinity sensor. Using EIS, the glassy carbon was found to have a stable resistance at high current frequencies, which is a desirable characteristic for salinity sensors. To make a practical salinity sensor, the salinity of the aqueous environment must have a linear relationship with the measured resistance at high current frequencies. In the limited investigated range of cell constants and salinity concentrations the glassy carbon was found to not work as a salinity sensor. This was likely due to the cell constant and the salinity range not being compatible as the glassy carbon materials showed good chemical resistance and a stable resistance and high frequency alternating currents which are promising materials characteristics for salinity sensors.

7.3 Recommendations

In this section recommendations are made for future work that could be done building on the presented work in this thesis. Improvements, additions and future research endeavours are therefore discussed for several aspects of this doctoral research.

In the material characterisation of the photonic curing produced glassy carbon thin films, the future addition of XRD and TEM characterisation is recommended to study the d-spacing parameter of the carbon materials. This would add another parameter to compare

between the photonic curing and thermal carbonization produced carbons as well as adding an important parameter in terms of energy storage applications where the d-spacing is attributed to the materials ability to store ions of different sizes. In addition to the current Raman spectroscopy characterisation, a variety of laser wavelengths would allow for a study of the carbon structure at a range of penetration depths as longer wavelengths penetrate deeper into the carbon coatings. This would enable the assessment of the progression of the glassy carbon layer for different photonic curing parameters.

The photonic curing equipment malfunctioned after the thin film development stage, prevent use in an in-depth study of the photonic curing parameters and its effects on the carbon thin films. One day was spent using a photonic curing system in industry as a preliminary study investigating to possibility of producing glassy carbon thin films on temperature sensitive substrates like aluminium. The lamp in this photonic curing system had an energy density output of 14.6J/cm^2, approximately half the energy density used to produce the photonic cured carbon thin films used in this study. This preliminary study yielded no usable quantitative results to present, although it was found that this lower energy density output could not carbonize the precursor without overheating the sample holder and compromising the temperature sensitive substrates.

Further recommended studies using photonic curing include the study of a range of energy densities and pulses repetitions and the effects it has on the produced carbon thin films. Starting this study using the stainless steel as a substrate before exploring the use of temperature sensitive substrates is also recommended. As the photonic cured carbon was limited by the deposition layer thickness of the precursor, an investigation of adding layers of precursor to previously carbonized thin films is recommended.

The ability to produce glassy carbon on temperature sensitive substrates would potentially open glassy carbon to a host of new applications, therefore a wide range of substrate materials should be investigated as a future endeavour in the research of producing glassy carbon using photonic curing as the carbonization method. Substrate materials that are recommended are: aluminium and nickel for energy storage applications, cheap flexible plastics such as PET for printed electronics and sensors, and even common plastics for 3D printing for potential biomedical implant coating applications.

If glassy carbon is successfully produced on aluminium substrates, the electrochemical characterisation of the photonic cured carbon as an active electrode material could

performed to study the effect of the stainless-steel substrate on the capacitance shown by the glassy carbon in this work.

In further studies with regards to using glassy carbon in printed electronics and sensors, it's recommended that temperature sensitive substrates are explored using photonic curing as the carbonization method, and the use of automated screen-printing equipment with optimized printing parameters for a better quality and repeatability between precursor depositions. For the temperature sensors, to explore the usable temperature range of glassy carbon, a comprehensive study of temperature ranges is required to ascertain where glassy carbon displays a linear relationship between ambient temperature and measured resistance. Further studies for glassy carbon as a salinity sensor material are recommended as the material shows good resistance stability at high current frequencies. These studies should initially be broad to find a cell constant that performs well using glassy carbon for a particular salinity range.

References

1. de Boode B, Phillips C, Lau YC, Adomkevicius A, McGettrick J, Deganello D. Glassy carbon manufacture using rapid photonic curing. J Mater Sci. 2022;57(1):299–310.

2. Harris PJF. Structure of non-graphitising carbons a b. 1997;42(5):206–18.

3. Thrower PA. Glassy Carbon. 2007;163–4.

4. Harris PJF. Fullerene-related structure of commercial glassy carbons. Philos Mag. 2004;84(29):3159–67.

5. Zittel HE, Miller FJ. A Glassy-Carbon Electrode for Voltammetry. Anal Chem. 1965;37(2):200–3.

6. Van der Linden WE, Dieker JW. Glassy carbon as electrode material in electro-analytical chemistry. Anal Chim Acta [Internet]. 1980;119(1):1–24. Available from: http://www.sciencedirect.com/science/article/pii/S0003267000000258%5Cnhttp://linkinghub.elsevier.com/retrieve/pii/S0003267000000258

7. Yagi S, Tanaka A, Ichikawa Y, Ichitsubo T, Matsubara E. Electrochemical Stability of Magnesium Battery Current Collectors in a Grignard Reagent-Based Electrolyte. J Electrochem Soc [Internet]. 2013;160(3):C83–8. Available from: http://jes.ecsdl.org/cgi/doi/10.1149/2.033303jes

8. Bokros JC. Carbon Biomedical Devices. Carbon N Y. 1971;I.

9. Markle DH, Grenoble DE, Melrose RJ. Histologic Evaluation of implants in Dogs. Biomat Med Dev Art Org. 1975;3(1):97–114.

10. Wang J, Li M, Shi Z, Li N, Gu Z. Direct electrochemistry of cytochrome c at a glassy carbon electrode modified with single-wall carbon nanotubes. Anal Chem. 2002;74(9):1993–7.

11. Fagan DT, Hu IF, Kuwana T. Vacuum Heat Treatment for Activation of Glassy Carbon Electrodes. Anal Chem. 1985;57(14):2759–63.

12. McDermott MT, McCreery CA, McDermott RL. Scanning Tunneling Microscopy of Carbon Surfaces: Relationships between Electrode Kinetics, Capacitance, and Morphology for Glassy Carbon Electrodes. Anal Chem. 1993;65(7):937–44.

13. Zhang L, Yuan R, Chai Y, Li X. Investigation of the electrochemical and electrocatalytic behavior of positively charged gold nanoparticle and l-cysteine film on an Au electrode. Anal Chim Acta. 2007;596(1):99–105.

14. Plock CE, Vasquez J. Use of glassy carbon as a working electrode in controlled potential coulometry. Talanta. 1969;16(11):1490–2.

15. Gattrell M, Kirk DW. The electrochemical oxidation of aqueous phenol at a glassy carbon electrode. Can J Chem Eng. 1990;68(6):997–1003.

16. Swain GM. The Susceptibility to Surface Corrosion in Acidic Fluoride Media: A Comparison of Diamond, HOPG, and Glassy Carbon Electrodes. J Electrochem Soc [Internet]. 1994;141(12):3382. Available from:

http://jes.ecsdl.org/cgi/doi/10.1149/1.2059343

17. Wall C, Zhao-Karger Z, Fichtner M. Corrosion Resistance of Current Collector Materials in Bisamide Based Electrolyte for Magnesium Batteries. ECS Electrochem Lett [Internet]. 2014;4(1):C8–10. Available from: http://eel.ecsdl.org/cgi/doi/10.1149/2.0111501eel

18. Yi Y, Weinberg G, Prenzel M, Greiner M, Heumann S, Becker S, et al. Electrochemical corrosion of a glassy carbon electrode. Catal Today [Internet]. 2017;295(February):32–40. Available from: http://dx.doi.org/10.1016/j.cattod.2017.07.013

19. Lewis IC, Pirro TA, Miller DJ. Method for making a graphite component covered with a layer of glassy carbon. 1995;1(1):2020–3.

20. Bokros JC. Blood Filter Using Glassy Carbon Fibres. 1976;(19):19–22.

21. Jenkins GM, Grigson CJ. The fabrication of artifacts out of glassy carbon and carbon-fiber-reinforced carbon for biomedical applications. J Biomed Mater Res. 1979;13(3):371–94.

22. Jonhnson KK, Jones LE, Johnson KK. Phenol-Formaldeyde Resin Structure for the Synthesis of Glassy Carbon. 1997;478–9.

23. Icatovic Z, Konibinat K. Curing of Resole-Type Phenol-Formaldehyde Resin. 1967;11:85–93.

24. Bhatia G, Aggarwal RK, Malik M, Bahl OP. Conversion of phenol formaldehyde resin to glass-like carbon. J Mater Sci. 1984;19(3):1022–8.

25. Laušević Z, Marinković S. Mechanical properties and chemistry of carbonization of Phenol formaldehyde resin. Carbon N Y. 1986;24(5):575–80.

26. Schueller OJA, Brittain ST, Whitesides GM. Fabrication of glassy carbon microstructures by pyrolysis of microfabricated polymeric precursors. Adv Mater. 1997;9(6):477–80.

27. Schneller OJA, Brittain ST, Whitesides GM. Fabrication of glassy carbon microstructures by soft lithography. Sensors Actuators, A Phys. 1999;72(2):125–39.

28. Fitzer E, Schäfer W. The effect of crosslinking on the formation of glasslike carbons from thermosetting resins. Carbon N Y. 1970;8(3):353–64.

29. Šupová M, Svítilová J, Chlup Z, Černý M, Weishauptová Z, Suchý T, et al. Relation between mechanical properties and pyrolysis temperature of phenol formaldehyde resin for gas separation membranes. Ceram - Silikaty. 2012;56(1):40–9.

30. Fitzer E, Schaefer W, Yamada S. The formation of glasslike carbon by pyrolysis of polyfurfuryl alcohol and phenolic resin. Carbon N Y. 1969;7(6):643–8.

31. Guillot MJ, Schroder KA, Mccool SC. IMECE2012-87674. 2016;1–9.

32. Cui HW, Jiu JT, Nagao S, Sugahara T, Suganuma K, Uchida H, et al. Ultra-fast photonic curing of electrically conductive adhesives fabricated from vinyl ester resin and silver micro-flakes for printed electronics. RSC Adv. 2014;4(31):15914–22.

33. Das S, Yang B, Gu G, Joshi PC, Ivanov IN, Rouleau CM, et al. High-Performance Flexible Perovskite Solar Cells by Using a Combination of Ultrasonic Spray-Coating and Low Thermal Budget Photonic Curing. ACS Photonics. 2015;2(6):680–6.

34. Schroder KA. Mechanisms of photonic curing™: Processing high temperature films on low temperature substrates. Tech Proc 2011 NSTI Nanotechnol Conf Expo, NSTI-Nanotech 2011. 2011;2:220–3.

35. Akhavan V, Schroder K, Pope D, Farnsworth S. Processing thick-film screen printed Metalon® CuO reduction ink with PulseForge® tools. Coat Int. 2013;46(3):14–7.

36. Assaifan AK, Alshehri NA, Lewis AR, Samavat S, Lau YC, Deganello D, et al. Effect of intense pulsed light on hydrothermally grown ZnO nanowires. Mater Lett [Internet]. 2020;271:127797. Available from: https://doi.org/10.1016/j.matlet.2020.127797

37. Cronin HM, Stoeva Z, Brown M, Shkunov M, Silva SRP. Photonic Curing of Low-Cost Aqueous Silver Flake Inks for Printed Conductors with Increased Yield. ACS Appl Mater Interfaces. 2018;10(25):21398–410.

38. Bouchet-Fabre B, Marino E, Lazar G, Zellama K, Clin M, Ballutaud D, et al. Spectroscopic study using FTIR, Raman, XPS and NEXAFS of carbon nitride thin films deposited by RF magnetron sputtering. Thin Solid Films. 2005;482(1–2):167–71.

39. Baldan MR, Almeida EC, Azevedo AF, Gonçalves ES, Rezende MC, Ferreira NG. Raman validity for crystallite size L a determination on reticulated vitreous carbon with different graphitization index. Appl Surf Sci. 2007;254(2):600–3.

40. Franklin E. Crystallite growth in graphitizing and non-graphitizing carbons. Proc R Soc London Ser A Math Phys Sci. 1951;209(1097):196–218.

41. Saxena R, Bragg R. Electrical Conduction in Glassy Carbon. J Non Cryst Solids. 1977;(1978):282–4.

42. Zhou Z, Bouwman WG, Schut H, Pappas C. Interpretation of X-ray diffraction patterns of (nuclear) graphite. Carbon N Y [Internet]. 2014;69:17–24. Available from: http://dx.doi.org/10.1016/j.carbon.2013.11.032

43. Pandolfo AG, Hollenkamp AF. Carbon properties and their role in supercapacitors. J Power Sources. 2006;157(1):11–27.

44. Hou H, Qiu X, Wei W, Zhang Y, Ji X. Carbon Anode Materials for Advanced Sodium-Ion Batteries. Adv Energy Mater. 2017;7(24):1–30.

45. Noda T, Inagaki M. The structure of glassy carbon. Mater Res Bull. 1964;37(10):1249–55.

46. Jenkins G, Kawamura K, Ban L. Formation and structure of polymeric carbons. Proc R Soc Lond A Math Phys Sci [Internet]. 1972;327(1571):501–17. Available from: http://www.jstor.org/stable/10.2307/78220%5Cnhttp://www.jstor.org/stable/78220

47. Jurkiewicz K, Pawlyta M, Zygadło D, Chrobak D, Duber S, Wrzalik R, et al. Evolution of glassy carbon under heat treatment: Correlation structure–mechanical properties. J Mater Sci. 2018;53(5):3509–23.

48.   Minami N, Ino T. The structure of glassy carbon. Jpn J Appl Phys. 1986;25(3 R):328–35.

49.   Braun A, Bärtsch M, Schnyder B, Kötz R, Haas O, Haubold H-G, et al. X-ray scattering and adsorption studies of thermally oxidized glassy carbon. J Non Cryst Solids [Internet]. 1999;260(1–2):1–14. Available from: http://www.sciencedirect.com/science/article/pii/S0022309399005712

50.   Zhao M, Song H, Chen X, Lian W. Large-scale synthesis of onion-like carbon nanoparticles by carbonization of phenolic resin. Acta Mater. 2007;55(18):6144–50.

51.   Baranov A V., Bekhterev AN, Bobovich YS, Petrov VI. Interpretation of some singularities in raman-spectra of graphite and glass carbon. Opt I Spektrosk. 1987;62(5):1036–42.

52.   Ferrari AC, Robertson J. Interpretation of Raman spectra of disordered and amorphous carbon. 2000;31(2):632–45.

53.   Lim Y, Chu JH, Lee DH, Kwon SY, Shin H. Increase in graphitization and electrical conductivity of glassy carbon nanowires by rapid thermal annealing. J Alloys Compd [Internet]. 2017;702:465–71. Available from: http://dx.doi.org/10.1016/j.jallcom.2017.01.098

54.   Xu L, Wu JF, Bai S. Boron-doped glassy carbon fabricated by chemical vapor deposition. Xinxing Tan Cailiao/New Carbon Mater. 2012;27(3):226–32.

55.   Ferrari AC, Robertson J. Raman spectroscopy of amorphous, nanostructured, diamond-like carbon, and nanodiamond. Philos Trans R Soc A Math Phys Eng Sci. 2004;362(1824):2477–512.

56.   Reich S, Ferrari AC, Arenal R, Loiseau A, Bello I, Robertson J. Resonant Raman scattering in cubic and hexagonal boron nitride. Phys Rev B - Condens Matter Mater Phys. 2005;71(20):1–12.

57.   Kawamura K, Jenkins GM. A new glassy carbon fibre. J Mater Sci. 1970;5(3):262–7.

58.   Craievich AF. On the structure of glassy carbon. Mater Res Bull. 1976;11(10):1249–55.

59.   Baker DF, Bragg RH. The electrical conductivity and hall effect of glassy carbon. 1983;58:57–69.

60.   Lewis IC, Pirro TA, Miller DJ. Method for makng a graphite component covered with a layer of glassy carbon. 1995;(19).

61.   Teng H, Wang SC. Preparation of porous carbons from phenol-formaldehyde resins with chemical and physical activation. Carbon N Y. 2000;38(6):817–24.

62.   Kamide K, Miyakawa Y. Limiting Viscosity Number-Molecular Weight Relationships for Phenol-Formaldehyde Resin in Solution. Die Makromol Chemie. 1978;372:359–72.

63.   Poljanšek I, Krajnc M. Characterization of phenol-formaldehyde prepolymer resins by in line FT-IR spectroscopy. Acta Chim Slov. 2005;52(3):238–44.

64.   Pilato L. Phenolic Resins: A Century of Progress: A Century of Progress - Google

Books [Internet]. 2013. Available from:
http://books.google.co.id/books?id=a6Hd6Trsnw8C&pg=PA305&lpg=PA305&dq=ph
enolic+resin;composite+brake;pdf&source=bl&ots=GDYgRgfnVY&sig=iqu3ST9E4YRj
DlaJcCwzlqAjThc&hl=en&sa=X&ei=oD8PUpHmH8KtrAeL_IDwBQ&redir_esc=y#v=on
epage&q=phenolic resin;composite brake;p

65.   Gardziella A, Pilato LA, Knop A. Phenolic Resins: Chemistry, Applications,
       Standardization, Safety and Ecology (Google eBook) [Internet]. 2000. 5–9 p.
       Available from:
       http://books.google.com/books?hl=en&lr=&id=CDOAraoWwTMC&pgis=1

66.   Shudo Y, Izumi A, Hagita K, Nakao T, Shibayama M. Large-scale molecular dynamics
       simulation of crosslinked phenolic resins using pseudo-reaction model. Polymer
       (Guildf) [Internet]. 2016;103:261–76. Available from:
       http://dx.doi.org/10.1016/j.polymer.2016.09.069

67.   Shudo Y, Izumi A, Hagita K, Nakao T, Shibayama M. Structure-mechanical property
       relationships in crosslinked phenolic resin investigated by molecular dynamics
       simulation. Polym (United Kingdom) [Internet]. 2017;116:506–14. Available from:
       http://dx.doi.org/10.1016/j.polymer.2017.02.037

68.   Zhong Y, Jing X, Wang S, Jia QX. Behavior investigation of phenolic hydroxyl groups
       during the pyrolysis of cured phenolic resin via molecular dynamics simulation.
       Polym Degrad Stab [Internet]. 2016;125:97–104. Available from:
       http://dx.doi.org/10.1016/j.polymdegradstab.2015.11.017

69.   Kimuraf S. Graphitization of Carbon Fibre / Glassy Carbon Composites. Carbon N Y.
       1974;12:249–58.

70.   Sharma S, Kamath R, Madou M. Porous glassy carbon formed by rapid pyrolysis of
       phenol-formaldehyde resins and its performance as electrode material for
       electrochemical double layer capacitors. J Anal Appl Pyrolysis [Internet].
       2014;108:12–8. Available from: http://dx.doi.org/10.1016/j.jaap.2014.05.025

71.   Potts SJ, Lau YC, Dunlop T, Claypole T, Phillips C. Effect of photonic flash annealing
       with subsequent compression rolling on the topography, microstructure and
       electrical performance of carbon-based inks. J Mater Sci [Internet].
       2019;54(11):8163–76. Available from: https://doi.org/10.1007/s10853-019-03462-3

72.   Hübschmann H-J. Handbook of GC-MS: Fundamentals and Applications. Third. John
       Wiley & Sons; 2015. 880 p.

73.   Ibrahim EA, Wang M, Radwan MM, Wanas AS, Majumdar CG, Avula B, et al. Analysis
       of Terpenes in Cannabis sativa LUsing GC/MS: Method Development, Validation,
       and Application. Planta Med. 2019;85(5):431–8.

74.   Hermabessiere L, Himber C, Boricaud B, Kazour M, Amara R, Cassone AL, et al.
       Optimization, performance, and application of a pyrolysis-GC/MS method for the
       identification of microplastics. Anal Bioanal Chem. 2018;410(25):6663–76.

75.   Parry V KD. Scanning Electron Microscopy : An introduction. III-Vs Rev.
       2000;13(4):40–4.

76.   Kumar CSSR. Raman spectroscopy for nanomaterials characterization. Vol.
       9783642206, Raman Spectroscopy for Nanomaterials Characterization. 2012. 1–645

p.

77. Yu PY, Cardona M. Fundamentals of Semiconductors [Internet]. 4th Editio. Berlin, Heidelberg: Springer Berlin Heidelberg; 2010. Chapter 7. (Graduate Texts in Physics). Available from: http://link.springer.com/10.1007/978-3-642-00710-1

78. Moulder JF, Stickle WF, Sobol PE, Bomben KD. X-ray photoelectron spectroscopy (XPS). Handbook of X-ray Photoelectron Spectroscopy. 1993. 260 p.

79. Kaciulis S. Spectroscopy of carbon: From diamond to nitride films. Surf Interface Anal. 2012;44(8):1155–61.

80. Islam T, Hasan MM, Shah SS, Karim MR, Al-Mubaddel FS, Zahir MH, et al. High yield activated porous coal carbon nanosheets from Boropukuria coal mine as supercapacitor material: Investigation of the charge storing mechanism at the interfacial region. J Energy Storage [Internet]. 2020;32(July):101908. Available from: https://doi.org/10.1016/j.est.2020.101908

81. Tiwari P, Jaiswal J, Chandra R. Hierarchal growth of MoS2@CNT heterostructure for all solid state symmetric supercapacitor: Insights into the surface science and storage mechanism. Electrochim Acta [Internet]. 2019;324:134767. Available from: https://doi.org/10.1016/j.electacta.2019.134767

82. Simon P, Gogotsi Y, Dunn B. Where do Batteries end and Supercapacitors Begin ? Science (80-). 2014;343(March):1210–1.

83. Smits FM. Measurement of Sheet Resistivities with the Four-Point Probe. Vol. 37, Bell System Technical Journal. 1958. p. 711–8.

84. Challenger KD, Moteff J. Characterization of the Deformation Substructure of Aisi 316 Stainless Steel After High Strain Fatigue At Elevated Temperatures. Met Trans. 1972;3(6):1675–8.

85. WEISS B, STICKLER R. Phase instabilities during high temperature exposure of 316 austenitic stainless steel. Met Trans. 1972;3(4):851–66.

86. Nakamizo M, Kammereck R, Walker PL. Laser raman studies on carbons. Carbon N Y. 1974;12(3):259–67.

87. VIDANO R, FISCHBACH DB. New Lines in the Raman Spectra of Carbons and Graphite. J Am Ceram Soc. 1978;61(1–2):13–7.

88. Vidano RP, Fischbach DB, Willis LJ, Loehr TM. Observation of Raman band shifting with excitation wavelength for carbons and graphites. Solid State Commun. 1981;39(2):341–4.

89. Mezzi A, Kaciulis S. Surface investigation of carbon films: From diamond to graphite. Surf Interface Anal. 2010;42(6–7):1082–4.

90. Briggs D. X-ray photoelectron spectroscopy (XPS). Handb Adhes Second Ed. 2005;621–2.

91. Carroll B, McGuire GE. Auger electron spectroscopy reference manual. Microchem J. 1981;26(3):444.

92. Seddon BJ, Osborne MD, Lagger G, Dryfe RAW, Loyall U, Schäfer H, et al. Micro-

glassy carbon inks for thick-film electrodes. Electrochim Acta. 1997;42(12):1883–94.

93. Jiang Y, Liu J. Definitions of Pseudocapacitive Materials: A Brief Review. Energy Environ Mater. 2019;2(1):30–7.

94. Chen X, Shirai Y, Yanagida M, Miyano K. Effect of light and voltage on electrochemical impedance spectroscopy of perovskite solar cells: An empirical approach based on modified randles Circuit. J Phys Chem C. 2019;123(7):3968–78.

95. Lai CY, Huang WC, Weng JH, Chen LC, Chou CF, Wei PK. Impedimetric aptasensing using a symmetric Randles circuit model. Electrochim Acta [Internet]. 2020;337:135750. Available from: http://dx.doi.org/10.1016/j.electacta.2020.135750

96. Murariu T, Morari C. Time-dependent analysis of the state-of-health for lead-acid batteries: An EIS study. J Energy Storage [Internet]. 2019;21(June 2018):87–93. Available from: https://doi.org/10.1016/j.est.2018.11.011

97. Cao WJ, Greenleaf M, Li YX, Adams D, Hagen M, Doung T, et al. The effect of lithium loadings on anode to the voltage drop during charge and discharge of Li-ion capacitors. J Power Sources. 2015;280:600–5.

98. Pell WG, Conway BE, Adams WA, De Oliveira J. Electrochemical efficiency in multiple discharge/recharge cycling of supercapacitors in hybrid EV applications. J Power Sources. 1999;80(1):134–41.

99. Pell WG, Conway BE, Marincic N. Analysis of non-uniform charge/discharge and rate effects in porous carbon capacitors containing sub-optimal electrolyte concentrations. J Electroanal Chem. 2000;491(1–2):9–21.

100. Popkirov GS, Burmeister M, Schindler RN. Electrode potential redistribution during silver oxidation and reduction in alkaline solution. J Electroanal Chem. 1995;380(1–2):249–54.

101. Phillips C, Al-Ahmadi A, Potts SJ, Claypole T, Deganello D. The effect of graphite and carbon black ratios on conductive ink performance. J Mater Sci. 2017;52(16):9520–30.

102. Hatala M, Gemeiner P, Hvojnik M, Mikula M. The effect of the ink composition on the performance of carbon-based conductive screen printing inks. J Mater Sci Mater Electron [Internet]. 2019;30(2):1034–44. Available from: http://dx.doi.org/10.1007/s10854-018-0372-7

103. Hof F, Kampioti K, Huang K, Jaillet C, Derré A, Poulin P, et al. Conductive inks of graphitic nanoparticles from a sustainable carbon feedstock. Carbon N Y. 2017;111:142–9.

104. Aziz A, Bazbouz MB, Welland ME. Double-Walled Carbon Nanotubes Ink for High-Conductivity Flexible Electrodes. ACS Appl Nano Mater. 2020;3(9):9385–92.

105. Olthuis W, Streekstra W, Bergveld P. Theoretical and experimental determination of cell constants of planar-interdigitated electrolyte conductivity sensors. Sensors Actuators B Chem. 1995;24(1–3):252–6.

106. Sheppard NF, Tucker RC, Wu C. Electrical Conductivity Measurements Using

Microfabricated Interdigitated Electrodes. Anal Chem. 1993;65(9):1199–202.

107.   Dizon A, Orazem ME. On experimental determination of cell constants for interdigitated electrodes. Electrochim Acta [Internet]. 2020;337:135732. Available from: http://dx.doi.org/10.1016/j.electacta.2020.135732

108.   Griffin R, Hooper K, Charbonneau C, Baker J. Comparative Study of Radiative Heating Techniques for Fast Processing of Functional Coatings for Sustainable Energy Applications: Applications of radiative mechanisms in solar energy, battery storage and fuel cells. Johnson Matthey Technol Rev. 2022;66(1):32–43.

109.   Pu NW, Shi GN, Liu YM, Sun X, Chang JK, Sun CL, et al. Graphene grown on stainless steel as a high-performance and ecofriendly anti-corrosion coating for polymer electrolyte membrane fuel cell bipolar plates. J Power Sources [Internet]. 2015;282:248–56. Available from: http://dx.doi.org/10.1016/j.jpowsour.2015.02.055

110.   Liu T -C., Pell WG, Conway BE, Roberson SL. Behavior of Molybdenum Nitrides as Materials for Electrochemical Capacitors: Comparison with Ruthenium Oxide. J Electrochem Soc. 1998;145(6):1882–8.

111.   Sols L, Engineering A. Current and Potential Distribution in Parallel Electrodes. 1995;244(1975):236–44.

112.   Costentin C. Electrochemical Energy Storage: Questioning the Popular $v/ v1/2$Scan Rate Diagnosis in Cyclic Voltammetry. J Phys Chem Lett. 2020;11(22):9846–9.

113.   Mabbott GA. An introduction to cyclic voltammetry. J Chem Educ. 1983;60(9):697–702.

114.   Hinderliter BR, Croll SG, Tallman DE, Su Q, Bierwagen GP. Interpretation of EIS data from accelerated exposure of coated metals based on modeling of coating physical properties. Electrochim Acta. 2006;51(21):4505–15.

115.   Muralidharan VS. Warburg impedance - Basics revisited. Anti-Corrosion Methods Mater. 1997;44(1):26–9.

116.   Buj-Corral I, Domínguez-Fernández A, Gómez-Gejo A. Effect of printing parameters on dimensional error and surface roughness obtained in direct ink writing (DIW) processes. Materials (Basel). 2020;13(9).

117.   Arutyunyan NR, Komlenok MS, Zavedeev E V., Pimenov SM. Raman Spectroscopy of Amorphous Carbon Films Modified by Single-Pulse Irradiation of Nanosecond and Femtosecond Lasers. Phys Status Solidi Basic Res. 2018;255(1):1–6.

118.   Cördoba-Torres P, Mesquita TJ, Nogueira RP. Relationship between the origin of constant-phase element behavior in electrochemical impedance spectroscopy and electrode surface structure. J Phys Chem C. 2015;119(8):4136–47.

119.   Baker J, McGettrick JD, Gethin DT, Watson TM. Impedance Characteristics of Transparent GNP-Pt Ink Catalysts for Flexible Dye Sensitized Solar Cells. J Electrochem Soc. 2015;162(8):H564–9.

120.   Liu J, Li Y, Zhao H. A temperature measurement system based on PT100. Proc - Int Conf Electr Control Eng ICECE 2010. 2010;296–8.

121.   Wang Q, Wang G, Xie X, Zhou L. Design and simulation for temperature

measurement and control system based on PT100. Proc 2019 IEEE 4th Adv Inf Technol Electron Autom Control Conf IAEAC 2019. 2019;(Iaeac):2301–4.